PUC RIO

Dissertação de Mestrado

Development of a system for locating non-ferromagnetic metallic foreign bodies based on GMI magnetometers and eddy currents

Brando Luis Martínez Chavez

Pontifícia Universidade Católica do Rio de Janeiro
Centro Técnico Cientifico
Programa de Pós-Graduação em Metrologia - PUC-Rio

Rio de Janeiro, 13 de outubro de 2025

Pontifícia
Universidade
Católica do
Rio de Janeiro

Dissertação de Mestrado

Development of a system for locating non-ferromagnetic metallic foreign bodies based on GMI magnetometers and eddy currents

Brando Luis Martínez Chavez

Orientação: Professora Elisabeth Costa Monteiro, Dra.
Coorientação: Professor Carlos Roberto Hall Barbosa, Dr.

Dissertação apresentada como requisito parcial para a obtenção
do grau de Mestre pelo Programa de Pós-Graduação em Metrologia da
PUC-Rio.

Rio de Janeiro, 13 de outubro de 2025

Pontifícia
Universidade
Católica do
Rio de Janeiro

Development of a system for locating non-ferromagnetic metallic foreign bodies based on GMI magnetometers and eddy currents

Brando Luis Martínez Chavez

Dissertação apresentada como requisito parcial para a obtenção do grau de Mestre em Metrologia. Aprovada pela Comissão examinadora abaixo:

Professora Elisabeth Costa Monteiro, Dra.
Orientadora
Programa de Pós-Graduação em Metrologia - PUC-Rio

Professor Carlos Roberto Hall Barbosa, Dr.
Co-Orientador
Programa de Pós-Graduação em Metrologia - PUC-Rio

Professor Eduardo Costa da Silva, Dr.
Departamento de Engenharia Elétrica -PUC-Rio

Professor Daniel Ramos Louzada, Dr.
Programa de Pós-Graduação em Metrologia - PUC-Rio

Professor José Franco Machado do Amaral, Dr.
Universidade do Estado do Rio de Janeiro – UERJ

Rio de Janeiro, 13 de outubro de 2025

Pontifícia
Universidade
Católica do
Rio de Janeiro

Brando Luis Martínez Chavez

Graduado em Engenharia Eletrônica, com especialização em Telecomunicações, pela Pontifícia Universidade Católica de Santa Maria (UCSM) em 2021.

Ficha Catalográfica

Martínez Chavez, Brando Luis

Development of a system for locating non-ferromagnetic metallic foreign bodies based on GMI magnetometers and eddy currents / Brando Luis Martínez Chavez ; orientadora: Elisabeth Costa Monteiro; coorientador: Carlos Roberto Hall Barbosa. – 2025.
123 f. : il. color. ; 30 cm

Dissertação (mestrado)–Pontifícia Universidade Católica do Rio de Janeiro, Centro Técnico Científico, Programa de Pós-Graduação em Metrologia, 2025.
Inclui bibliografia

1. Metrologia – Teses. 2. Metrologia. 3. Magnetoimpedância gigante. 4. Correntes parasitas. 5. Corpos estranhos metálicos não-ferromagnéticos. 6. Redes neurais artificiais. I. Monteiro, Elisabeth Costa. II. Barbosa, Carlos Roberto Hall. III. Pontifícia Universidade Católica do Rio de Janeiro. Centro Técnico Científico. Programa de Pós-Graduação em Metrologia. IV. Título.

CDD:389.1

This work is dedicated to my parents Sara and Luís, and to all the good people
who have come into my life.

Acknowledgments

I would especially like to thank Professors Elisabeth Costa Monteiro and Carlos Roberto Hall Barbosa, whose guidance and support were fundamental to my academic development. Together, they formed a solid foundation that propelled me forward on my journey, providing not only technical knowledge but also the inspiration necessary to explore new horizons in the field of metrology. Their dedication to teaching and research made a significant difference in my education, and I am deeply grateful for all the opportunities they offered me.

I am also grateful to Professors JAN Cruguer and Evandro Costa Dos Reis, whose guidance and support were essential in building this project. The collaboration and knowledge shared by both were crucial to the development of this phase, allowing me to move forward with confidence and clarity.

I cannot fail to mention all my colleagues from the Metrology program at PUC-Rio. More than friends, we formed a true family, sharing a learning experience that led us to explore the boundaries of knowledge. Together, we always believed that "everything will be alright," and this mutual trust was essential in overcoming the challenges throughout our academic journey. I am thankful for every moment we shared and for the unconditional support we gave one another.

I am deeply thankful to my parents, Luís Pedro Martinez Huamani and Sara Maribel Chavez Gutierrez, who have always strived to help me become a better person and a successful professional. Their unwavering belief in my potential motivated me to always give my best and to believe that I can achieve any goal I set for myself. I will be forever grateful for all the love, support, and wisdom they have given me throughout my life. You have been and will always be my greatest inspiration.

To my wife and son, who have been my greatest inspiration in completing this thesis. To you, my love, for your unconditional love, endless patience, and for standing by my side through every step of this journey. And to you, my son, for reminding me every day of the true meaning behind this effort. You are my driving force and my reason to never give up.

Finally, I thank God for granting me the necessary blessings and for placing the right people in my path throughout the master's program, enabling me to face every adversity.

This study was financed in part by the Coordenação de Aperfeiçoamento de Pessoal de Nível Superior - Brasil (CAPES) - Finance Code 001.

Abstract

Chavez, Brando Luis Martínez; Monteiro, Elisabeth Costa (Advisor); Barbosa, Carlos Roberto Hall (Co-Advisor). **Development of a system for locating non-ferromagnetic metallic foreign bodies based on GMI magnetometers and eddy currents. Rio de Janeiro, 2025.** Dissertação de Mestrado - Departamento de Metrologia, Pontifícia Universidade Católica do Rio de Janeiro.

The detection of non-ferromagnetic metallic foreign bodies within the human body presents a clinical challenge, especially due to the limitations of conventional imaging techniques such as X-rays and computed tomography, which expose patients to ionizing radiation and do not always provide precise localization. This work presents the development of a portable, low-cost system operating at room temperature, based on Giant Magnetoimpedance (GMI) sensors and planar spiral coils. The approach employs eddy current induction and differential gradiometric measurements to non-invasively detect non-ferromagnetic metallic bodies, enhancing accuracy and sensitivity compared to existing methods. Experimental results, supported by computational simulations, show that the primary magnetic field reaches up to 179 µT at a depth of 6.3 mm, consistent with simulated values. Reliable detection of the secondary field enables high-precision localization of the objects. In addition to solving the direct problem, this work also addresses the inverse problem by proposing a methodology based on artificial neural networks to estimate physical characteristics of non-ferromagnetic metallic bodies, such as depth (height) and diameter, from the signals acquired by sensors. This extends the applicability of the system to real clinical contexts, offering more accurate diagnostics and contributing to more efficient localization and characterization of foreign bodies, even in situations where conventional techniques would present limitations.

KEYWORDS:

Metrology; Giant Magnetoimpedance (GMI); eddy currents; non-ferromagnetic metallic bodies; artificial neural networks.

Resumo

Chavez, Brando Luis Martínez; Monteiro, Elisabeth Costa (Orientador); Barbosa, Carlos Roberto Hall (Co-Orientador). **Desenvolvimento de um sistema para localização de corpos estranhos metálicos não-ferromagnéticos baseado em magnetômetros GMI e correntes parasitas. Rio de Janeiro, 2025**. Dissertação de Mestrado - Departamento de Metrologia, Pontifícia Universidade Católica do Rio de Janeiro.

A detecção de corpos metálicos estranhos não ferromagnéticos no corpo humano representa um desafio clínico, especialmente devido às limitações das técnicas de imagem convencionais, como raios X e tomografias computadorizadas, que expõem os pacientes à radiação ionizante e nem sempre fornecem uma localização precisa. Este trabalho apresenta o desenvolvimento de um sistema portátil, de baixo custo e operando à temperatura ambiente, baseado em sensores de Impedância Magneto-Gigante (GMI) e bobinas espirais planas. A abordagem emprega a indução de correntes parasitas e medições gradiométricas diferenciais para detectar, de forma não invasiva, corpos metálicos não ferromagnéticos, aumentando a precisão e a sensibilidade em comparação com os métodos existentes. Os resultados experimentais, apoiados por simulações computacionais, mostram que o campo magnético primário atinge até 179 μT a uma profundidade de 6,3 mm, em conformidade com os valores simulados. A detecção confiável do campo secundário permite a localização precisa dos objetos. Além de resolver o problema direto, este trabalho também aborda o problema inverso, propondo uma metodologia baseada em redes neurais artificiais para estimar características físicas dos corpos metálicos não ferromagnéticos, como profundidade (altura) e diâmetro, a partir dos sinais adquiridos pelos sensores. Isso amplia a aplicabilidade do sistema a contextos clínicos reais, oferecendo diagnósticos mais precisos e contribuindo para uma localização e caracterização mais eficiente dos corpos estranhos, mesmo em situações nas quais as técnicas convencionais apresentariam limitações.

Palavras-chave

Metrologia; Magnetoimpedância Gigante; correntes parasitas; corpos estranhos metálicos não-ferromagnéticos; redes neurais artificiais

SUMÁRIO

LIST OF FIGURES

LIST OF TABLES

1

Introduction

The presence of metallic foreign bodies in the human body, often resulting from accidents or firearm projectiles, usually require surgical intervention [1,2,3]. However, conventional surgical procedures for their removal have proven challenging, largely due to the inefficiency of imaging techniques used for accurate localisation [1]. The use of ionising radiation, which is commonly employed in such cases, poses health risks to patients and suffers from limited precision, especially when dealing with small metallic foreign bodies [1,4] Given this reality, the search for innovative and safer methods becomes imperative, highlighting the current need for technological advances in the medical field.

Locating foreign objects in the human body through conventional imaging approaches, such as radiography, computed tomography, and fluoroscopy during surgical procedures, is a common practice [1,3,4]. Although these techniques are non-invasive, their use of ionising radiation implies health risks for patients and the surgical team [1,3,5]. As mentioned earlier, such approaches are unable to determine the exact positioning of the foreign body, such as the depth relative to the skin, resulting in surgical procedures that are often prolonged and have high failure rates in removing the undesired object [1,3,4,6]. This limitation highlights the critical need to develop safer, harmless, non-invasive, and effective alternatives for imaging and removing foreign bodies, underscoring the continued importance of technological innovation in the medical field [1-4].

New techniques are based on mapping the magnetic flux density generated by the foreign body. This approach enables a non-invasive and highly accurate assessment of the location of ferromagnetic objects. The Superconducting Quantum Interference Device (SQUID) is currently the most sensitive magnetometer, exhibiting extremely low noise levels, which has led to the development of a technique for locating foreign bodies [1]. The application of this technique was successful in seven clinical cases, resulting in the effective and swift surgical removal of foreign bodies, including ferromagnetic and sewing needles [1,4,6,7].

However, this magnetic measurement system was based on a SQUID system which, in order to perform its physical transduction process, operated at cryogenic temperatures, approximately -269.5° C [1,4,7]. In addition to being an expensive and low-portability device, operating under such conditions required a volume of liquid helium and a Dewar vessel to contain and pressurise this fluid. These logistical characteristics and associated costs limited the accessibility and practical feasibility of this system in broader clinical contexts [1,3,4].

Recently, the team at the Biometrology Laboratory (LabBioMet) of PUC-Rio has focused on research in the area of non-invasive clinical diagnosis, developing low-cost, portable measurement systems operating at room temperature for the detection of metallic foreign bodies in the human body, using magnetometers based on the phenomena of Giant Magnetoimpedance (GMI) and Giant Magnetoresistance (GMR) [2,3,4,8-13].

Metallic foreign bodies, however, are not always ferromagnetic, which represents an additional challenge for localisation. Firearm projectiles, commonly encountered in medical practice [14], are typically made of lead (Pb), consisting of chemical elements that exhibit diamagnetic properties. In this case, locating these objects via magnetic mapping will require the induction of eddy currents using an alternating magnetic field [2,3,10,15,16], which can be detected by a magnetometer with the adequate sensitivity and resolution [3,4,15].

The process to be applied must be based on the theory of classical electromagnetism, which describes the induction of eddy currents in the foreign body. In this context, when the foreign object is subjected to an alternating primary magnetic field, it induces a secondary magnetic field [2,3,15]. This secondary magnetic field is then detected by the measurement system, which consists of a sufficiently sensitive magnetometer. The data collected is then processed computationally to build a map of the magnetic flux density generated by the currents induced in the object. This approach, based on the induction of eddy currents, allows precise information to be obtained about the position and dimension of the foreign object, providing an effective technique for detecting and locating non-ferromagnetic foreign bodies in the human body [1,2,3,15].

A previously developed system [3,10], represented in Figure 1, uses a solenoid excited by an alternating current (AC) as the primary magnetic field generator, with a frequency of 8 kHz and amplitude at the limit of 1 μT (the saturation limit of GMI sensors). The variation in primary magnetic flux density (B_o) generates eddy currents in the foreign body, simplified as (I_{eddy}), a sphere with radius a, located at a distance z from the base of the solenoid in Figure 1, resulting in the production of a secondary alternating magnetic field (B_s) [1,2,3].

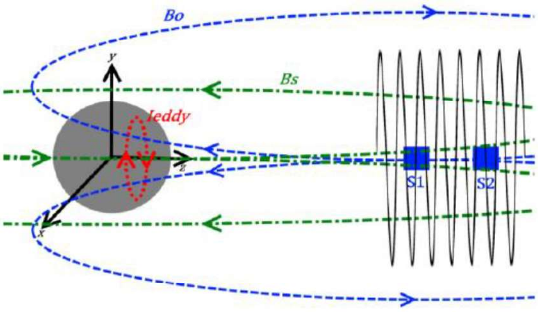

Figure 1 - Simplified diagram of the detection procedure developed in [3]

This secondary magnetic field is measured by the GMI sensors (S_1 and S_2) positioned symmetrically along the solenoid (Figure 1), with both sensors being exposed to the same primary magnetic field, the effect of which can then be neutralised by means of a differential measurement. However, due to the proximity of S_1 to the foreign body, the secondary magnetic field incident on it is considerably more intense than the secondary field reaching S_2, and this disparity in intensity between the secondary fields at S_1 and S_2 in a gradiometric configuration is exploited to enable effective identification and discrimination [1,2,3].

The system in [3,10] demonstrated effectiveness in estimating the radius of the projectile and its depth in relation to the patient's skin. However, due to the fact that the excitation magnetic field B_0 (primary) is restricted to the maximum value of the GMI sensor's linear operating range, which is ±1 μT, the secondary field B_s generated by the induction of eddy currents is also limited. This limitation reduces the instrument's detection capacity, especially in cases where the dimensions and depth of the metallic foreign body are significant [2,3,10]. This consideration highlights the importance of evaluating the system's limitations in relation to the specific characteristics of the foreign body to be detected.

Thus, it becomes imperative to develop measurement system configurations that overcome the limitations to the transducer's capacity due to the interference of the primary magnetic field on the sensing elements.

The project developed in [2] presented alternative configurations involving pairs of planar spiral coils or long vertical solenoids, both with windings in opposite directions. Performance analysis revealed that the use of planar spiral coils yielded superior results in terms of the ability to excite the foreign object with higher magnetic field values while keeping the GMI sensor within its linear measurement range [2]. Furthermore, the evaluation of the secondary magnetic field generated by the eddy currents induced in non-magnetic metallic foreign bodies revealed distinct behaviours for the GMI sensor in horizontal and vertical positions, demonstrating the effectiveness of this new approach for locating such foreign bodies at different depths in the human body [2].

Building on the successful results of the computational study presented in [2], using planar spiral coils for excitation, the next step is to develop an experimental implementation of the system. Additionally, the potential benefits of a gradiometric configuration for the sensing elements utilising a dual-sensor experimental setup to measure the secondary magnetic flux density could be explored. At this stage, it will be essential to address practical challenges and design modifications arising from the use of actual components, while ensuring strict compliance with the exposure limits established by the International Commission on Non-Ionising Radiation Protection (ICNIRP). Such compliance is essential to guarantee adherence to international safety standards.

1.1
Objectives: general and specific

The general objective of the research is to develop a measurement system for localising non-ferromagnetic metallic foreign bodies in the human body at significant depths relative to the skin surface, based on the induction of eddy currents, using GMI magnetometers. The research will also investigate the eventual benefit of arranging two GMI magnetometers in a gradiometric configuration. An appropriately designed excitation module will be implemented to prevent interference with the sensor element by emitting primary excitation magnetic field levels and secondary fields generated by eddy currents that respect the non-ionising radiation exposure limits established by international guidelines.

To achieve this overall purpose, the following specific objectives were defined:

- Identify the key regulatory/normative documents and international guidelines applicable to the reliability of equipment for locating non-ferromagnetic metallic foreign bodies in the human body;
- Perform the theoretical and computational characterisation of the measurement system, with its excitation components (generation of primary magnetic field) and detection using the GMI sensor (from the secondary magnetic field generated by eddy currents induced in non-ferromagnetic metallic foreign bodies), meeting the most critical clinical demands and complying with non-ionising radiation exposure limits established by international guidelines;
- Carry out computational simulations of the secondary magnetic field linear maps measured by the GMI Magnetometer, based on the measurement system to be implemented, also exploring a gradiometric configuration, for different clinical conditions of positioning and geometry of the foreign body;
- Design and develop a prototype of the measurement system and experimental setup for the localisation of non-ferromagnetic metallic bodies, through the induction of Eddy Currents, using the GMI Magnetometer, including its arrangement in a gradiometric configuration;
- Evaluate metrological parameters for performance and safety analysis of the measurement system prototype intended for biomedical applications;
- Conduct experimental magnetic mappings of foreign bodies, such as firearm projectiles represented by lead spheres, in different configurations and positions, characterising the developed measurement system for clinical application, complying with Biometrological Principles;
- Develop and validate a method based on artificial neural networks to solve the inverse problem, enabling the automatic estimation of physical parameters such as depth (distance) and diameter of non-ferromagnetic metallic bodies from signals measured by the developed prototype.

1.2
Dissertation structure

This dissertation is structured in seven chapters, which address the topic of locating non-ferromagnetic metallic foreign bodies in the human body, providing the reader with an approach that identifies and contextualises gaps in the specialised scientific literature, contributing to safety aspects, the scientific community and system operators, through measurement data obtained during this research.

Chapter 1 introduces the context and concepts of the main topics covered by the thesis, describing its general goal and the specific objectives established to achieve that overall purpose.

Chapter 2 provides a detailed review of the relevant magnetic quantities for this thesis, as well as an overview of the International and National Frameworks for ensuring the reliability and comparability of magnetic measurement results, covering the exposure limits to magnetic fields defined by ICNIRP. Additionally, a detailed description of the operating principles of GMI magnetometers is presented, including the metrological characteristics of the commercial and laboratory models currently available.

Chapter 3 presents a detailed theoretical characterisation and computational modelling of the measurement system developed for detecting non-ferromagnetic metallic foreign bodies. Additionally, it introduces the conceptual foundations of inverse modelling, with an emphasis on the application of artificial neural networks as a predictive tool.

Chapter 4 describes the development of the prototype of the proposed measurement system. The excitation and detection components, including the GMI sensor, are presented in detail, along with the signal conditioning and processing circuit used for gradiometric measurement.

Chapter 5 presents the results and discussion related to the proposed measurement system. It begins with the simulated and experimental results of the primary and secondary magnetic fields, followed by a comparison between simulations and measurements under different gain configurations. Additionally, this chapter describes the application of inverse modelling using artificial neural networks, including the data pre-processing, network training, and performance evaluation.

Chapter 6 presents a critical discussion of the results obtained, highlighting the system's capabilities and limitations.

Finally, Chapter 7 presents the conclusions and recommendations for future work.

2

Metrological Reliability – Measurement of Magnetic Quantities and GMI Magnetometers

This chapter provides a detailed review of the magnetic quantities relevant to this dissertation, as well as an overview of the International and National Frameworks for ensuring the reliability and comparability of magnetic measurement results, covering the exposure limits to magnetic fields defined by ICNIRP. Additionally, a thorough description of the operating principles of GMI magnetometers is presented, including the metrological characteristics of currently available commercial and laboratory models.

2.1

International and National Framework for Ensuring the Reliability and Comparability of Magnetic Measurement Results

2.1.1

International Context

2.1.1.1

BIPM – International Bureau of Weights and Measures

The International Bureau of Weights and Measures (BIPM) was established by the Meter Convention in 1875; an agreement signed in Paris by seventeen states [17]. The primary objective of the BIPM is to ensure the global unification of measurements, with goals that include representing the international metrology community, facilitating measurement comparisons between different countries, and coordinating the global measurement system to ensure that results are comparable and universally accepted.

The BIPM operates under the authority of the General Conference on Weights and Measures (CGPM), which meets every four years with delegates from member countries to review reports and proposals from the International Committee for

Weights and Measures (CIPM) [18]. The CIPM, composed of distinguished metrologists, supervises various advisory committees that address specific areas of metrology, such as the Consultative Committee for Electricity and Magnetism (CCEM), which is relevant to this work.

The International System of Units (SI), established in 1960, consists of seven base units: meter [m] (length), kilogram [kg] (mass), second [s] (time), ampere [A] (electric current), kelvin [K] (temperature), mole [mol] (amount of substance), and candela [cd] (luminous intensity). These units form a coherent set that allows the derivation of additional units.

The BIPM also manages the KCDB (BIPM Key Comparison Database), which compiles information on the measurement and calibration capabilities of the national institutes that are signatories of the Metre Convention and the Mutual Recognition Arrangement of the CIPM (CIPM-MRA). This ensures metrological traceability, allowing countries to declare their Calibration and Measurement Capabilities (CMCs) in various areas, including electricity and magnetism. For example, Australia and Italy have declared specific CMCs in magnetic flux density at different frequencies and amplitude ranges.

In Germany, the PTB (Physikalisch-Technische Bundesanstalt) maintains the national standard for magnetic flux density using nuclear magnetic resonance (NMR) magnetometry. Its systems operate from 1 nT to 2 mT (free precession method) and from 2 mT to 100 mT (absorption method), achieving a typical resolution of 5 nT and relative uncertainties on the order of 10^{-4}.

In the United Kingdom, the NPL (National Physical Laboratory) offers calibration services for DC and AC magnetic fields typically spanning 1 nT to 1 mT, as detailed in its Best Practice Guide for the Generation and Measurement of DC Magnetic Fields. These measurements ensure high stability and traceability for low-field magnetic applications.

2.1.1.2
OIML – International Organisation of Legal Metrology

The International Organisation of Legal Metrology (OIML) is an intergovernmental institution founded in 1955 with the aim of promoting the global harmonisation of legal metrology procedures, thereby facilitating international trade [19]. Its headquarters are located in Paris, France. The OIML develops international recommendations that member states can adopt into their national legislation. Its work seeks to ensure compatibility with the standards established by the International Electrotechnical Commission (IEC) and the International Organisation for Standardisation (ISO).

The OIML consists of various Technical Committees, each specialised in a specific field. The most relevant committee in the area of electrical medical equipment is TC 18 – Medical Measuring Instruments, particularly its Subcommittee TC 18/SC 4 – Bioelectrical Instruments. For the purposes of this work, TC 12 – Instruments for Measuring Electrical Quantities is also significant.

2.1.1.3
IEC – International Electrotechnical Commission

The International Electrotechnical Commission (IEC) is a non-governmental organisation dedicated to international standardisation in the field of electrical and electronic technologies, including electromedical equipment [20]. Founded in 1906 and headquartered in Geneva, Switzerland, the IEC has 107 technical committees and 100 subcommittees responsible for investigating and proposing specific standards in various areas. Among the most relevant for the development of medical devices are:

- **TC 62**: Electrical equipment in medical practice.
- **TC 85**: Measuring equipment for electrical and electromagnetic quantities.
- **TC 108**: Methods for the assessment of electric, magnetic and electromagnetic fields related to human exposure.

IEC 60601 Standards

The **IEC 60601** series focuses on safety and essential performance requirements for electromedical equipment. The most relevant standards for this study include:

- **IEC 60601-1:2005/AMD2:2020 | IEC:** General requirements for basic safety and essential performance of medical electrical equipment.
- **IEC 60601-1-2:2014/AMD1:2020**: Addresses electromagnetic disturbances, specifying requirements and tests for electromagnetic compatibility.
- **IEC 60601-1-6:2010/AMD2:2020**: Focuses on usability, ensuring that the equipment's design is accessible and user-friendly.
- **IEC 60601-1-9:2007/AMD2:2020**: Establishes requirements for environmentally sustainable design.
- **IEC 60601-1-12:2014/AMD1:2020**: Specifies requirements for equipment intended for use in emergency medical services environments.

IEC 61786 Standards

The **IEC 61786** series addresses the measurement of low-frequency electric and magnetic fields (1 Hz to 100 kHz) with regard to human exposure. Notable standards include:

- **IEC 61786:1998**: Measurement of low-frequency magnetic and electric fields with regard to exposure of human beings - Special requirements for instruments and guidance for measurements.
- **IEC 61786-2:2014**: Measurement of DC magnetic, AC magnetic and AC electric fields from 1 Hz to 100 kHz with regard to exposure of human beings - Part 2: Basic standard for measurements.
- **IEC 61786-1:2013/AMD1:2024:** Measurement of DC magnetic, AC magnetic and AC electric fields from 1 Hz to 100 kHz with regard to exposure of human beings - Part 1: Requirements for measuring instruments

These standards are essential to ensure that medical devices comply with international safety and performance norms, thereby promoting patient protection and the correct functioning of the equipment.

2.1.1.4
ICNIRP – International Commission on Non-Ionising Radiation

The International Commission on Non-Ionising Radiation Protection (ICNIRP) is an independent, non-governmental, and non-profit scientific organisation, founded in 1992 in Munich, Germany [21]. Its goal is to continue and complement the work of the International Radiation Protection Association (IRPA). ICNIRP is dedicated to scientific research and the publication of guidelines, reviews, and statements on the adverse effects of non-ionising radiation which includes static electric fields, static magnetic fields, and electromagnetic fields on human health and the environment. Most of its publications are freely available to the public.

For the development of the device in question, the most relevant ICNIRP publications are:

- Guidelines for limiting exposure to time-varying electric and magnetic fields (1 Hz – 100 kHz): Last updated in 2010.
- Guidelines for limiting exposure to time-varying electric, magnetic, and electromagnetic fields (up to 300 GHz): First published in 1998, with a revision currently underway.
- Guidelines on exposure limits for static magnetic fields: Last updated in 2009.

These ICNIRP guidelines establish reference levels for human exposure to electric and magnetic fields across different frequency ranges. Their main objective is to ensure that medical and experimental devices operate within safe limits, preventing possible biological effects associated with non-ionizing radiation. In the context of the present work, these standards are particularly relevant to confirm that the magnetic fields generated by the excitation coils, in the microtesla range, remain well below the recommended exposure limits, ensuring the safety of both the patient and operator.

2.1.1.5

ISO – International Organisation for Standardisation

The International Organisation for Standardisation (ISO) is a non-governmental international entity, founded in 1947 and headquartered in Geneva, Switzerland [22]. Its members are primarily composed of the most representative national standardisation bodies from each country. ISO is dedicated to the development of standards across a wide range of fields and has also collaborated with the International Electrotechnical Commission (IEC) in various areas, such as the evaluation of medical device quality.

ISO is structured into 318 technical committees responsible for studying, discussing, and verifying structures and measurements across industries, with the aim of protecting society from both economic and safety perspectives. The most relevant technical committees for the present study are:

- **ISO/TC 194:** Biological and clinical evaluation of medical devices.
- **ISO/TC 210:** Quality management and general aspects related to medical devices.
- **ISO/TC 210/JWG 01:** Joint working group on the application of risk management to medical devices.
- **ISO/TC 210/JWG 02:** Joint working group on software for medical devices.
- **ISO/TC 210/JWG 03:** Joint working group on the usability of medical devices**.**
- **ISO/TC 210/WG 01:** Application of quality systems to medical devices.
- **ISO/TC 210/WG 02:** General aspects arising from the application of quality principles to medical devices.

The most relevant standard for the proposed device is:

- **ISO 14971:2019:** Medical devices: application of risk management to medical devices**.**

2.1.1.6
WHO – World Health Organisation

The World Health Organisation (WHO) is an entity affiliated with the United Nations (UN), focused on promoting global public health [23]. Founded in 1948 and headquartered in Geneva, Switzerland, the WHO performs several essential functions such as monitoring the global health situation, analysing health trends, and establishing norms and standards.

In the context of medical devices, the WHO refers to ISO and IEC standards. Regarding electromagnetic fields and their impact on human health, the WHO adopts the guidelines developed by the International Commission on Non-Ionising Radiation Protection (ICNIRP). In addition, it relates the effects of radiation on the human body to data from the International Agency for Research on Cancer, where the WHO conducts scientific research and publishes guidelines, reviews, and statements concerning the adverse effects of non-ionising radiation (static magnetic fields and electromagnetic fields) on human health and the environment.

2.1.2
National Organisations

2.1.2.1
INMETRO - National Institute of Metrology, Quality and Technology

INMETRO (*Instituto Nacional de Metrologia, Qualidade e Tecnologia*) is a Brazilian federal agency linked to the Ministry of Development, Industry, and Foreign Trade, founded in 1973 [24]. Its main role is to operate in all areas of metrology: scientific, legal, and industrial. INMETRO's mission is "to strengthen national organisations, generating greater productivity through the adoption of mechanisms that improve the quality of products and services" while also providing Brazilian society with confidence in measurements and products, promoting the harmonisation of consumer relations, innovation, and competitiveness in the country.

INMETRO is responsible for accrediting national certification bodies in Brazil. The traceability of electromagnetic field measurements is ensured by the Laboratory of Magnetism and Electric and Magnetic Fields (LAMCE) [25]. This laboratory maintains the national measurement standards for these quantities, which are used in calibration services performed by accredited laboratories of the Brazilian Calibration Network (RBC) and by companies in the electric sector. The measurement standard for the electric field is a primary standard, while the magnetic measurement standard is traceable to the National Measurement Institute (NMI) of Australia.

Currently, LAMCE provides traceability for magnetic flux densities in the range of 1 µT to 700 µT with uncertainties from ±1.8 % to ±4.0 % at frequencies of 50 Hz or 60 Hz. The laboratory's current objective is to be capable of calibrating devices for DC fields in the range of 2 µT to 2 T with uncertainties below 0.1 %, and subsequently for AC fields between 1 nT and 10 nT at frequencies ranging from 10 Hz to 10 kHz.

2.1.2.2
ANVISA – National Health Surveillance Agency

ANVISA (Brazilian Health Regulatory Agency) is the regulatory body responsible for public health in Brazil [26]. It is a special-regime autonomous agency, which grants it administrative independence and financial autonomy from the government, despite being a public organisation linked to the Ministry of Health. In 1999, ANVISA published Resolution N. 444, which made it mandatory to adopt Brazilian technical standards adapted from the IEC 60601 series, such as NBR IEC 60601-1: Medical Electrical Equipment – Part 1: General Requirements for Safety, in addition to specific standards with particular requirements from the IEC 60601-2 series. This resolution was succeeded by Resolution RDC 32 of May 2007, which was amended in June of the same year and later replaced by Resolution RDC 27 of June 21, 2011. This was, in turn, repealed and replaced by the current Resolution RDC 549 of August 30, 2021, which establishes the procedures for mandatory certification of equipment within the scope of the Health Surveillance System. According to Article 2 of RDC 549/2021, equipment must comply with Resolution RDC ANVISA 546/2021, which sets out the essential safety and performance requirements for health products through conformity certification under the Brazilian Conformity Assessment System (SBAC).

Paragraph 1 of Article 2 of RDC 549/2021 refers to ANVISA's Normative Instruction 49, dated November 22, 2019, to evaluate the requirements for conformity assessment, specifying the standards to be used in the conformity assessment of medical equipment.

Paragraph 2 of Article 2 of RDC 549/2021 states that equipment under health surveillance includes any equipment, as well as their parts and accessories, intended for medical, dental, laboratory, or physiotherapeutic purposes, used directly or indirectly for the diagnosis, treatment, rehabilitation, and monitoring of human beings, as well as equipment for aesthetic and beautification purposes.

2.1.2.3
ABNT – Brazilian National Standards Organisation

ABNT (*Associação Brasileira de Normas Técnicas*) is a national private non-profit organisation founded in 1940 [27]. Its role is supported by the federal government through various legal instruments. ABNT is one of the founding members of the International Organisation for Standardisation (ISO) and is responsible for publishing Brazilian Standards (ABNT NBR), developed by its Brazilian Committees (ABNT/CB), Sectorial Standardisation Bodies (ABNT/ONS), and Special Study Commissions (ABNT/CEE), many of which are translated and adapted versions of ISO and IEC standards. ABNT's work is organised through technical committees. ABNT/CB-026 is the Brazilian Committee for Dental-Medical-Hospital Equipment, which addresses products related to health, except those involving ionising radiation. This committee was responsible for the ABNT NBR ISO 14971:2009 standard, which deals with the application of risk management to healthcare products (Medical devices Application of risk management to medical devices). ABNT/CB-03 is the Brazilian Committee for Electricity, which covers all types of electrical and electronic fields and related areas. ABNT plays a crucial role in technical standardisation in Brazil, promoting the harmonisation of the interests of manufacturers, consumers, government, and the technical/scientific community. The development of Brazilian standards involves the participation of all stakeholders, ensuring that the standards are developed by consensus and in accordance with international best practices.

2.2
Magnetic Quantities

According to the International Vocabulary of Metrology (VIM), a quantity is defined as a "property of a phenomenon, body, or substance that can be expressed quantitatively by a number and a reference." Quantities are classified into two main categories: base quantities and derived quantities. The ISO/IEC 80000 standard establishes the nomenclature and symbols for these quantities, implementing the International System of Quantities (ISQ), which is based on seven fundamental quantities [17,28]. The International System of Units (SI) correlates the corresponding units for these quantities within the ISQ system, ensuring that all physical quantities and their units discussed in this research are aligned with these standards.

The magnetic quantities, that are the focus of this dissertation, include magnetic field strength (H) and magnetic flux density (B), both of which are considered derived quantities. As defined by the International Electrotechnical Vocabulary (IEV), magnetic field strength (H), often simply referred to as the magnetic field, is described as "a vector quantity obtained at a specific point by subtracting the magnetisation (M) from the magnetic flux density, divided by the magnetic permeability of vacuum" ($\mu_0 = 4\pi \times 10^{-7}$ H/m), where μ_r is the relative permeability (in vacuum or in a non-ferromagnetic material, it is approximately equal to 1), and M is the magnetisation vector, which exists only within a ferromagnetic material.

$$H = \frac{B}{\mu_0 \mu_r} - M \tag{1}$$

In a vacuum, this leads to equation (2), which can also be considered a good approximation for air; thus

$$H = \frac{B}{\mu_0} \tag{2}$$

Therefore, in this case, the magnetic flux density (B), also referred to as the magnetic induction vector, is the vector quantity defined as the product of the magnetic field strength and the approximate magnetic permeability of air:

$$B = \mu_0 H = 4\pi \times 10^{-7}\, H \tag{3}$$

To avoid ambiguity, the following terminology will be used: B will be referred to as magnetic flux density, whose SI unit is tesla (T), while H will be referred to as magnetic field strength, whose SI unit is ampere per meter (A/m) [17]. Table 1 shows the two fundamental magnetic quantities, according to the definitions established by the International Electrotechnical Vocabulary (IEV) and the International System of Units (SI).

Table 1 - Representation of magnetic quantities according to the ISQ and SI systems

Quantity (IEV)		**Unit (SI)**		**Base expression (SI)**
Name	**Symbol**	**Name**	**Symbol**	
Magnetic field strength	H	Ampere per metro	A/m	$A\, m^{-1}$
Magnetic flux density	B	tesla	T	$kg\, s^{-2}\, A^{-1}$

In various magnetometer data sheets and in the literature related to the GMI effect, it is common to find these quantities expressed in units of the CGS system (centimetre-gram-second), as illustrated in Table 2.

Table 2 - Representation of magnetic quantities in the ISQ and CGS systems and relationship between the units of magnetic quantities in the SI and CGS systems.

Quantity (IEV)		**Unit (CGS)**		**conversion SI/CGS**
Name	**Symbol**	**Name**	**Symbol**	
Magnetic field strength	H	oersted	Oe	$1\ \mathrm{Oe} = \frac{10^3}{4\pi}\ \mathrm{A/m}$
Magnetic flux density	B	gauss	G	$1\ \mathrm{G} = 10^{-4}\ \mathrm{T}$

The conversion between the units in the SI and CGS systems is shown in Table 2. It is important to note that in the CGS system of units, the magnetic permeability of the vacuum is considered to be a unit value. Therefore, when taking atmospheric conditions into account, the quantities related to magnetic field strength and magnetic flux density have equivalent numerical values.

$$B[\mathrm{G}] = H[\mathrm{Oe}] \tag{4}$$

2.3

GMI Magnetometers

Magnetometers are non-invasive and robust sensors, making them extremely useful for measuring electromagnetic quantities. They are essential in various scientific and technological applications, especially in the monitoring and control of magnetic fields. The use of harmless and non-invasive magnetic readings can facilitate biological measurements by replacing electrodes, provided that the magnetometers used offer adequate resolution and sensitivity [4].

There are two main types of magnetometers: scalar magnetometers, which provide only the magnetic field intensities without any directional information, and vector magnetometers, which can determine the intensity of each axis component. Scalar magnetometers are particularly advantageous in certain applications because they are insensitive to rotational vibrations, whereas vector magnetometers can be more susceptible to low-frequency noise [29].

Among the most promising technologies in the field are SQUID (Superconducting Quantum Interference Device) magnetometers and GMI (Giant Magnetoimpedance) magnetometers. SQUIDs are remarkably sensitive and widely used in measurements that require extreme precision. On the other hand, GMI magnetometers offer significant advantages in environments where miniaturisation, robustness, and operation at room temperature are essential, unlike SQUIDs, which require cryogenic conditions.

2.3.1
Operating Principles

A magnetometer is a device that functions as a transducer, converting magnetic quantities such as magnetic field intensity or magnetic flux density into electrical quantities, typically electric potential difference (volt) or electric resistance (ohm). Furthermore, magnetometers play a crucial role in control and monitoring systems, as well as in high-resolution motion transducers [2,30].

The phenomenon of Giant Magnetoimpedance (GMI) was discovered in the early 1990s, when it was observed that soft ferromagnetic conductive materials, such as CoFeSiB, exhibited significant variations in electrical impedance (ranging from 40 % to 100 % per Oe) when exposed to external magnetic fields [2,30,31].

The basic operation of GMI magnetometers involves exciting the sensor sample with an alternating current, which generates an electromagnetic field capable of magnetising the sample. This magnetisation causes a rearrangement of magnetic domains, resulting in changes in the material's permeability. The dependence of magnetic permeability on the external magnetic field and the applied current alters the penetration depth of the electric current into the sample and, consequently, its impedance [2,11,12,31,32].

GMI elements can be fabricated in sizes as small as 1 µm, offering advantages in spatial resolution and in applications requiring miniaturisation. The impedance variation in GMI materials is generally symmetric around zero magnetic flux density; however, techniques can be applied to make it asymmetric (AGMI) [33,34,35]. This can be achieved by applying a direct current through the material or by exposing it to alternating magnetic fields. The resulting asymmetry introduces significant benefits, such as the ability to distinguish the direction of the magnetic field and enhanced sensitivity near zero magnetic flux density [2,34,36,37].

The basic excitation and measurement scheme for GMI magnetometers is illustrated in Figure 2. The phenomenon is induced by the application of an alternating current (I) along a ribbon, which is subjected to an external magnetic field H_{ext} parallel to it. The resulting voltage V is measured across the terminals of the ribbon .The impedance variation is explained by classical electromagnetism, where the magnetisation of the sensing element increases as it is submitted to an external magnetic field [2,32,36,38].

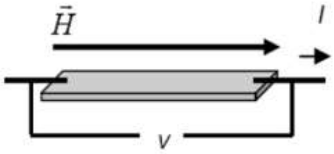

Figure 2 - Typical Measurement Structure with GMI Sensor

The application of an external magnetic field results in an increase in the material's magnetic permeability, which alters the current penetration depth in the sensor. This depth is inversely proportional to both the frequency of the excitation current (*I*) and the magnetic permeability of the GMI element. This phenomenon alters the current path within the sensing element, leading to variations in its electrical impedance [32,39]. The magnitude of impedance variation in GMI magnetometers depends on factors such as the amplitude and frequency of the excitation current, the operating temperature of the element, the polarisation field, and the geometry of the sensing element [2,32].

$$\delta\left(\mu(H)\right) = \left(\frac{2\rho}{\omega * \mu(H)}\right)^{\left(\frac{1}{2}\right)} \tag{5}$$

The following parameters are considered in the analysis:

- $\boldsymbol{H}$: External (Ambient) Magnetic Field
- $\boldsymbol{\mu}$: Magnetic Permeability of the sensor
- $\boldsymbol{\delta}$: Penetration Depth of the Electric Current
- $\boldsymbol{\rho}$: Electrical Resistivity of the material
- $\boldsymbol{\omega}$: Angular Frequency of the Current

The impedance of GMI sensors can be electrically modelled as an inductive load, represented by a series configuration of a resistor and an inductor. Using the phasor description of alternating voltage (AC) and current, and assuming that the phase of the current ($\emptyset_1$) is zero, the impedance of the sample can be calculated [6]. The relationship between voltage and current is given by:

$$Z_{GMI} = \frac{|V| e^{j\emptyset_V}}{|I| e^{j\emptyset_V}} = \frac{|V|}{|I|} e^{j\emptyset} = |Z| e^{j\emptyset} \tag{6}$$

Where $|V|e^{j\emptyset_V}$ and $|I|e^{j\emptyset_V}$ represent, respectively, the potential difference across the ends of the sample and the excitation current, both expressed in phasor form.

Thus, the definition of complex impedance (Z) involves two distinct components: a real component and an imaginary component. For the analysis, the following parameters are considered.

$$Z_{GMI} = R + jX \tag{7}$$

where

$$Z_{GMI} = |Z|cos\emptyset + j|Z|sin\emptyset \tag{8}$$

For the analysis, the following parameters are considered:

- Z_{GMI}: Complex electrical impedance of the sensing element.
- V: Electrical voltage applied to the sensing element
- I: Electric current applied to the element sensor.
- $\emptyset$: Phase angle between voltage and current
- R: Electrical resistance of the sensing element.
- X: Inductive reactance of the sensing element.

Numerous studies have been conducted to explore the potential of the GMI effect. Recently, research has indicated that measuring the phase variation of impedance can result in greater sensitivity compared to traditional measurements of impedance magnitude.

2.3.2
GMI Transducer Aichi

The giant magnetoimpedance (GMI) based magnetometers manufactured by Aichi Micro Technology, model MI-CB-1DJ-M-B, operate based on variations in the magnitude of the electrical impedance of the sensing element (Figure 3). These devices are capable of measuring magnetic flux densities in the range of 15 pT and were selected for this work due to their high sensitivity, low cost, and small sensor element dimensions (13.5 mm in length and 1.2 mm in width) [2,3,31,40]. These characteristics make them particularly suitable for building portable systems dedicated to locating diamagnetic metallic bodies in biomedical applications, as illustrated in Figure 1.

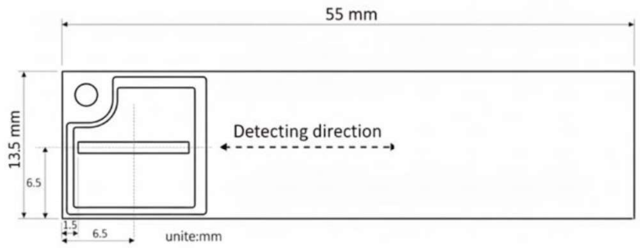

Figure 3 - Simplified diagram showing the dimensions of the Aichi MI-CB-1DJ-M-B prototype GMI sensor **[40]**.

The MI-CB-1DJ-M-B model is available in two versions: single-type and multi-type. The single-type version incorporates an internal oscillator to excite the sensing element, while the multi-type version requires an external oscillator, enabling synchronisation of two or more sensors. The latter was adopted in this work to enable the construction of a first-order gradiometric configuration, which enhances immunity to common-mode noise [41]. The oscillators used must operate with square wave signals, have a 50 % duty cycle, and a voltage range between 0 and 5 V, at a frequency of 1 MHz [40].

Additionally, the sensors are available in two detection orientations: Type A (Figure 4a, perpendicular to the length of the circuit board) and Type B (Figure 4b, parallel to the length of the board). For this project, the Type B version (Figure 4b) was chosen, as it is more suitable for detection along the z-axis.

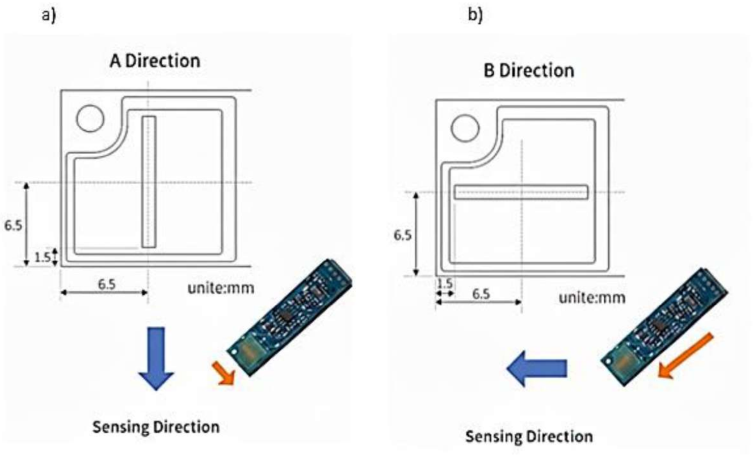

Figure 4 - *Sensor element position and sensing directions of the MI-CB-1DJ model. a) Type A, b) Type B.*[40]

The MI-CB-1DJ-M-B GMI sensor features a symmetric linear operating range of ±1 μT, a typical sensitivity of 5 V/μT, and a bandwidth ranging from 0.1 Hz to 10 kHz. Its estimated analog resolution ranges from 0.3 nT to 1 nT, primarily limited by 1/*f* noise (flicker noise), with a spectral density of 10 pT/√Hz at 1 Hz. It also includes a high-rejection internal analog filter for static and uniform fields, with a cutoff frequency of 0.1 Hz [2,40]. This filtering annihilates the influence of the geomagnetic field, allowing the sensor to respond only to alternating magnetic fields. This feature simplifies the excitation system by eliminating the need for constant bias fields, as required by GMR or Hall effect sensors [2,40].

In previous studies conducted at the Biometrology Laboratory of PUC-Rio, the sensor was operated at a frequency of 8 kHz using a fourth-order analog Butterworth bandpass filter based on the Sallen-Key topology. The results indicated an optimised resolution of up to 25 pT [3], representing the smallest measurable flux density with this sensor.

Although the present study employs a single-axis configuration, Aichi Steel also offers triaxial GMI sensors (e.g., AMI306M model) capable of measuring the magnetic field components along the x, y, and z directions simultaneously. The use of such triaxial configurations, operating under a common excitation frequency, could further enhance spatial resolution and provide a more complete characterisation of the magnetic field in future implementations.

3

Modelling and Simulation of a Measurement System for Locating Non-Ferromagnetic Foreign Objects

This chapter presents the theoretical foundations, computational modelling, and simulation strategies adopted for the development of the proposed measurement system. First, the theoretical characterisation of the system is established within the framework of electromagnetic theory, highlighting the role of the magnetic vector potential and the formulation of eddy current effects. Next, analytical models are introduced to describe the interaction between primary and secondary magnetic fields, including gradiometer configurations designed to enhance measurement sensitivity. Building on these foundations, the chapter details the computational implementation of the primary magnetic field using the Biot–Savart Law, followed by the simulation of magnetic field maps for different positions and geometries of foreign objects. Finally, the concepts of inverse modelling with artificial neural networks are introduced, establishing the basis for the application of machine learning methods in the interpretation of experimental data.

3.1

Theoretical Characterisation of the Measurement System

Within the framework of electromagnetic theory, the magnetic vector potential $\boldsymbol{A}$ is employed, whose main characteristic is that its curl is equivalent to the magnetic flux density $\boldsymbol{B}$. The relationship between these quantities leads to Equation (16), which also involves the electric potential, as expressed in Equation (9). In this work, a theoretical formulation based on $\boldsymbol{A}$ is adopted, as discussed in [42,43] , for the purpose of projectile localisation using magnetometers.

$$E = -\nabla \emptyset_E - \frac{\partial \boldsymbol{A}}{\partial t} \tag{9}$$

In systems where electric fields are generated solely by the presence of a time-varying primary magnetic field, we have $\nabla \emptyset_E = 0$. The electric field $\boldsymbol{E}$ can be related to the resistivity ρ and the current density $\boldsymbol{J}$.

$$\rho \cdot \boldsymbol{J} = -\frac{\partial \boldsymbol{A}}{\partial t} \tag{10}$$

In a conductor with magnetic permeability $\boldsymbol{\mu}$, the induced electric currents produce a magnetic field whose magnetic flux density can be expressed as:

$$\nabla \times \boldsymbol{B} = \mu \boldsymbol{J} \tag{11}$$

In terms of the magnetic vector potential $\boldsymbol{A}$, the following can be written:

$$\nabla^2 \boldsymbol{A} = -\mu \boldsymbol{J} \tag{12}$$

From eqs. (10) and (11)

$$\frac{\mu}{\rho} . \frac{\partial \boldsymbol{J}}{\partial t} = -[\nabla \times (\nabla \times \boldsymbol{J})] = \nabla^2 \boldsymbol{J} - \nabla(\nabla \cdot \boldsymbol{J}) = \nabla^2 \boldsymbol{J} \tag{13}$$

From eqs. (10) and (12)

$$\frac{\mu}{\rho} \frac{\partial \boldsymbol{A}}{\partial t} = \nabla^2 \boldsymbol{A} \tag{14}$$

Equivalently, eq. (16) can be obtained from eqs. (10) and (11), as well as from the knowledge of Gauss's law for magnetism that $\nabla \cdot B = 0$.

$$\frac{\mu}{\rho} . \frac{\partial \boldsymbol{B}}{\partial t} = \nabla(\nabla \cdot \boldsymbol{B}) - \nabla^2 \boldsymbol{B} = [\nabla \times (\nabla \times \boldsymbol{B})] \nabla^2 \boldsymbol{B} \tag{15}$$

Equations (14) and (15) admit solutions in both steady-state and transient regimes. In the steady-state case, it is common to represent the current density as the real part of a Fourier $\check{A}_n e^{jn\omega t}$, series expansion, with terms in the form of the real part of a Fourier series, where n is an integer and ω is the angular frequency. The inverted circumflex indicates a phasor associated with the corresponding term [2,36].

3.1.1
Eddy Current Calculations for Magnetometers

Eddy currents, also known as Foucault currents, are circulating currents induced in conductors when they are exposed to time-varying magnetic fields. This induction is a direct consequence of the presence of a non-conservative and spatially varying electric field, as described by Eq. (9), in accordance with Maxwell–Faraday's equation [44]. Bold upright typography is used to denote vector quantities.

$$\nabla \times \boldsymbol{E} = -\frac{\partial \boldsymbol{B}}{\partial t} \tag{16}$$

Eddy currents are frequently used as a non-destructive testing technique to detect cracks and defects in metals, playing a crucial role in quality control across various industries.

One undesirable aspect of this effect is that the flow of currents through materials generates heat due to the Joule effect, which can be exploited in applications such as induction heating[3]. However, this heating also leads to power losses in devices like transformers and electric motors, requiring careful attention to improve the efficiency of these systems.

Furthermore, the principle of eddy currents is applied in metal detectors, being fundamental to the operation of the proposed device for locating non-magnetic metallic foreign bodies[2,3,15,45]. To achieve this goal, it is essential to carefully consider the parameters involved, aligning the generation of the primary magnetic field with the characteristics of the magnetometer and the biometrological principles [4].

To develop the calculations related to eddy currents detected by magnetometers, it is assumed that the projectile can be modelled as a conducting sphere of radius a. Objects with other geometries will produce a magnetic field with similar characteristics, but scaled by a constant factor that depends on their shape. Assuming the application of a uniform alternating magnetic field in a region containing the object, this field referred to as the primary field induces eddy currents in the sphere [3,15]. In response, these currents generate a secondary magnetic field, whose intensity and spatial distribution depend on the distance between the sphere and the observation point, as well as on the magnetic permeability μ, the electrical conductivity σ, the waveform, and the frequency f_0 of the primary field.

Considering that the radius of the sphere is much smaller than the other dimensions involved, and that its magnetic and electrical properties are homogeneous, the symmetry of the problem allows the use of spherical coordinates $(r, \theta, \emptyset)$, which can later be converted into Cartesian coordinates (x, y, z).The applied field is assumed to be parallel to the z-direction, or orthogonal to the $r\varphi$-plane, and can be described as:

$$B_{app}(f_0, t) = B_0 \cdot e^{2\pi f_0 j t} \hat{z} \tag{17}$$

Where f_0 is the excitation frequency and B_0 is the magnitude of the applied magnetic field. The analytical formulation for the magnetic vector potential induced by eddy currents in a sphere was initially developed by [42] and later employed by [43] in the context of designing magnetic detectors. According to this approach, the secondary magnetic vector potential has only a component in the $\emptyset$-direction, which simplifies the analysis and allows closed-form expressions for the resulting field.

$$A_{s\emptyset}(r, \theta, \emptyset) = \frac{1}{2} B_0 a^3 \left[\frac{(2\mu_r+1)-(2\mu_r-v^2+1)\cdot\frac{\tanh(v)}{v}}{(\mu_r-1)-(\mu_r-v^2+1)\cdot\frac{\tanh(v)}{v}} \right] \frac{sin\theta}{r^2} \tag{18}$$

The factor v is

$$v = (1 + j)\frac{a}{\delta'} \tag{19}$$

Where δ is the skin depth of the eddy current, given by

$$\delta = \sqrt{\frac{1}{f_0} \frac{1}{\pi \mu_r \mu_0 \sigma}} \tag{20}$$

Where $f_0 = \frac{\omega}{2\pi}$ is the frequency of the primary magnetic field, σ is the electrical conductivity, and μ_r is the relative magnetic permeability. In equation (18), the term $\frac{sin\theta}{r^2}$ corresponds to the same expression found in the field of an ideal dipole, while the bracketed factor represents a constant influenced by the material properties and the frequency of the applied field. This indicates that the presence of finite dimensions and frequency variation modifies the secondary magnetic field as a multiplicative factor relative to the theoretical response of an infinitesimal sphere subjected to a static field [2,8].

The behaviour of the secondary magnetic field (B_s), originating from eddy currents in a spherically symmetric body, has been described in various studies [3,10,15,45]. These works demonstrate that (B_s) depends not only on the geometric dimensions of the object subjected to induction, such as its radius (a) and its position in space, but also on the electromagnetic properties of the material, often lead, such as magnetic permeability (μ) and electrical conductivity (σ). In addition, the magnitude and frequency of the incident primary field ($|B_0|$ and f_0, respectively) directly influence the intensity of the eddy currents, and consequently, the resulting secondary field. Thus, the relationship between these variables can be expressed through a specific mathematical model:

$$B_s = f(a, \mu, \sigma, B_0, f_0) \tag{21}$$

This formulation highlights the interdependence between the geometric and electromagnetic characteristics of the body and the conditions of the applied magnetic field.

The secondary magnetic flux density generated by eddy currents is described by the laws of classical electrodynamics, using the concept of the divergence of the magnetic vector potential. This density is expressed in spherical coordinates, which is justified by the symmetry of the problem, as initially expressed in equation (22); the magnetic field B_s is obtained from the curl of the vector potential $\boldsymbol{A}$. The expanded form of this operation in spherical coordinates is presented in equation (23). Modelling in spherical coordinates enables a more precise analysis of magnetic interactions, facilitating the understanding of the magnetic field distributions resulting from the induced currents [2,5,8].

$$B_s(r, \theta, \emptyset) = \nabla \times A(r, \theta, \emptyset) \tag{22}$$

$$B_s(r, \theta, \emptyset) = \frac{1}{r \cdot \sin(\theta)} \cdot \frac{1}{\partial \theta} \left(\frac{\partial A_\emptyset}{\partial \theta} \cdot \sin(\theta) + \frac{\partial A_\emptyset}{\partial \theta} \cdot \right) \hat{r}$$

$$+ \frac{1}{r} \left(\frac{1}{\sin(\theta)} \cdot \frac{\partial A_r}{\partial \emptyset} - \frac{\partial A_\emptyset}{\partial r} \cdot r \right) \widehat{\theta}$$

$$+\frac{1}{r}\left(\frac{\partial A_{\theta}}{\partial r}\cdot r-\frac{\partial A_{r}}{\partial \theta}\right)\hat{\emptyset} \qquad (23)$$

As in this case, for a primary excitation magnetic field parallel to the z-axis, the magnetic vector potential has only a non-zero A_{ϕ}component, and Equation (23) simplifies to Equation (24)

$$B_{s}(r,\theta,\emptyset)=\frac{1}{r\cdot\sin(\theta)}\cdot\frac{1}{\partial\theta}\left(\frac{\partial A_{\emptyset}}{\partial\theta}\cdot\sin(\theta)\right)\hat{r}+\frac{1}{r}\left(\frac{1}{\sin(\theta)}\cdot\frac{\partial A_{r}}{\partial\emptyset}\right)\hat{\theta}+0\hat{\emptyset} \qquad (24)$$

$$B_{s}(r,\theta,\emptyset)=(B_{r},B_{\theta},0) \qquad (25)$$

Upon substituting equation (18) into equation (24), the expressions for the components of the magnetic flux density in the spherical coordinate system are obtained.

$$B_{sr}(r,\theta,\emptyset)=\frac{1}{2}B_{0}a^{3}\left[\frac{(2\mu_{r}+1)-(2\mu_{r}-v^{2}+1)\cdot\frac{\tanh(v)}{v}}{(\mu_{r}-1)-(\mu_{r}-v^{2}+1)\cdot\frac{\tanh(v)}{v}}\right]\frac{sin\theta}{r^{3}} \qquad (26)$$

$$B_{s\theta}(r,\theta,\emptyset)=\frac{1}{2}B_{0}a^{3}\left[\frac{(2\mu_{r}+1)-(2\mu_{r}-v^{2}+1)\cdot\frac{\tanh(v)}{v}}{(\mu_{r}-1)-(\mu_{r}-v^{2}+1)\cdot\frac{\tanh(v)}{v}}\right]\frac{sin\theta}{r^{3}} \qquad (27)$$

$$B_{s\emptyset}(r,\theta,\emptyset)=0 \qquad (28)$$

As most magnetometers detect the component of the magnetic field that is parallel to the excitation, the component of the magnetic flux density along the z-axis in Cartesian coordinates is calculated by:

$$B_{sz}(r,\theta,\emptyset)=B_{sr}(r,\theta,\emptyset)cos\theta-B_{s\emptyset}(r,\theta,\emptyset)\,sin\theta \qquad (29)$$

Or

$$B_{sz}(r,\theta,\emptyset)=\frac{B_{0}}{2}a^{3}\left[\frac{(2\mu_{r}+1)-(2\mu_{r}-v^{2}+1)\cdot\frac{\tanh(v)}{v}}{(\mu_{r}-1)-(\mu_{r}-v^{2}+1)\cdot\frac{\tanh(v)}{v}}\right]\left(\frac{sin\theta}{r^{3}}\right)(3cos^{3}\theta-1) \qquad (30)$$

A measurement plane is now considered to be positioned parallel to the xy plane, located at a distance *h* from the sphere, which also represents its depth. Based on this configuration, the identities presented in equations (31) and (32) can be used to convert the results to the Cartesian coordinate system.

$$r = \sqrt{x^2 + y^2 + h^2} \tag{31}$$

$$cos\theta = \frac{h}{r} = \frac{h}{\sqrt{x^2+y^2+h^2}} \tag{32}$$

By substituting equations (31) and (32) into equation (30), we obtain

$$B_{sz}(x,y,h) = \frac{B_0}{2} a^3 \left[\frac{(2\mu_r+1)-(2\mu_r-v^2+1)\frac{\tanh(v)}{v}}{(\mu_r-1)-(\mu_r-v^2+1)\frac{\tanh(v)}{v}}\right]\left(\frac{2h^2-x^2-y^2}{(x^2+y^2+h^2)^{\frac{5}{2}}}\right) \tag{33}$$

The generated magnetic flux density exhibits cylindrical symmetry, reaching its maximum value at the central point of the measurement plane, that is, at $x = y = 0$. This peak value, denoted as B_{smax}, allows for more precise definition of the specifications for the magnetometer to be used.

$$B_{smax}(h,a,f_0) = B_0 a^3 \left[\frac{(2\mu_r+1)-(2\mu_r-v^2+1)\frac{tanh(v)}{v}}{(\mu_r-1)-(\mu_r-v^2+1)\frac{tanh(v)}{v}}\right]\left(\frac{1}{h^3}\right) \tag{34}$$

Equation (33) then becomes equation (35), which separates the elements that vary with the characteristics of the sphere and the excitation from the depth effect.

$$B_{smax}(h,a,\mathrm{f}_0) = \frac{B_0}{h^3} V(a,\mathrm{f}_0) \tag{35}$$

The complex term $V(a,f_0)$ is formed by a combination of geometric, magnetic, and electrical parameters that are intrinsic to the object in question, in addition to considering the frequency of the primary magnetic flux density.

$$V(a,f_0) = a^3 \cdot \frac{(2\mu_r+1) -(2\mu_r-v^2(a,f_0)+1)\cdot\frac{\tanh\,(v(a,f_0))}{v(af_0)}}{(\mu_r-1)-(\mu_r-v^2(a,f_0)+1)\cdot\frac{\tanh\,(v(af_0))}{v(a,f_0)}} \tag{36}$$

The parameter μ_r represents the relative magnetic permeability of the material of the object in question (typically composed of lead) in relation to the magnetic permeability of the medium where the measurement is performed, which is considered to be air. Both permeabilities have similar values. Thus, μ_r is a dimensionless quantity, and its value approaches 1, approximately $\mu_r = 1 - (1{,}7 \times 10^{-5})$.

Therefore, it can be assumed that $B_0 = \left|B_{px}\right|$ and that the secondary magnetic field B_s can be determined by the vector combination of the spherical components presented in equations (26) and (27).

$$B_{s_x}\,(r,\theta,\emptyset) = B_\theta(r,\theta,\emptyset)\cdot\cos(\theta) - B_\theta(r,\theta,\emptyset)\cdot\sin\,(\theta) \tag{37}$$

$$B_{s_z}\,(r,\theta,\emptyset) = B_r(r,\theta,\emptyset)\cdot\sin(\theta)\cdot\sin(\emptyset) + B_\theta(r,\theta,\emptyset)\cdot\cos(\theta)\cdot\sin\,(\emptyset) \tag{38}$$

Finally, the following expressions are obtained for the two relevant components of the secondary magnetic flux density:

$$B_{s_x}\,(x,y,s) = \frac{B_0}{2}\cdot V(a,f)\cdot(x^2+y^2+z^2)^{-\frac{5}{2}}[2x^2-(y^2+z^2)] \tag{39}$$

$$B_{s_z}\,(x,y,s) = \frac{3B_0}{2}\cdot V(a,f)\cdot(x^2+y^2+z^2)^{-\frac{5}{2}}\left[(y^2+z^2)^{-\frac{1}{2}}\cdot(z^2\cdot x)\right] \tag{40}$$

3.1.2
Gradiometer effects

To significantly improve the signal-to-noise ratio and minimise the influence of environmental magnetic fields on the measurements, the magnetometer should adopt a gradiometric (or differential) configuration. In this context, the expression for the detected magnetic field, presented in Eq. (33), is modified to reflect this approach. In this configuration, two sensor elements are positioned with a defined separation, known as the baseline. The secondary magnetic flux density detected by a first-order gradiometer, assuming that the environmental field is efficiently cancelled out, is described by Equation (41).

$$B_{sz}(x,y,h) = \frac{B_0}{2}V(a,f)\left(\frac{2h^2-x^2-y^2}{(x^2+y^2+h^2)^{\frac{5}{2}}} - \frac{2(h+l_s)^2-x^2-y^2}{(x^2+y^2+(h+l_s)^2)^{\frac{5}{2}}}\right) \tag{41}$$

The peak value of this magnetic field also occurs at x = y = 0. is now given by:

$$B_{smax}\left(h,a,f_{0,}l_s\right) = B_0V(a,f_0)\left[\frac{1}{h^3} - \frac{1}{(h+l_s)^3}\right] \tag{42}$$

In relation to the magnitude of the primary magnetic field and expressing the complex factor $V(a, f_0)$ in terms of its magnitude and phase, to obtain.

$$\frac{B_{smax}(h,a,f_0,l_s)}{B_0} = |V(a, f_0)| \cdot e^{j\varphi(a,f_{0,})} \left[\frac{1}{h^3} - \frac{1}{(h+l_s)^3}\right] \tag{43}$$

3.2
Simulation of the magnetic maps obtained by the Measurement System for different geometries and positions of the foreign body

3.2.1
Computational Modelling of the Primary Field

The Biot-Savart Law is essential for understanding the generation of magnetic fields by electric currents. It allows the calculation of the magnetic induction vector (or magnetic flux density) at a specific point in space from a conductor carrying a steady current. For this, the conductor is considered to be divided into small differential elements *dl*, whose magnitudes correspond to an infinitesimal segment of the wire, and whose direction follows the current flow [2,46,47]. The magnetic field generated by each of these elements is then evaluated with respect to a point **P** through the vector $\vec{r}$, which represents the distance between the wire element and the observation point. The superposition of the effects of these elements along the entire wire allows the determination of the total magnetic field, as illustrated in Figure 5. This formulation is one of the pillars of classical electromagnetism, accurately describing how electric currents generate magnetic fields in the surrounding space.

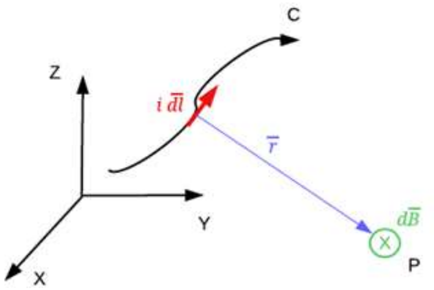

Figure 5 - Geometric representation used for the application of the Biot-Savart Law

Considering an infinitesimal current element i in the direction of $d\bar{l}$, and the vector $\vec{r}$ that connects this element to the point of interest **P**, we can express the infinitesimal contribution to the magnetic flux density. This contribution is determined by the interaction between the electric current and the position of the observation point, taking into account both the magnitude of the current and the geometry of the system.

$$d\bar{B} = \frac{\mu_0}{4\pi} \frac{i \cdot d\bar{l} \times \bar{r}}{|\bar{r}|^3} \tag{44}$$

Thus, by integrating this infinitesimal element $d\bar{B}$ along the conductor **C** that carries the current i, we obtain the total magnetic flux density at point **P**. The total magnetic flux density is expressed by the following relation:

$$\bar{B} = \int_C \frac{\mu_0}{4\pi} \frac{i \cdot d\bar{l} \times \bar{r}}{|\bar{r}|^3} = \frac{\mu_0}{4\pi} \int_C \frac{\mu_0}{4\pi} \frac{i \cdot d\bar{l} \times \bar{r}}{|\bar{r}|^3} \tag{45}$$

Where μ_0 is the permeability of free space $\mu_0 = 4\pi \times 10^{-7}\ \mathrm{T \cdot m \cdot A^{-1}}$, i is the current value in the wire, $d\bar{l}$ is the infinitesimal length element of the conductor, and $\vec{r}$ is the vector that connects the current element to point P. This integral considers the contribution of each segment of the wire to the total magnetic field at **P**, taking into account the direction and distance of each current element.

All the simulations presented in this dissertation, related to the excitation of the foreign object, are based on the Biot-Savart Law. The computational implementation used is detailed next.

3.2.2
Computational Model for the Primary Magnetic Field Analysis

To model the primary magnetic field generated by the coil system, a MATLAB code was developed based on the Biot–Savart Law, which enables the calculation of the magnetic field vector $\vec{B}$ at any point in space, based on the geometry of the coils and the electric current flowing through them.

In this model, two flat circular coils wound in opposite directions, with multiple turns, were considered, arranged coaxially and symmetrically separated relative to the centre of the system, as illustrated in Figure 6. The coils were described as Archimedean spirals, with defined inner and outer radii and a specific number of turns. Each spiral is represented by three-dimensional vectors that describe the position of its infinitesimal length elements $d\bar{l}$ in space.

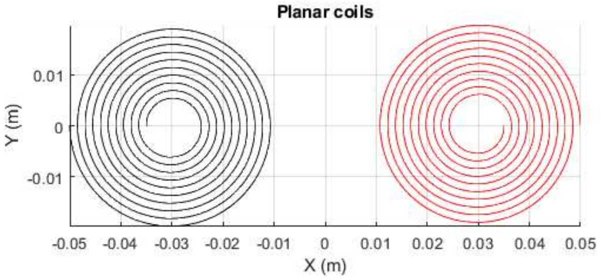

Figure 6 - Planar Coils

The distribution of the field generated by each coil is calculated individually. Then, the total field is obtained by the vector superposition of the individual contributions from each coil. The coordinates of the differential current elements are defined based on the radius of each turn, and numerical integration is performed in three-dimensional space to calculate the components B_x, B_y, B_z of the magnetic field in the region of interest.

The computational implementation considered two coils with opposite windings, positioned symmetrically relative to the central axis of the coordinate system. To ensure proper spatial alignment, linear transformations such as rotations and horizontal translations were applied to their positions.

The magnetic flux density at each point in space was calculated by considering the vector interactions between the infinitesimal current elements and the relative distances to the measurement points, based on the Biot–Savart Law expression as shown in Equation (45). Figure 7 illustrates the distribution of the primary magnetic flux density generated by the modelled coil pair, highlighting the symmetry of the field along the central axis.

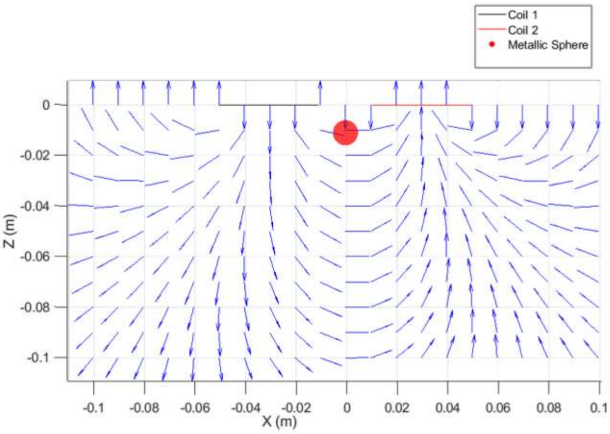

Figure 7 - Spatial Distribution of Primary Magnetic Flux Density

3.3
Theoretical Foundations of Inverse Modelling with Neural Networks

3.3.1
Artificial Neural Networks

The human nervous system is composed of a highly interconnected network of neurons, which represent the basic units of information processing in the brain. As illustrated in Figure 8, each neuron receives signals from other neurons through structures called dendrites, processes this information, and, if the stimulus is strong enough, generates a response through its axon. The connections between neurons, known as synapses, can be modified in their effectiveness through experience, which forms the basis of biological learning [48].

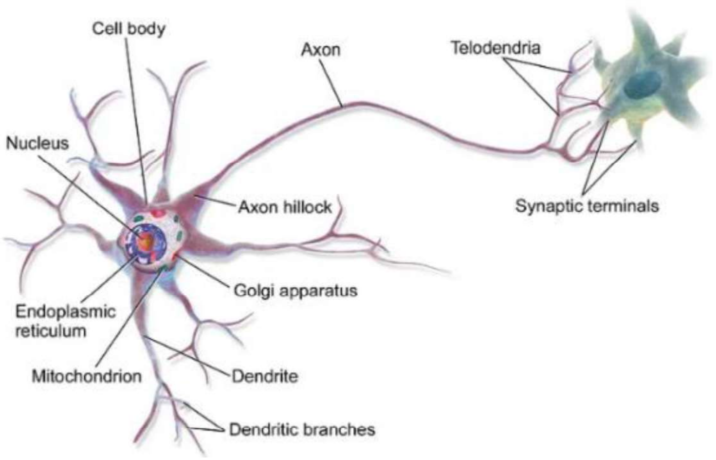

Figure 8 - Representation of a Biological Neuron [49].

This functioning served as inspiration for the development of computational models known as artificial neural networks, which are widely used in solving inverse modelling problems, as illustrated in Figure 9. In these models, the goal is to adjust the internal parameters of an artificial network so that it can estimate or reconstruct physical properties (such as geometry or material) from indirect observations, thereby emulating, to some extent, the adaptive capacity of the human brain.

Artificial neural networks (ANNs) are computational models inspired by the structure and functioning of biological neurons. Their main applications include classification, pattern recognition, time series prediction, and function approximation. The block diagram in Figure 9 shows the model of an artificial neuron with its main components.

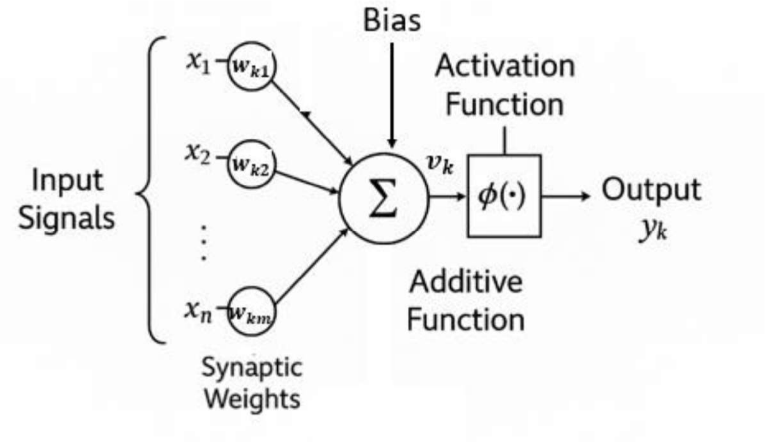

Figure 9 - Model of an Artificial Neuron [50].

The main components of an artificial neuron, are:

- **Inputs ($x_1, x_2, ..., x_m$):** These can be the input patterns to the network or the outputs from neurons in the previous layer.
- **Synaptic weights ($w_{k1}, w_{k2}, ..., w_{km}$):** These represent the strength of each connection. Positive weights (excitatory) increase the neuron’s activation, while negative weights (inhibitory) reduce it.
- **Weighted sum (v_k):** The result of the linear combination of the inputs weighted by their respective weights.
- **Bias term (b_k):** A constant value added to the weighted sum, increasing the flexibility of the model.
- **Activation function ($\emptyset$):** Transforms the weighted sum to limit the neuron’s output.

- **Output (y_k):** The final response of the neuron.

Mathematically, the output of the neuron can be expressed as:

$$\mathcal{Y}_k = \emptyset\left(\sum_{i=1}^{m} w_{ki} x_i + b_k\right) \tag{46}$$

3.3.1.1
Activation Functions

The activation function determines the value of the output of the artificial neuron and, depending on its form (linear or non-linear), influences the network's ability to learn complex patterns [50]. Some common functions are:

- **Linear:**

  $$f(x) = ax \tag{47}$$

  Usually used in the output layer of networks for regression.

- **Step (Threshold):**

  $$f(x) \begin{cases} 1, & x > 0 \\ 0, & x \leq 0 \end{cases} \tag{48}$$

  Applicable in simple binary classifiers.

- **Sigmoid (Logistic):**

  $$f(x) = \frac{1}{1+e^{-x}} \tag{49}$$

  Varies between 0 and 1; useful in binary classifications.

- **ReLU (Rectified Linear Unit):**

  $$f(x) = \max{(0, x)} \tag{50}$$

Transforms the output using the following algorithm:

- If the input value x is less than 0, it returns 0.
- If the input value x is greater than or equal to 0, it returns the input value.

Widely used in deep networks due to computational simplicity and efficiency.

3.3.1.2
Network Architecture

Neural networks can be classified according to their architecture into non-recurrent (feedforward) and recurrent networks [39]:

- **Non-recurrent Networks:** Organised in sequential layers (input, hidden, and output), without feedback between neurons. The structure of these networks can consist of a single layer or multiple layers (Figure 10). Networks with a single layer have an input layer responsible for distributing patterns throughout the network, which is projected onto an output layer. In networks with multiple layers, there is one or more intermediate (hidden) layers between the input and output layers. In these networks, signals flow only in one direction from input to output.

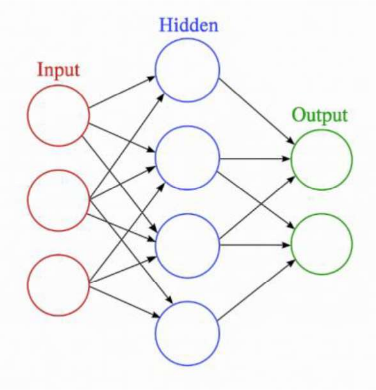

Figure 10 - Example of a non-recurrent network with hidden neurons.

- **Recurrent Networks:** Include feedback connections (Figure 11), allowing the output of one neuron to influence future inputs. These networks are particularly useful for tasks with temporal dependencies. These networks do not have a rigid organisation, and their neurons can connect to any other neuron in the structure, whether from a previous layer or the same layer.

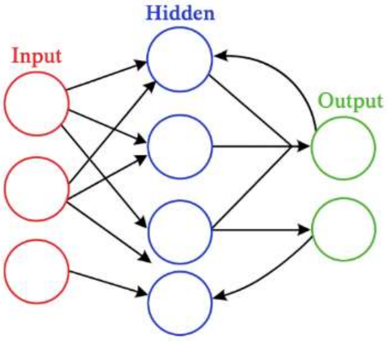

Figure 11 - Example of a recurrent network with hidden neurons.

3.3.1.3
Types of Learning

The learning process in artificial neural networks (ANNs) refers to the adaptation of their free parameters, mainly the synaptic weights and biases, through interaction with the environment and the presentation of data. During this process, the network modifies these parameters with the goal of appropriately representing the patterns present in the provided data. This adaptation is the mechanism by which the network acquires knowledge, and learning is an essential step in the development of any ANN model [50,51].

The type of learning is defined by how the network's parameters are adjusted, and it can be classified into three main categories: supervised learning, unsupervised learning, and reinforcement learning.

- **Supervised Learning:**

In this type of learning, the network is trained using a set of previously labeled examples, meaning that for each input vector, the corresponding expected output is known [48,51,52]. During training, the input vector is provided to the network, which produces an estimated output. This output is then compared with the desired output, and the difference (error) between the two is used to adjust the network's weights in a way that minimises this error.

The most widely used algorithm in this context is Backpropagation, which employs the gradient descent method to efficiently update the network's weights. Supervised learning is especially effective in regression and classification tasks, where the goal is to map a known input to a specific output.

- **Unsupervised Learning:**

Unlike supervised learning, unsupervised learning does not require prior knowledge of the desired outputs. In this case, the network is trained solely based on the inputs, seeking to find structure or patterns in the provided data [48,51,52]. The weights are adjusted so that similar input vectors result in similar outputs, promoting the organisation of data into categories or groups that share common characteristics.

This type of learning is widely used in clustering and dimensionality reduction tasks, with representative algorithms including the Self-Organising Map (SOM) by Kohonen and the Hopfield Network. These algorithms allow the network to automatically identify regularities or statistical distributions in the data, even without prior knowledge of its categories.

- **Reinforcement Learning:**

Reinforcement learning is based on the continuous interaction between an agent and the environment in which it operates. The environment is modelled as a set of states, and the agent, at each state, can choose an action from several available options [48,52]. In response to the action taken, the environment returns a positive or negative reinforcement value that reflects the immediate quality of the decision made. Over time, the agent learns to select actions that maximise the accumulation of these rewards.

The main goal of this process is to minimise a cost function, usually associated with the sum of the costs of actions over time, rather than just the result of a single action. Unlike supervised and unsupervised learning, this method relies on experience gained through repeated interactions with the environment, without relying on labeled data.

In contrast to supervised and unsupervised methods, reinforcement learning is based on perceptions obtained through direct and successive interactions with the environment, making it a more dynamic and adaptive paradigm.

3.3.1.4
Multilayer Perceptron Networks

Multilayer Perceptron (MLP) networks are among the most widely used models within the realm of Artificial Neural Networks. They belong to the class of feedforward networks, meaning they do not contain recurrent connections, and data flows in a single direction: from the input layer to the output layer [39,50].

An MLP is composed of three main parts: an input layer, which receives the data; one or more hidden layers, where intermediate processing occurs; and an output layer, which provides the final result of the network. Each neuron applies a nonlinear activation function, such as the sigmoid function or ReLU, allowing the network to represent complex relationships.

The basic structure of an MLP with a single hidden layer is illustrated in Figure 11, showing the flow of information between the neurons in each layer.

3.3.1.5
Training

The most common training method for MLP-type networks is the Backpropagation algorithm, which operates in a supervised manner and is based on the iterative correction of the errors made by the network [48]. For this, input-output data pairs are presented. The network processes the input data and generates a response, which is then compared to the desired output. The difference between these two responses is interpreted as the error.

This error is propagated back through the layers of the network, in a process known as error backpropagation, and serves as the basis for updating the synaptic weights, with the goal of reducing this error in subsequent iterations. The weight adjustment is guided by the gradient descent method, in which weights are modified in the opposite direction of the error gradient, aiming to minimise the cost function.

The frequency of these updates can vary according to the chosen strategy:

- **Online** (or by default), where weights are updated after each training example;
- **Batch**, where updates occur only after the presentation of all examples in the training set.

Stopping criteria for training may include: reaching an error below a predefined threshold; observing stagnation in error reduction; or completing a maximum number of epochs (complete iterations over the dataset). In practical applications, a combination of these criteria is commonly used [50].

4

Development of the Measurement System Prototype

The instrument developed to locate non-ferromagnetic foreign bodies, such as firearm projectiles, consists of two stages: excitation and measurement, which are described in Sections 4.1 and 4.2, respectively. The excitation of the foreign object is carried out by two planar spiral coils wound in opposite directions, creating an almost circular magnetic flux that passes horizontally through the coils and the target. In the measurement stage, the sensor records the secondary magnetic field generated by these currents. The device electronics and signal processing are covered in Section 4.3, while the creation of the primary magnetic field and the induction of the secondary are discussed in Section 4.4.

4.1

Excitation Component of the Measurement System.

The presented design is based on a measurement system that uses planar spiral coils, as illustrated in Figure 12. These coils were carefully designed to optimise magnetic field detection and are wound in opposite directions, with a distance of 20 mm between them. Each coil has an inner radius of 5 mm and an outer radius of 20 mm, with a track width of w = 0.75 mm and a spacing between tracks of s = 0.83 mm. Additionally, each coil consists of N = 10 turns, considering a maximum excitation current amplitude of 1 A was adopted based on previous studies conducted at the Biometrology Laboratory (PUC-Rio) [2,5]. These works demonstrated that this current amplitude produces a magnetic field intensity within the optimal linear operating range of the GMI sensor (approximately ±1 µT), while avoiding excessive heating of the excitation coils and ensuring compatibility with the current amplifier. Thus, the value of 1 A was maintained as a reference condition for both the simulations and experimental measurements in this study.

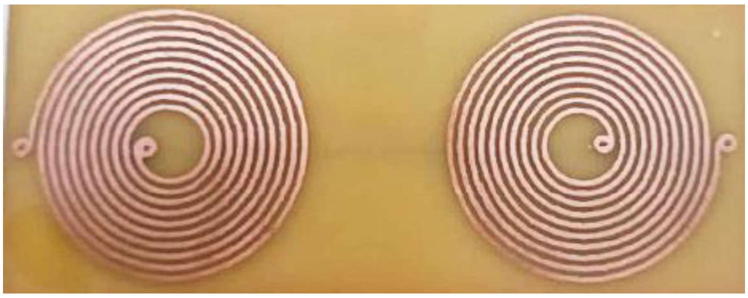

Figure 12 - Planar spiral coils

Both planar spiral coils are powered by sinusoidal currents with a frequency of 8 kHz was selected because it lies within the optimal operational bandwidth (0.1–10 kHz) of sensor. Characterisation experiments demonstrated that at this frequency, the sensor maintains high linearity up to 1.3 μT with a sensitivity of approximately 5 V/μT, ensuring a good signal-to-noise ratio. Additionally, the signal conditioning filter was designed with a central frequency of 8 kHz to match the sensor's best performance region, maintaining the same intensity but in opposite directions. This configuration generates a horizontal magnetic field, resulting in high intensity in the region of the foreign body. In contrast, the magnetic field intensity in the area where the GMI sensors are located remains very low, as already shown in Figure 7.

4.2
Detection Component of the Measurement System

In this system, two GMI sensors are used, each positioned near each one of the coils. This arrangement allows each sensor to capture the variations in the magnetic field generated by its respective coil, thus improving the accuracy and sensitivity of the measurements. Figure 13 illustrates the experimental setup, showing the spiral coils and the positioning of the GMI sensors relative to them. The sensors are arranged parallel to the coils, which is essential for maximising the detection of foreign bodies, ensuring they are properly aligned with the generated magnetic fields.

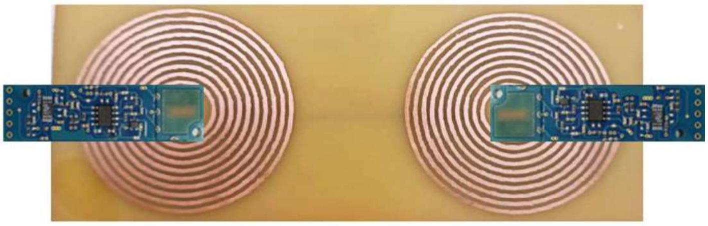

Figure 13 - Positioning of the sensors parallel to the coils

Figure 14 presents the actual physical structure developed for the experiments. Figure 15a shows a top view of the GMI sensors, while figure 15b provides a front view highlighting the positioning of the planar coils and the GMI sensors in the final configuration.

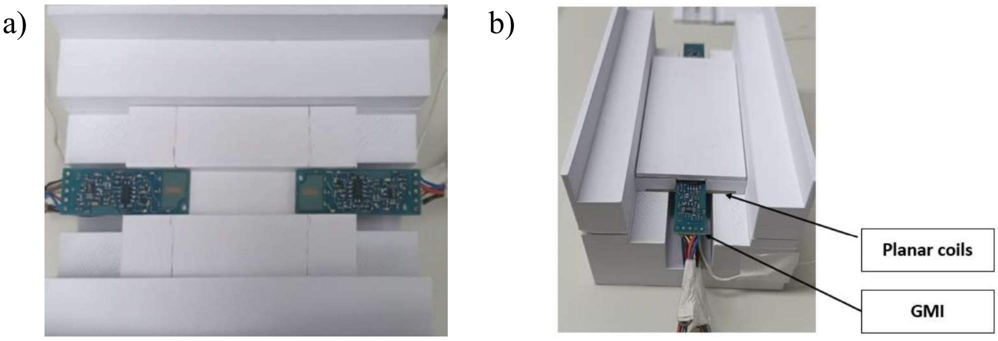

Figure 14 - Final assembly of the experimental setup: (a) top view of the mounted spiral coils and GMI sensors, (b) front view highlighting the positioning of the planar coils and the GMI sensors.

4.2.1
GMI Sensor

The presented design is based on a GMI sensor manufactured by Aichi Micro Intelligent Corporation, model MI-CB-1DJ-M-B. Aichi offers two versions of each sensor, depending on the number of sensing elements used: single-type and multi-type. The single-type sensor includes an integrated oscillator that excites the sensing element, whereas the multi-type requires an external oscillator to synchronise two or more sensors. The oscillators are designed to generate square waves with a 50 % duty cycle and a voltage range from 0 V to 5 V, operating at a frequency of 1 MHz with a sensitivity of 5 V/µT and capable of measuring magnetic flux densities on the order of 15 pT. For the implementation of a first-order gradiometer, the multi-type version was selected [3,40].

Additionally, Aichi manufactures sensors with two possible detection directions: A (figure 15a, perpendicular to the length of the circuit board) and B (figure15b, parallel to the length of the circuit board). Direction B (figure 15b) was chosen as it is more suitable for measurements along the z-axis.

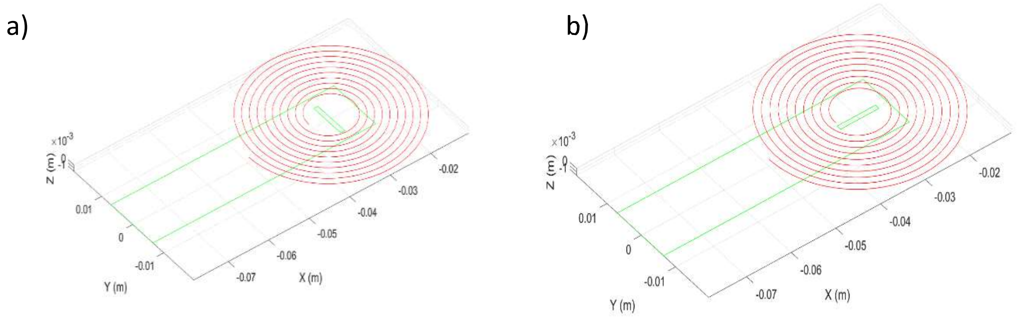

Figure 15 - shows both orientations, where (a) corresponds to direction A (perpendicular) and (b) to direction B (parallel).

The GMI sensor features small dimensions (1.2 mm × 13.5 mm) and operates at room temperature, measuring the magnetic flux density parallel to its length. Figure 16 presents a simplified diagram with the dimensions of the Aichi MI-CB-1DJ-M-B prototype GMI sensor, while shows an image of the sensor itself. These visual representations are essential for better understanding the physical characteristics and configuration of the sensor [40].

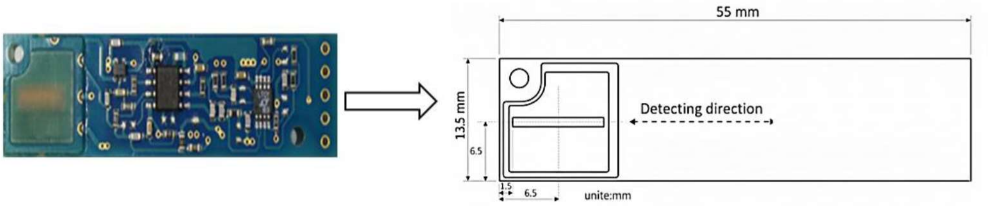

Figure 16 - Simplified diagram showing the dimensions of the Aichi MI-CB-1DJ-M-B prototype GMI sensor.

Table 3 summarises the technical specifications of the Aichi Model MI-CB-1DJ-M-B sensor, a device designed for magnetic field detection applications. This sensor stands out for its high sensitivity and ability to operate at low frequencies, making it ideal for locating non-ferromagnetic metallic bodies. The information in Table 3 includes crucial details such as sensitivity, operating range, and the physical characteristics of the sensor, all of which are essential for understanding its performance in practical environments.

In addition, the sensor exhibits a typical noise level ranging between 0.3 nT and 1 nT peak-to-peak, with a noise density of $10\ \frac{pT}{\sqrt{Hz}}$. These noise levels are considered quite low for devices of this type, contributing to more accurate measurements. The main component of the observed noise is $\frac{1}{f}$ noise, often referred to as pink noise, which is common in electronic devices and can affect measurement accuracy in certain frequency ranges.

The use of appropriate filters that allow only selected higher frequencies to pass can significantly reduce the noise level. This approach is fundamental to improving the resolution of the foreign body detection system. By eliminating unwanted components and low-frequency noise, filters help to emphasise relevant signals, resulting in more accurate and reliable measurement results. Therefore, the implementation of suitable filtering techniques not only enhances signal quality but also boosts the effectiveness of the system in identifying and locating non-ferromagnetic metallic objects.

Table 3 – Technical specifications of the Aichi Model MI-CB-1DJ-M-B sensor.

Parameter	**Measurement Condition**	**Values**			**Unit**
		Min	**Typical**	**Max**	
Power supply voltage	-	-0.3	15	20	V
Output saturation voltage	1 Hz sine wave with amplitude of 1 µT	-	14.9	-	V
Normal output voltage	0 µT	6.4	7.1	7.8	V
Operating current	0 µT, no load		16		mA
Frequency response	-3 dB	0,1		10000	Hz
Operating temperature		-20		50	
Linear detection range	±30 µT (DC Field)		±1,0		µT
Noise density	In air, 1 Hz		10		10 pT/√Hz

Linear operating range	In air, ±30 µT (DC Field)	-1		+1	µT
		-10		+10	mOe
Full-band resolution (Peak-to-peak noise)	In air, 1 Hz		±0,3	1	nT
			±3	±10	µOe
Sensitivity	In air, 10 Hz	4.5	5	5.5	V/µT
		0.45	0.5	5.5	V/mOe

The choice of GMI sensors is crucial to ensure effective detection of non-ferromagnetic metallic objects, as they are capable of responding quickly to changes in the magnetic field. The configuration of the coils and the use of GMI sensors ensure that the system operates within the ideal parameters for accurate detection of foreign bodies. This approach not only maximises the system's efficiency but also provides better spatial resolution in the measurements, which is essential for applications in environments where precise object identification is critical.

4.3
Signal Conditioning and Processing Circuit for Gradiometric Measurement

The primary components required for the operation of a GMI-based detection system include band-pass filters for the sensor outputs and an instrumentation amplifier responsible for gradiometric reading and signal amplification. The use of more selective filters is particularly important in this context, as the lower excitation frequency and absence of DC bias demand greater attention in signal filtering.

The analysis of simulation results from previous studies, particularly those presented by [5], guided the selection of the topology implemented in this work. Figure 17 illustrates a block diagram of the main functional blocks of the proposed system.

In that study, different circuit configurations were analysed to evaluate the influence of phase mismatches between the primary and secondary magnetic fields (ϕpri and ϕsec), as well as the effect of using precision full-wave rectifiers before

the instrumentation amplifiers.
The simulations demonstrated that, although rectifiers can mitigate systematic errors associated with ϕpri mismatches, they distort the amplitude–phase relationship linked to ϕsec, which compromises the accurate estimation of the secondary magnetic flux density.
Based on these findings, the present work adopts a non-rectified configuration, preserving the unaltered signal amplitude before gradiometric processing.

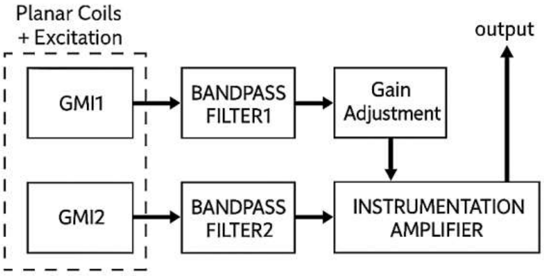

Figure 17 - Block diagram of the implemented circuit.

The excitation of the planar coils controls the frequency (f_o) and amplitude (I_o) of the coil current, being responsible for generating the primary magnetic field. The GMI excitation uses a 15 V power source. Band-pass filters, centred at f_o, are used to eliminate most environmental interferences and minimise electronic noise, especially the $\frac{1}{f_o}$ noise present in the sensor elements. This strategy results in a significant improvement in the signal-to-noise ratio, enabling higher resolution.

The gain adjustment block consists of a controllable gain applied to the filter output, aiming to equalise the amplitude responses between filters, considering non-ideal characteristics that may differ between them. This stage is crucial in the intermediate processing of the system.

The instrumentation amplifier ideally performs the subtraction between input signals while introducing gain. With GMI sensor 1 positioned closer to the foreign body and GMI sensor 2 placed at a distance (l_s) from the baseline of GMI 1, as Figure 18, this configuration characterises a first-order gradiometer, where the output is proportional to the secondary magnetic flux density.

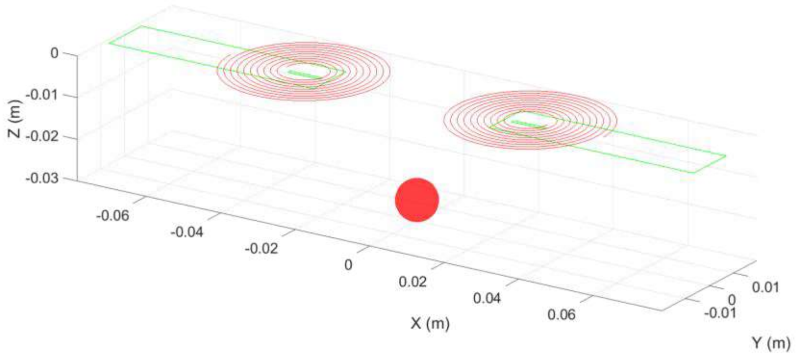

Figure 18 - Schematic representation of the sensor and coil arrangement for gradiometric measurement

These concepts and the developed circuit were adapted from the preliminary previous work conducted by [3], which explored similar systems for detecting non-ferromagnetic metallic foreign bodies, based on eddy currents and GMI magnetometers.

4.3.1
Band-Pass Filter Topology

In order to increase the filter's selectivity without compromising the gain in the passband, fourth-order Butterworth filters were adopted, known for their flat response in the passband. These filters were implemented using the Voltage-Controlled Voltage Source (VCVS) topology, also known as the Sallen-Key configuration. Figure 19 shows the structure of a second-order band-pass filter using this topology.

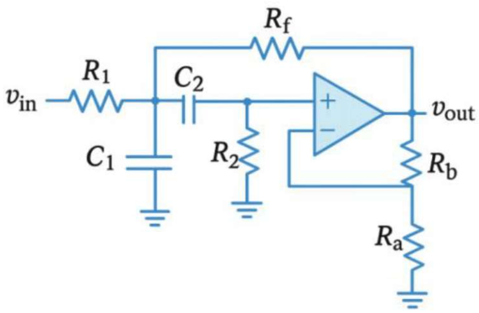

Figure 19 - *VCVS band-pass filter topology (second order)*

To achieve the desired order, two second-order stages were connected in cascade, resulting in a fourth-order filter.

The transfer function of the filter topology is given by:

$$\boldsymbol{H(s)} = \frac{\left(1+\frac{R_b}{R_a}\right)\frac{s}{R_1C_1}}{s^2\left(\frac{1}{R_1C_1}+\frac{1}{R_2C_1}+\frac{1}{R_2C_2}-\frac{R_b}{R_aR_fC_1}\right)s+\frac{R_1+R_f}{R_1R_fR_2C_1C_2}} \tag{51}$$

The centre frequency f_o is given by:

$$f_o = \frac{1}{2\pi}\sqrt{\frac{R_1+R_f}{R_1R_fR_2C_1C_2}} \tag{52}$$

The quality factor (Q):

$$\boldsymbol{Q} = \frac{\sqrt{(R_1+R_f)R_1R_fR_2C_1C_2}}{R_1R_f(C_1C_2)+R_2C_2\,(R_f-R_1R_b/R_a)} \tag{53}$$

To ensure stability, the gain $\left(1+\frac{R_b}{R_a}\right)$ must be less than 3. However, a gain close to 1 is preferred, considering the possibility of saturation at the output of the instrumentation amplifier.

4.3.2
Prototype Configuration

To compensate for the gain variations of the filter at the new excitation frequency of 8 kHz, a passive gain compensation block was incorporated. This adjustment is performed using a resistive divider, whose output can be regulated through a potentiometer. Figure 20 illustrates the schematic diagram of the prototype developed for the localisation system.

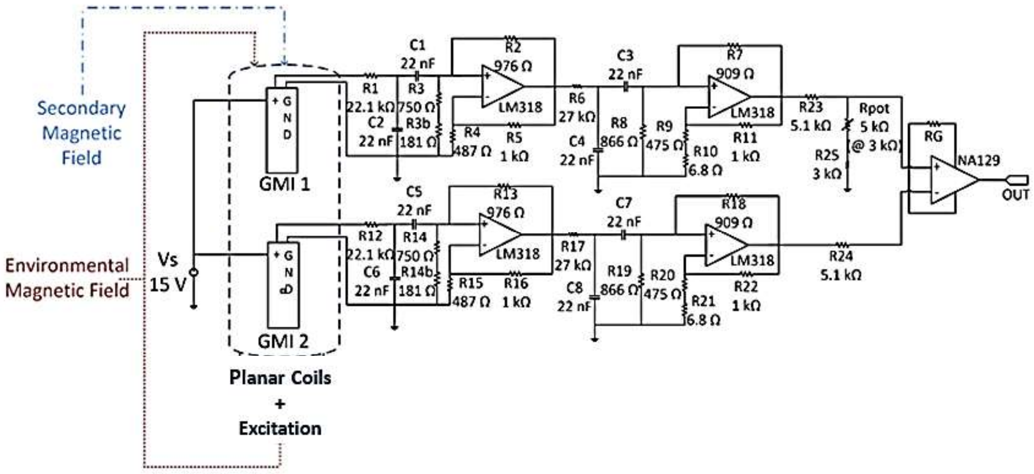

Figure 20 - Schematic for the detection system prototype. Adapted to [5]

The resistive divider, composed of R23–R25 and a 5 kΩ trimmer potentiometer, allows fine adjustment of the signal amplitude to equalise the outputs of both filter channels. This adjustment ensures that, under the presence of only the primary magnetic field, the voltages from GMI_1 and GMI_2 are matched, minimising the common-mode component at the instrumentation amplifier input. Consequently, the gradiometric output becomes more sensitive to the secondary magnetic flux density induced by the metallic target.

The physical implementation of the signal conditioning circuit is shown in Figure 21, highlighting the main components described in the schematic diagram.

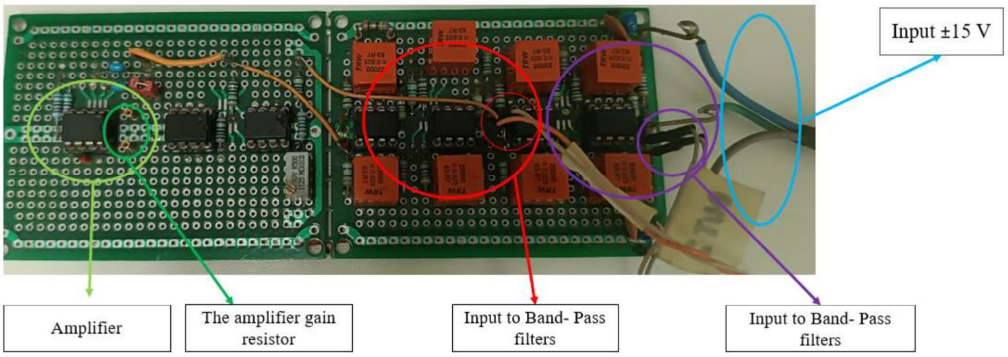

Figure 21 - Signal conditioning circuit board

The outputs of each GMI sensor are connected to fourth-order band-pass filters, responsible for suppressing unwanted signal components. The filtered signals are then applied to the input of an instrumentation amplifier, used to perform the gradiometric reading. The gain resistor of the amplifier can be replaced as needed, allowing adjustments to the measurement range. Since the GMI sensors operate with a 15 V DC power supply, the amplifiers are powered with ±15 V.

4.3.3
INA129 Instrumentation Amplifier

In the experiments conducted in this work, the INA129 instrumentation amplifier, manufactured by Texas Instruments, was used. This component was chosen for offering key features for low-amplitude signal measurements, such as low offset voltage, wide power supply range, high common-mode rejection, and good bandwidth even at high gain levels.

The operation of the amplifier can be described by a general equation in which the output depends on the difference between the input voltages V_{in+} and V_{in-}, multiplied by the differential gain G_{dif} , added to the contribution of the average of the inputs weighted by the common-mode gain G_{cm}:

$$V_0 = G_{dif}(V_{in+} - V_{in-}) + G_{cm}\frac{(V_{in+} + V_{in-})}{2} \tag{54}$$

The differential gain G_{dif} is determined by:

$$G_{dif} = 1 + \frac{49{,}4\ k\Omega}{R_G} \tag{55}$$

where R_G is the external resistor that defines the amplifier gain (Figure 26).

According to the manufacturer's datasheet, the INA129 supports gains of up to 1000 V/V for signals with frequencies up to 10 kHz. At higher frequencies, the bandwidth is reduced, with the maximum gain being around 100 V/V for signals at 100 kHz.

The datasheet also provides Common Mode Rejection Ratio (CMRR) graphs as a function of frequency and differential gain values. The relationship between CMRR (in decibels) and the amplifier gains (in V/V) is given by:

$$CMRR = 20log_{10}\left|\frac{G_{dif}}{|G_{cm}|}\right| \tag{56}$$

Around 8 kHz, CMRR values range from 50 dB to 110 dB, being higher for greater differential gains. This means the differential gain can be, at a minimum, 316 times higher than the common-mode gain. However, for higher frequencies, such as 100 kHz, CMRR tends to drop to the range of 30 to 70 dB, reducing common-mode noise rejection.

Furthermore, the maximum excursion of the signal of interest, limited by output saturation, can be estimated using equation (55).

4.4
Structure of the Primary and Secondary Field

A plastic support was built to integrate the coil PCB and secure the sensors at the centre of the coils, where the magnetic field is nearly zero. The support was designed using Onshape software and manufactured with the aid of a 3D printer, as illustrated in Figure 22, which highlights its functionality and design.

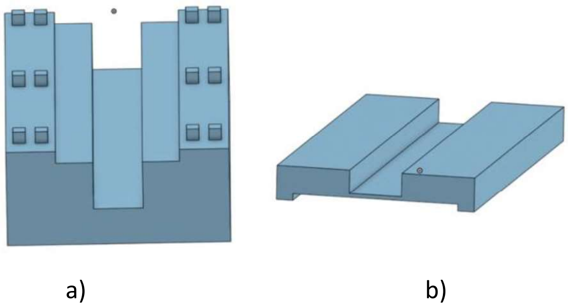

Figure 22- Support structure built with the aid of a 3D printer: (a) base for the PCB and cables, (b) top piece for sensor placement.

The structure of the support, illustrated in Figure 27, is composed of two main parts. The first part is the larger base (figure 27a), designed to accommodate the cables and serve as a mount for the second piece. The second piece has two distinct faces (figure 27b): on one side, the bottom face, the printed circuit board (PCB) is mounted, while on the opposite face, the two sensors are positioned, one on each side of the coil. This configuration ensures that the sensors are properly aligned with the coils, optimising the detection of the magnetic field. Thus, the support was designed to provide efficient organisation of the components and to facilitate the necessary connections for the system’s operation.

Following the description of the mechanical support, Figure 23 presents the experimental configuration adopted. In Figure 23(a), the relative positioning of the excitation coils and the GMI sensors is shown, arranged in a gradiometric configuration with distance l_s indicated between them. In Figure 23(b), a detail of the symmetric alignment of the sensors with respect to the planar coils is highlighted, ensuring the differential measurement condition (Figure 23).

Figure 24 illustrates the final configuration employed for the detection tests of non-ferromagnetic metallic bodies. In this configuration, the foreign body is positioned at a predefined distance from the sensor plane, with a representative test diameter considered in the experiments, serving as a reference for the validation of the proposed method.

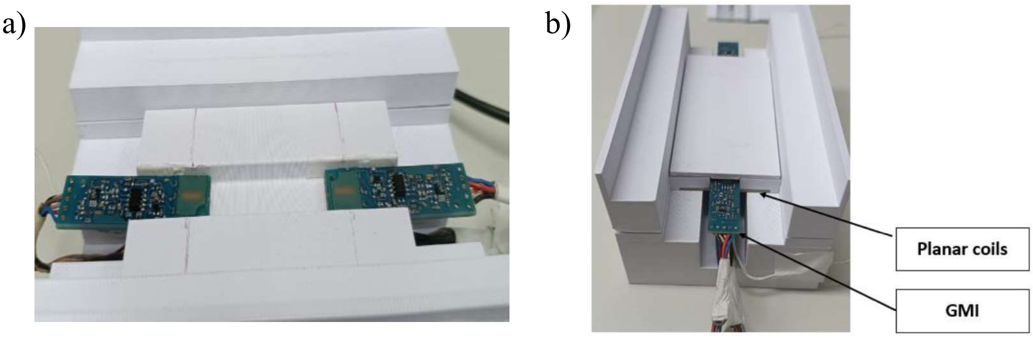

Figure 23 - Experimental configuration: (a) Positioning of the excitation coils and GMI sensors in gradiometric configuration with distance $\mathbf{l_s}$; (b) Symmetric alignment of the sensors with respect to the planar coils.

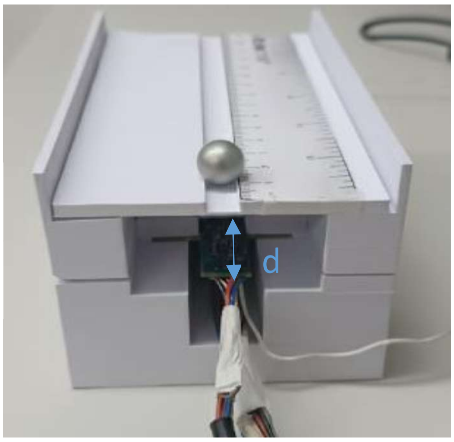

Figure 24 - Final experimental setup: Positioning of the non-ferromagnetic metallic object at a predefined distance **d** from the sensor plane, considering a representative test diameter of the body.

5
Results

This chapter presents the most significant results obtained through program simulations and experiments conducted with the proposed system for detecting non-ferromagnetic metallic objects, using GMI sensors in combination with planar spiral coils. The findings are divided into three main sections: (i) simulated and experimental response of the primary magnetic field produced by the coils; (ii) simulated and experimental response of the secondary magnetic field in the presence of a lead metal sphere; and (iii) use of inverse solution methods for estimating physical characteristics of the detected objects, such as diameter and distance.

5.1
Simulation of the Primary Magnetic Field

The simulation of the primary magnetic field was carried out with the aim of characterising the spatial distribution of the field generated by the spiral coils used in the experiment. MATLAB software was used to implement a model based on the Biot–Savart Law, considering the actual geometric arrangement of the system.

The results show that the magnetic field exhibits an alternating pattern along the X-axis, with two symmetrical positive peaks and a two symmetrical negative peak in the central region (Figure 25). This configuration results from the superposition of the fields generated by the two coils supplied with an alternating current of 1 A.

The magnetic flux density reaches values greater than 179 µT (in magnitude) at a depth of 6.3 mm, indicating a strong field concentration in the region of interest for detection.

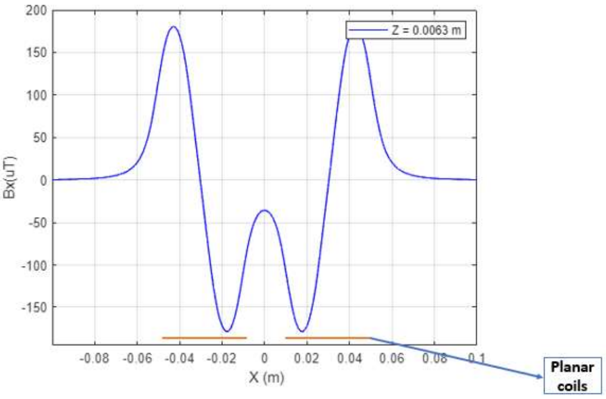

Figure 25 - Distribution of the primary magnetic flux density along the X-axis, highlighting the symmetrical peaks and the variation in magnetic field intensity.

5.2
Experimental Results of the Primary Magnetic Field

The experimental setup employed a sensor used to measure the primary magnetic field along a linear path, as is illustrated in Figure 26. During the experiment, the planar spiral coils were moved in a linear scan from left to right, while the GMI sensor remained fixed.

This procedure enabled the recording of variations in magnetic flux density generated by the coils along the path, under a 1 A direct current (DC) excitation.

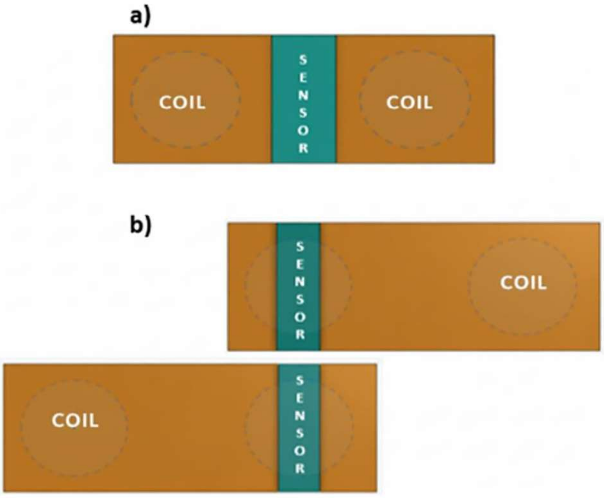

Figure 26 - Experimental setup for evaluating the primary magnetic field, indicating the position of the coils related to the fixed sensor position: (a) overview of the experimental system; (b) positioning the sensor, with linear scanning of the planar spiral coils.

The experimental results confirmed the simulation predictions. As illustrated in Figure 27, an alternating pattern in the direction of the magnetic flux density along the X-axis was observed, reproducing the expected pattern, with two symmetrical positive peaks and a more pronounced negative peak in the central region.

The experimental measurements recorded a maximum intensity of the primary magnetic flux density exceeding 173 µT at a depth of 6.3 mm, validating the accuracy of the simulation model.

However, small deviations from zero magnetic flux density were observed near x= 0.03 m, which can be attributed to slight misalignments between the coils or to measurement noise. These minor imperfections slightly affect the symmetry of the primary magnetic field distribution but do not compromise the overall agreement between experimental and simulated data.

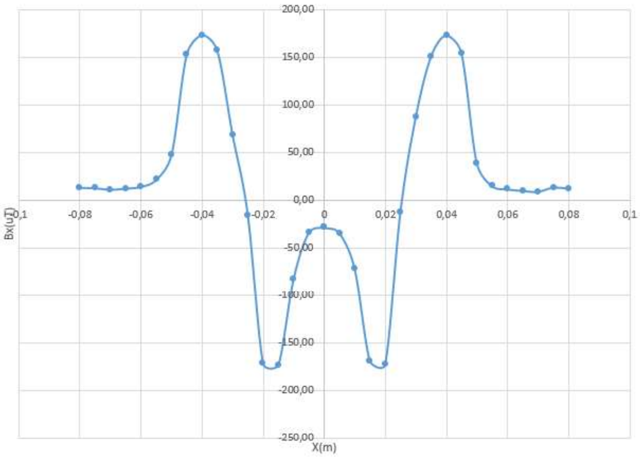

Figure 27 - Experimental results of the primary magnetic flux density along the X-axis, highlighting the correspondence with the simulated data.

To quantify the correlation between the simulated and experimental results, Figure 28 presents a direct comparison between both distributions. The alternation of the magnetic field, the location of the peaks, and the maximum values obtained demonstrate strong agreement, with small relative discrepancies. The quantitative comparison between the simulated and experimental values was performed using the calculation of the percentage error, as expressed by the following equation:

$$Percentage\ Error = \frac{|Simulated\ Value - Experimental\ Value|}{Simulated\ Value} \times 100 \tag{57}$$

By applying this formula, the difference between the simulated magnetic flux density (179 µT) and the experimentally measured value (173 µT) results in a percentage error of approximately 3.35 %.

This analysis demonstrates that the absolute error is small (6 µT) and that the relative error is well below the commonly accepted threshold of 5 % for experimental validations in the field of magnetic instrumentation.

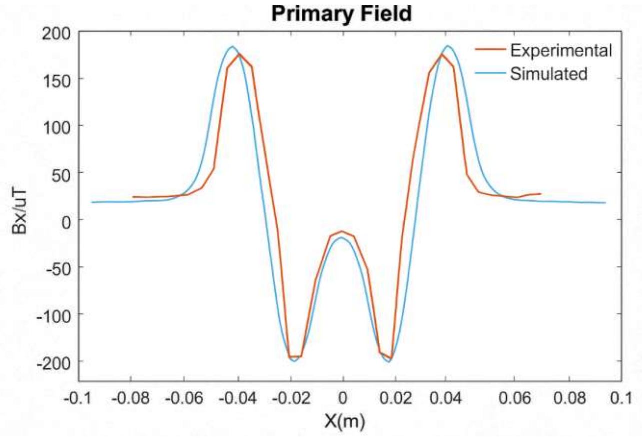

Figure 28 - Comparison between simulated and experimental results of the primary magnetic flux density distribution along the X-axis.

Thus, the results obtained highlight not only the robustness of the theoretical modelling employed but also the high reliability of the experimental procedures and the measurement instruments used in this study.

This solid validation of the primary magnetic field provides a reliable foundation for the continuation of the experiments involving the analysis of the secondary magnetic field and the application of inverse problem-solving techniques, which will be discussed in the following sections.

5.3
Conceptual Simulation of the Secondary Magnetic Field

The evaluation of the secondary magnetic field (Figure 29) generated by the eddy currents induced in non-magnetic metallic foreign bodies revealed distinct behaviours for the GMI sensor in horizontal , demonstrating the effectiveness of this new approach for locating such foreign bodies at different depths in the human body [2]

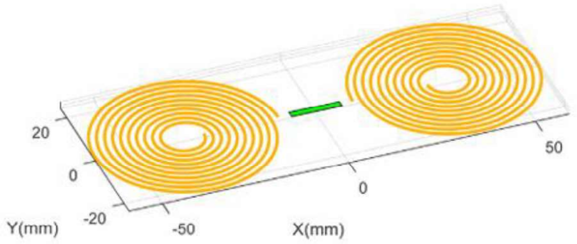

Figure 29 - the foreign body location system, with planar coils and with the GMI sensor oriented horizontally [2]

For spiral coils configuration, along a straight line parallel to the X-axis at Z = 0 (Figure 30), the secondary magnetic flux density exhibits three-pole behaviours, symmetric about the longitudinal axis, with a maximum at the location of the foreign body (X = 0 mm).

To evaluate the effect of the object's depth, simulations were carried out for three distinct depths (20 mm, 40 mm, and 60 mm), enabling the analysis of how the secondary magnetic field varies with the distance between the sensor and the metallic body.

For shallow depths (20 mm), adjacent amplitudes can become negative, generating a five-pole pattern, which transitions to a three-pole configuration as the distance from the sensor increases. Decreasing the sensor-to-object distance reduces the peak width, concentrating the flux near the longitudinal axis. Depth strongly influences the field magnitude: for a 5 mm diameter object, B_{sx} decreases approximately twentyfold when depth increases from 20 mm to 40 mm, and tenfold from 40 mm to 60 mm. Similarly, larger object radii produce higher amplitudes and variations, with a decrease of 3–4 times in magnitude for every 5 mm reduction in radius. These trends were observed in the previous study [2].

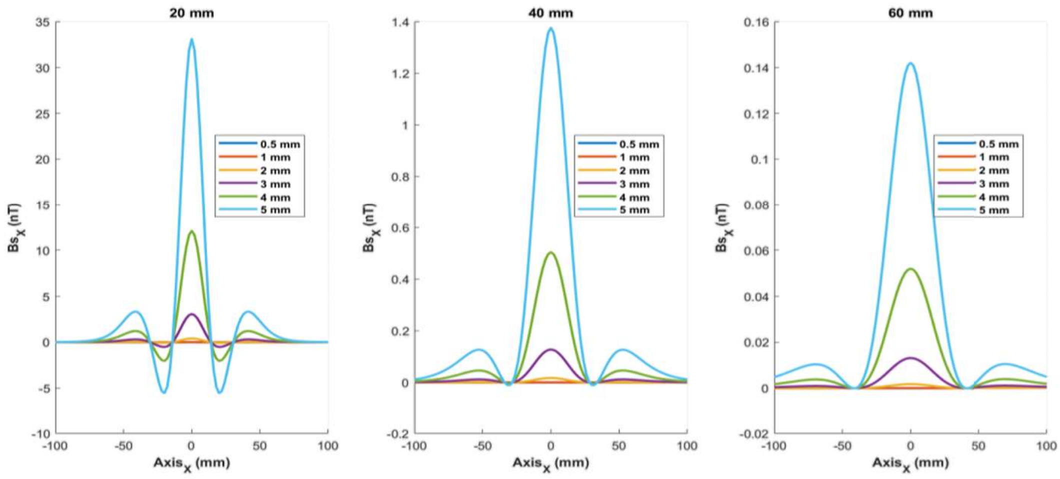

Figure 30 - The secondary magnetic flux density in the region of the foreign body location according to the $\boldsymbol{B_{px}}$ excitations produced for spiral coils configuration [2].

5.4
Experimental Results of the Secondary Magnetic Field: GMI Sensor Performance

However, the experimental tests revealed a significant limitation: the GMI sensor reached saturation. This effect was attributed to the strong influence of the primary magnetic field, whose intensity exceeded the sensor's measurement range. As a result, it was not possible to null the measured field at the expected central position between the planar spiral coils and aligned along the X-axis, where the secondary component should theoretically vanish according to the simulation presented in Section 5.3.

This observation demonstrates that, in practice, the GMI sensor primarily detected the dominant primary field component, preventing the proper measurement of the weak secondary magnetic field. This limitation highlights the constraints of the current experimental setup (Figure 31).

Given this limitation, it becomes pertinent to consider the study [5], which proposes a differential gradiometric reading system composed of two sensors, capable of suppressing the primary component and isolating the secondary response.

Figure 31 - Experimental setup showing the planar spiral coils and the GMI sensor oriented horizontally.

5.5

Simulation of the Secondary Magnetic Field: Differential Gradiometric Measurements

This section presents the simulation of the secondary magnetic field generated by the system structure in the presence of a non-ferromagnetic metallic body, carried out in MATLAB using the same geometric model of coils and sensors previously described.

The simulated system consists of two main coils, powered with a sinusoidal current of 1 A at 8 kHz, and GMI sensors positioned parallel to the coils, as shown in Figure 32, a gradiometric configuration essential for analysing and optimising the detection of disturbances in the magnetic field.

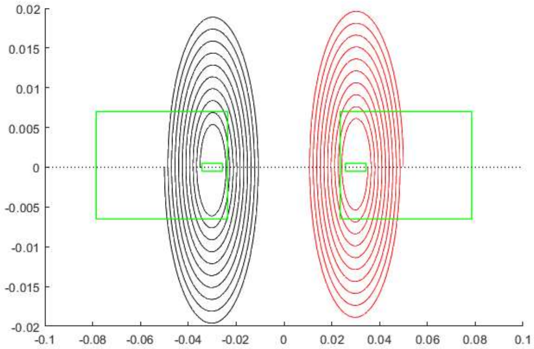

Figure 32 - Positioning of the GMI sensors relative to the planar spiral coils.

The presence of the foreign object was modelled as a lead (Pb) metallic sphere, with electrical conductivity $\sigma = 4{,}55 \times 10^6 \; S/m$ and magnetic permeability close to vacuum ($\mu \approx \mu_0$).

The numerical implementation was carried out in MATLAB, using the analytical formulation of the eddy current problem in metallic spheres subjected to time-varying magnetic fields. Equations (39) and (40) were solved computationally to determine the induced magnetic moment and the corresponding secondary magnetic field at each spatial point.

The simulation involved discretizing the space around the sphere and evaluating the perturbation produced in the primary magnetic field, allowing the determination of the distribution of the secondary magnetic field detectable by the GMI sensors. In particular, the simulation considered a three-dimensional grid of points to evaluate the resulting magnetic field around the sphere and its variation over the sensors.

Figure 33 shows the simulated spatial distribution of the magnetic flux component, illustrating the perturbations introduced by the lead sphere.

It is observed that the metallic body generates local disturbances in the field, particularly in the central region of the measurement system, highlighting the method's effectiveness for detecting foreign metallic objects.

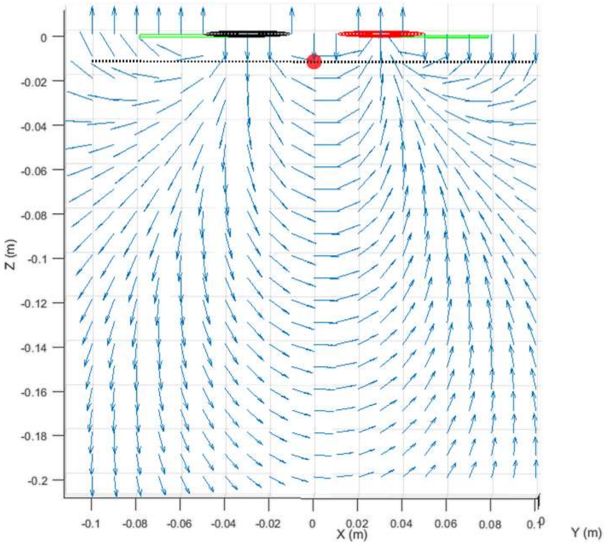

Figure 33 - Distribution of the magnetic flux component generated by a lead sphere positioned at the centre of the measurement system.

The lines and vectors indicate the direction and intensity of the resulting magnetic field, highlighting the disturbance caused by the foreign body within the measurement system.

In addition to the vector analysis of the spatial distribution of the secondary magnetic field, the simulated B_{sx} component was extracted along a linear path parallel to the X-axis, at the position Y=0 and at a fixed distance in Z. Figure 34 presents the variation of the simulated secondary magnetic field B_{sx} along this path.

Four main peaks can be observed, corresponding to the regions where the secondary field generated by the metallic sphere reaches its maximum typically when the sphere is aligned with the edges of the coils.

Between the peaks, the intensity of the secondary field decreases significantly, approaching zero, an expected behaviour, when the sphere is positioned in the central region between the coils, where the magnetic contributions cancel each other out.

This result provides the theoretical prediction of the system's response under ideal conditions, which will later be compared with the experimental data obtained from the real system.

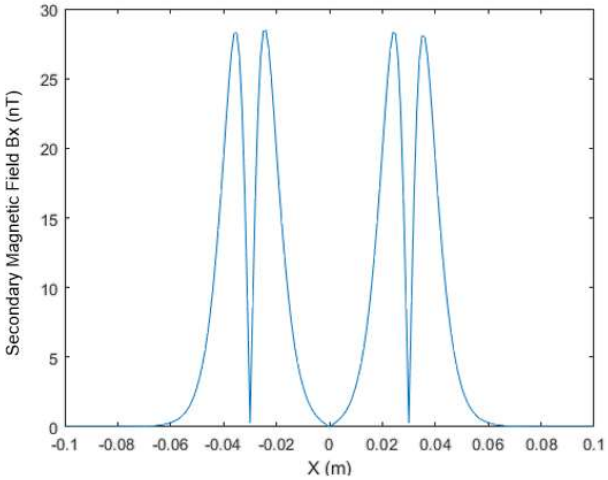

Figure 34 - Simulated response of the secondary magnetic field $\boldsymbol{B_{sx}}$ along the X-axis for a lead sphere positioned at the centre of the measurement system.

5.6
Experimental Results Secondary Magnetic Field: Differential Gradiometric Measurements

The experimental setup used to measure the secondary magnetic field is illustrated in Figure 35.

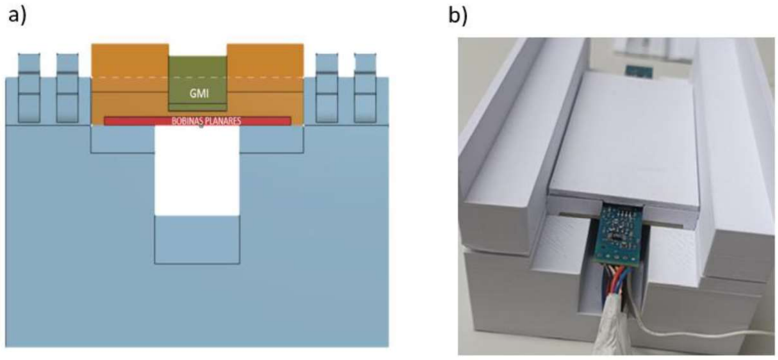

Figure 35 - Experimental setup for the evaluation of the secondary magnetic field: (a) shows a simplified diagram of the system configuration, highlighting the positioning of the GMI sensors and planar coils. (b) shows the actual assembly of the experimental setup with the sensors fixed according to the proposed model.

The signals from the GMI sensors, after the amplification stage, were initially expressed in terms of root mean square (RMS) voltage. To convert these values into magnetic flux density, the RMS values were first converted to peak values (by multiplying by $\sqrt{2}$), Subsequently, the values were normalised by the gain applied in the circuit and the sensitivity of the system ($5\frac{V}{nT}$) according to the equation:

$$\boldsymbol{B}_{\boldsymbol{X}(\mathbf{nT})} = \frac{\boldsymbol{V_{rms}} \times \sqrt{2}}{5 \times \boldsymbol{G}} \tag{58}$$

where *G* is the gain applied in the respective measurement.

This approach allowed for estimating the amplitude of the secondary magnetic field generated by the metallic spheres based on the experimentally measured voltages.

Measurements were conducted using lead (Pb) spheres with diameters ranging from 3 to 11 mm, at distances (*d*) of 6 mm and 9 mm. The gains used in the experiments were set to 1, 10, and 20 V/V. The experimental setup used for these measurements is shown in Figure 36. Figure 36a depicts the positioning of the lead sphere with respect to the excitation coils and the sensing elements. Figure 36b illustrates the procedure adopted for measuring the secondary magnetic field, where the sphere was linearly displaced above the sensors, performing a scan that enabled the acquisition of the characteristic peaks, at a specific distance (*d*).

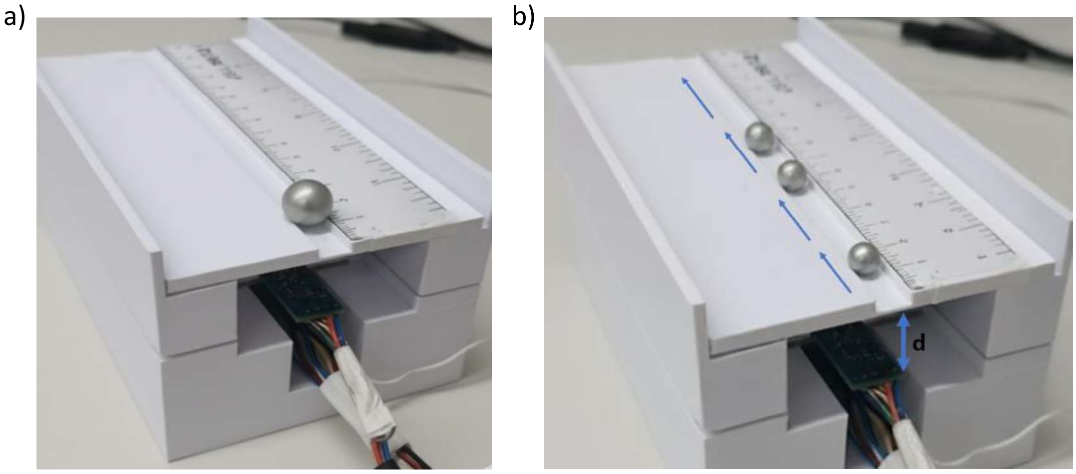

Figure 36 – (a) Experimental setup for measuring the secondary magnetic field with the sphere in place. (b) Schematic representation of the linear displacement of the sphere relative to the excitation coils and sensing elements, indicating the different measurement positions at a distance d.

In the following section, the results are presented according to the gain applied to the readout circuit, showing the four characteristic peaks of the secondary magnetic field as a function of sphere diameter for each fixed distance, which corresponds to the distance between the lead sphere and the detecting sensors.

5.6.1
Results with gain of 1 V/V

Table 4 presents the peak values of the measured secondary magnetic field for different diameters of lead spheres with a constant distance of 6 mm and a gain of 1 V/V. A characteristic pattern of four peaks is observed, which is associated with the position of the sphere relative to the sensitive region of the GMI sensors.

Table 4 – Peak amplitudes of the secondary magnetic field for a gain of 1 and 6 mm distance, considering a set of lead spheres with diameters from 4 mm to 11 mm.

Diameter (mm)	Distance (mm)	Gain (V/V)	Peak1 (nT)	Peak2 (nT)	Peak3 (nT)	Peak4 (nT)
11.0	6.0	1	368.46	368.57	301.79	302.87
10.0	6.0	1	340.85	341.50	277.30	277.53
9.0	6.0	1	279.79	278.15	226.44	226.67
8.0	6.0	1	183.74	186.87	150.73	153.27
7.0	6.0	1	129.17	128.69	109.09	108.50
6.0	6.0	1	72.55	73.37	53.57	53.71
5.0	6.0	1	35.61	35.58	28.23	27.78
4.0	6.0	1	8.97	8.88	6.36	6.31

Figure 37 presents the eight signals depicted in Table 4, showing that peak intensity increases proportionally with sphere diameter due to stronger interaction with the excitation field.

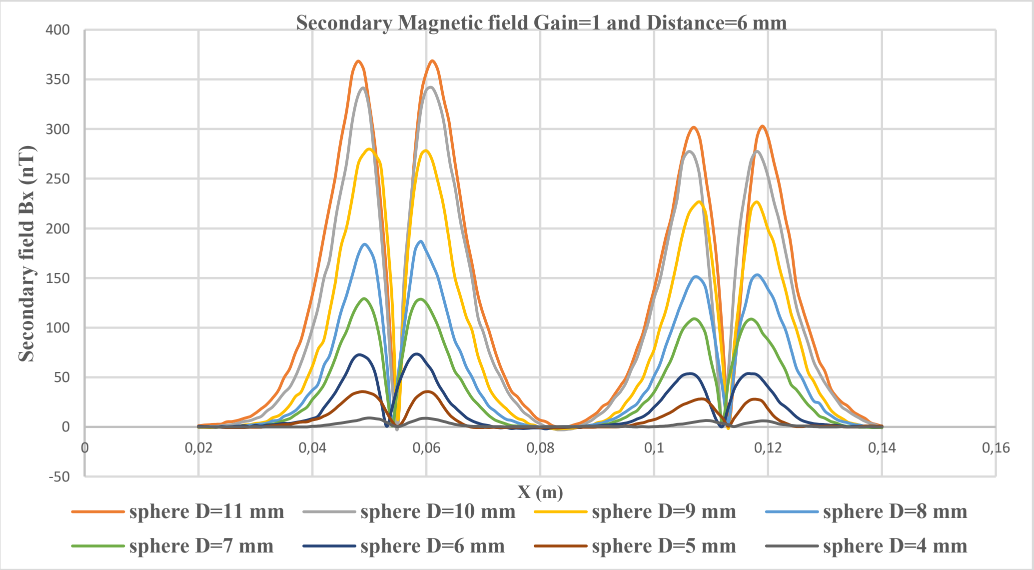

Figure 37 - $\boldsymbol{B_x}$curves for spheres with gain 1 and distance 6 mm.

The amplitude differences observed between the peaks can be explained by the variations in sensitivity and the different gains applied in the measurement system. Although the coils and experimental conditions are symmetrical, the sensor response may exhibit small magnitude variations due to its intrinsic sensitivity and the gain setting used during each measurement.

Table 5 presents the data obtained for the same set of spheres, but with a distance of 9 mm, also under a gain of 1 V/V. The peak values decrease significantly compared to the 6 mm distance, highlighting the dependence of amplitude on the distance between the sphere and the sensors.

Table 5 – Peak amplitudes of the secondary magnetic field for a gain of 1 V/V and 9 mm distance, considering same set of lead spheres, but with diameters from 5 mm to 11 mm.

Diameter (mm)	Distance (mm)	Gain (V/V	Peak 1 (nT)	Peak 2 (nT)	Peak 3 (nT)	Peak 4 (nT)
11.0	9.0	1	89.44	90.23	81.18	80.72
10.0	9.0	1	71.53	72.27	58.18	58.29
9.0	9.0	1	64.21	64.83	50.54	49.89
8.0	9.0	1	55.24	55.92	42.23	41.92
7.0	9.0	1	29.64	29.87	21.38	21.41
6.0	9.0	1	19.40	19.18	15.30	15.13
5.0	9.0	1	8.68	8.71	6.28	6.17

Figure 38 shows the behaviour of the secondary magnetic field with a gain of 1 and a distance of 9 mm. Compared to Figure 30, a general decrease in the peak amplitudes can be observed, as expected, due to the increased distance between the object and the sensors.

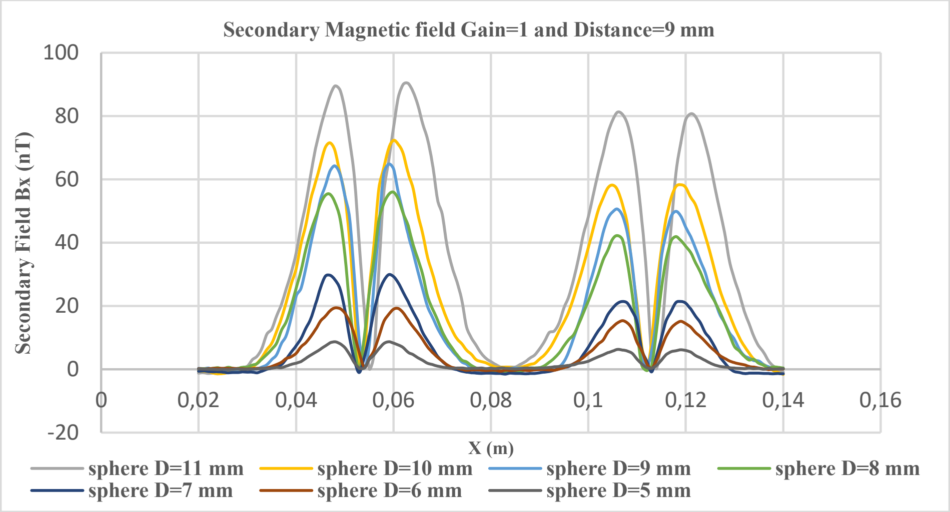

Figure 38 - B_x curves for spheres with diameters from 5 mm to 11 mm, with a gain of 1 and 9 mm distance.

5.6.2
Results with gain of 10 V/V

Tables 6 and 7 present the measured peaks for a gain of 10 V/V, with distances of 6 mm and 9 mm, respectively. The increased gain enables the detection of weaker signals from lower-diameter spheres, specifically 3 mm for the 6 mm distance and 4 mm for the 9 mm distance, while preserving the symmetric pattern of the detected peaks.

Table 6 – Peak amplitudes of the secondary magnetic field for a gain of 10 V/V and 6 mm distance, with sphere diameters ranging from 3 mm to 6 mm.

Diameter (mm)	Distance (mm)	Gain (V/V)	Peak 1 (nT)	Peak 2 (nT)	Peak 3 (nT)	Peak 4 (nT)
6.0	6.0	10	81.82	81.86	72.39	72.20
5.0	6.0	10	37.59	37.69	29.42	29.32
4.0	6.0	10	14.28	14.18	12.41	12.32
3.0	6.0	10	5.45	5.45	3.30	3.20

Table 7 – Peak amplitudes of the secondary magnetic field for a gain of 10 V/V and 9 mm distance, with sphere diameters ranging from 4 mm to 11 mm.

Diameter (mm)	Distance (mm)	Gain (V/V)	Peak 1 (nT)	Peak 2 (nT)	Peak 3 (nT)	Peak4 (nT)
11.0	9.0	10	102.67	103.04	90.24	90.10
10.0	9.0	10	83.91	83.91	67.98	68.76
9.0	9.0	10	69.82	70.11	57.43	57.18
8.0	9.0	10	61.03	60.94	47.27	47.30
7.0	9.0	10	38.70	38.67	30.65	30.51
6.0	9.0	10	24.42	24.38	21.05	21.12
5.0	9.0	10	9.22	9.18	7.68	7.58
4.0	9.0	10	3.72	3.76	2.96	2.98

Figures 39 and 40 illustrates the results obtained with a gain of 10 V/V for distances of 6 mm and 9 mm, respectively. The increasing trend with the sphere diameter remains evident, although with less pronounced variations at greater distances.

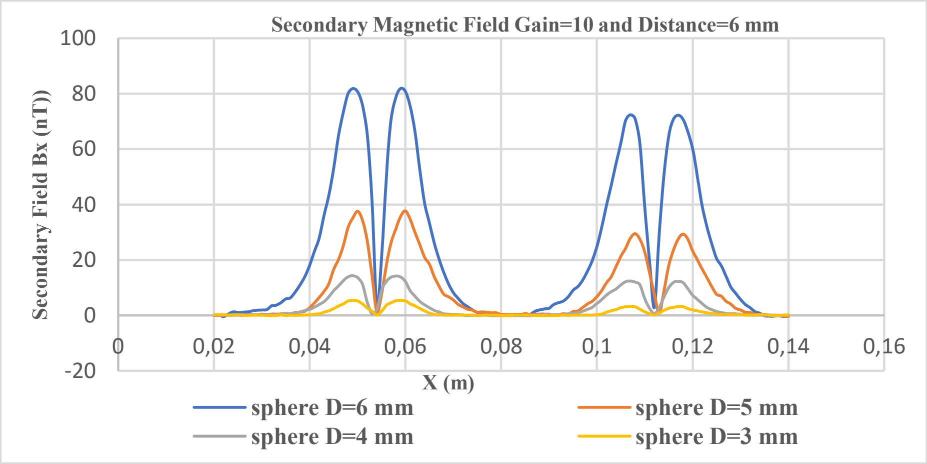

Figure 39 - B_x *curves for spheres with a gain of 10, for spheres with diameters from 3 mm to 6 mm and a distance of 6 mm.*

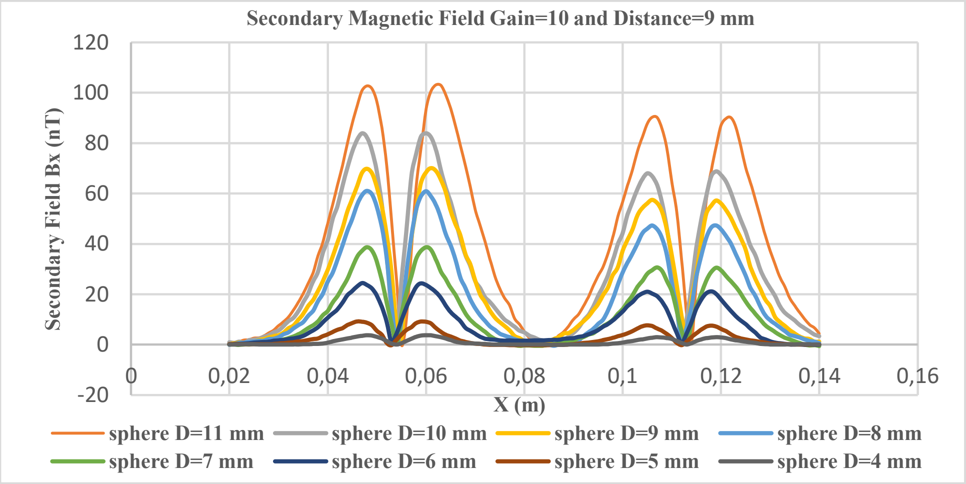

Figure 40 - B_x curves for spheres with a gain of 10, for spheres with diameters from 5 mm to 11 mm and a distance of 9 mm.

5.6.3
Results with gain of 20 V/V

Table 8 presents the data obtained with a gain of 20 V/V and a distance of 6 mm, used especially for spheres with smaller diameters, ranging from 3 mm to 6 mm. The distance amplification allowed for clear detection of signals even for 3 mm spheres.

Table 8 – *Peak amplitudes of the secondary magnetic field for a gain of 20 and a 6 mm distance.*

Diameter (mm)	Distance (mm)	Gain (V/V)	Peak 1 (nT)	Peak 2 (nT)	Peak 3 (nT)	Peak 4 (nT)
6.0	6.0	20	83.61	83.70	76.79	76.82
5.0	6.0	20	38.12	38.16	33.33	33.33
4.0	6.0	20	17.53	17.56	15.27	15.18
3.0	6.0	20	5.88	5.88	4.27	4.25

Figure 41 shows the experimental data for a gain of 20 and a distance of 6 mm, mainly applied to small spheres, from 3 mm to 6 mm in diameter. Despite the low absolute intensity of the peaks, the amplification makes it possible to observe the typical shape of four symmetric peaks clearly

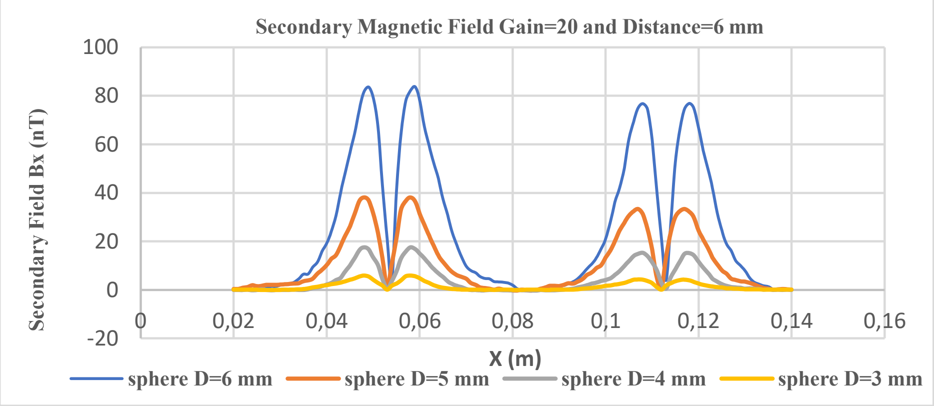

Figure 41- B_x curves for spheres with diameters from 3 mm to 6 mm, with a gain of 20 and 6 mm distance.

Finally, Table 9 summarises the smallest detectable sphere diameter for each distance and gain analysed. At 6 mm distance, spheres as small as 3 mm were detected with gains of 10 and 20 V/V, and 4 mm with a gain of 1 V/V. At 9 mm distance, the limit was the diameter of 5 mm with a gain of 1 V/V and 4 mm diameter with a gain of 10 V/V. These results confirm the significant influence of gain on system sensitivity and serve as a reference for the simulation comparison in the next section. According to these results. a gain of 10 V/V is the most efficient one for both studied distances.

Table 9 – *Smallest detectable diameter of metallic spheres according to sensor distance and amplification gain.*

Distance (mm)	Diameter (mm) for Gain = 1 V/V	Diameter (mm) for Gain = 10	Diameter (mm) for Gain = 20
6.0	4.0	3.0	3.0
9.0	5.0	4.0	-

5.6.4
Comparison of Experimental Results with Simulation

This section presents a comparative analysis between the experimental results obtained with the metallic body detection system and the results from previously conducted computational simulations. Three series of tests were carried out, varying the diameter of the foreign body, the distance at which it was located and the gain of the measurement system, in order to assess the accuracy and reliability of the proposed method.

To facilitate the visualisation and analysis of the results, the data were organised according to the gain of the measurement system:

5.6.4.1
Gain of 1 V/V

Tests were conducted for distances of 6 mm and 9 mm, with the following diameters:

- Distance = 6 mm: diameters from 11 mm to 4 mm (Figure 42).
- Distance = 9 mm: diameters from 11 mm to 5 mm (Figure 43).

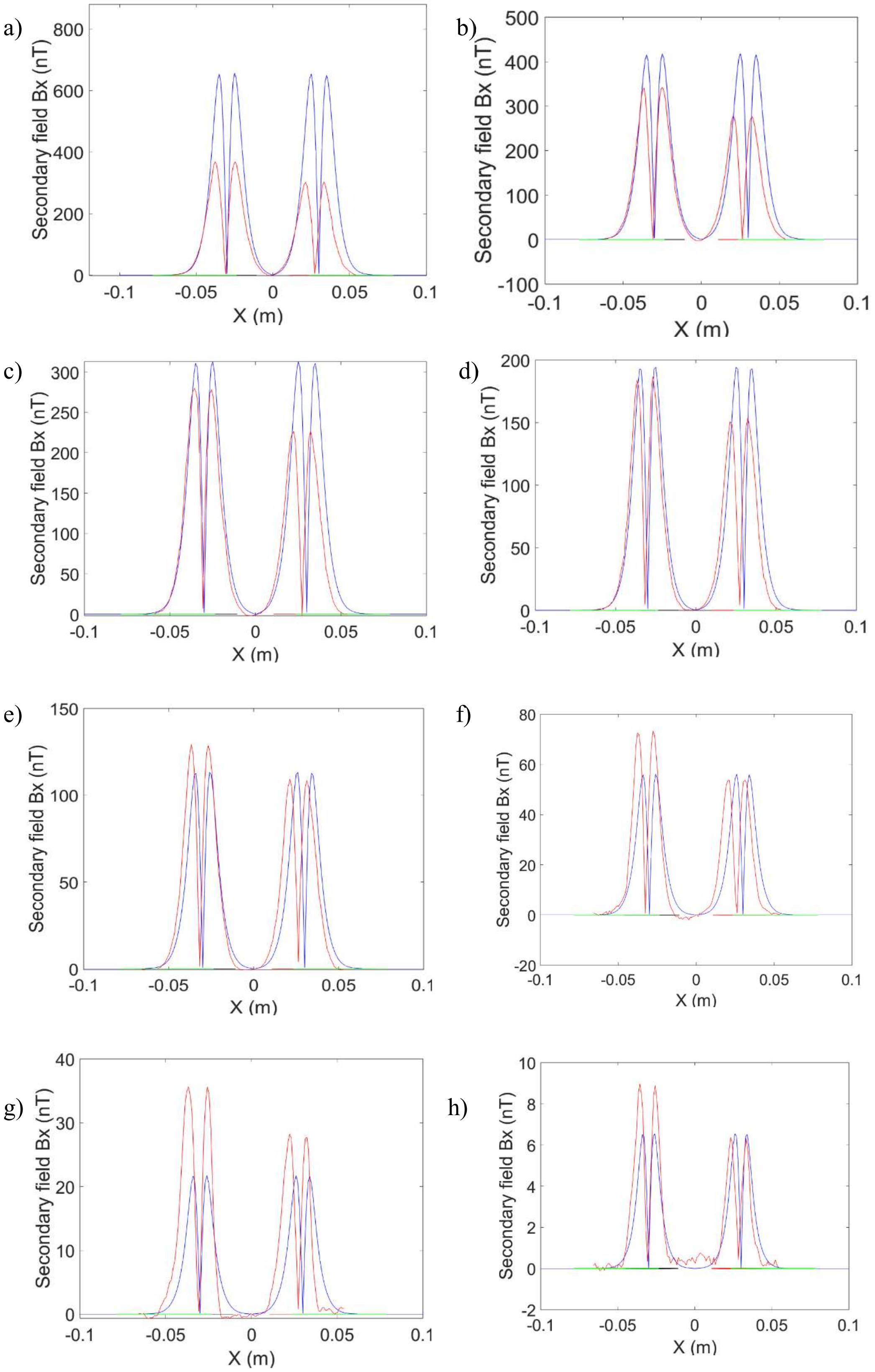

Figure 42 - Experimental data (red) and simulation (blue) of the secondary magnetic field in the region of the foreign body location, for metallic spheres placed at a

distance of 6 mm, with gain 1 V/V. Sphere diameters: (a) 11 mm; (b) 10 mm; (c) 9 mm; (d) 8 mm; (e) 7 mm; (f) 6 mm; (g) 5 mm; (h) 4 mm.

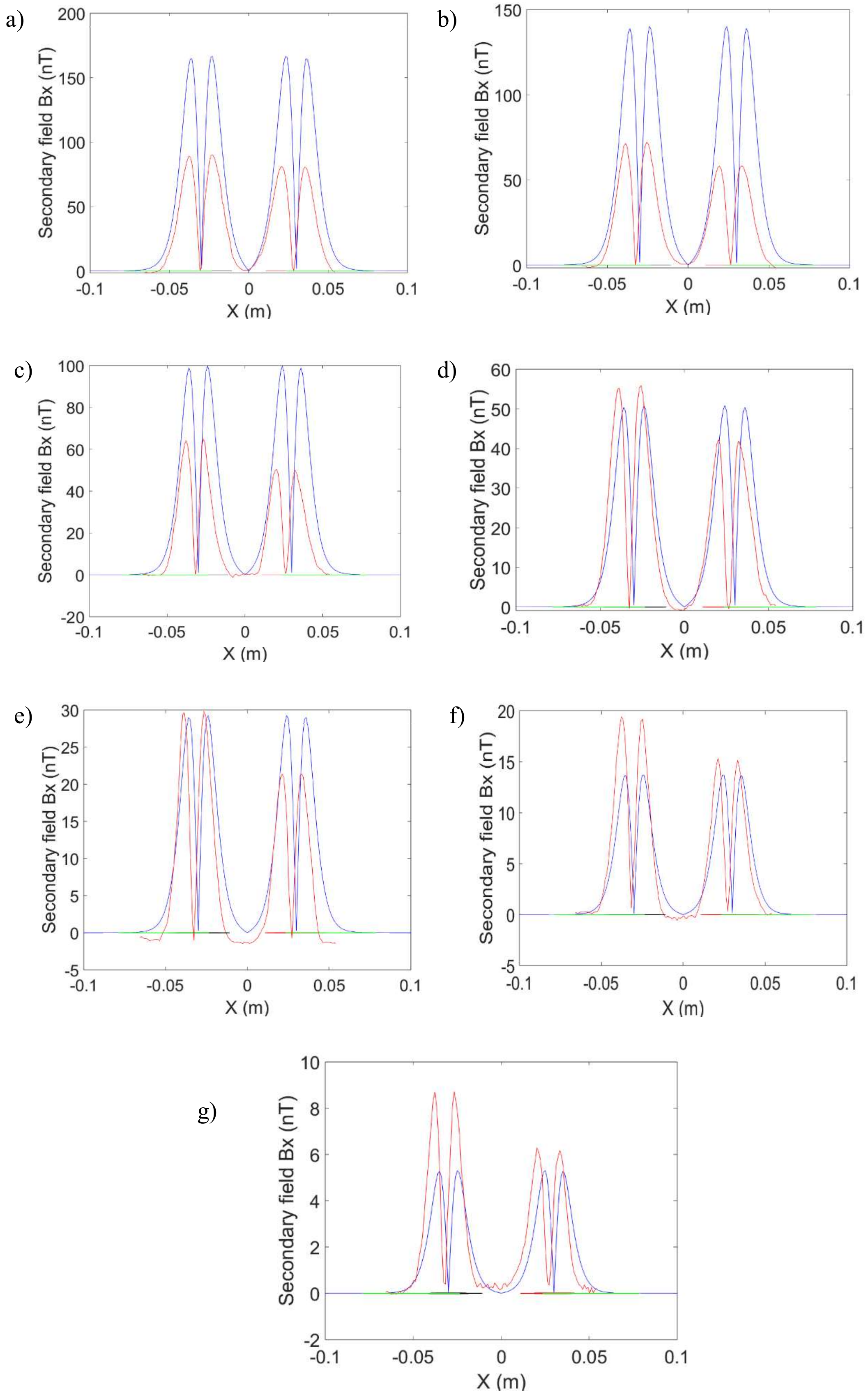

Figure 43 - Experimental data (red) and simulation (blue) of the secondary magnetic field in the region of the foreign body location, for metallic spheres placed at a distance

of 9 mm, with gain 1 V/V. Sphere diameters: (a) 11 mm; (b) 10 mm; (c) 9 mm; (d) 8 mm; (e) 7 mm; (f) 6 mm; (g) 5 mm.

5.6.4.2

Gain of 10 V/V

- Distance = 6 mm: diameters from 6 mm to 3 mm (Figure 44).
- Distance= 9 mm: diameters from 11 mm to 5 mm (Figure 45).

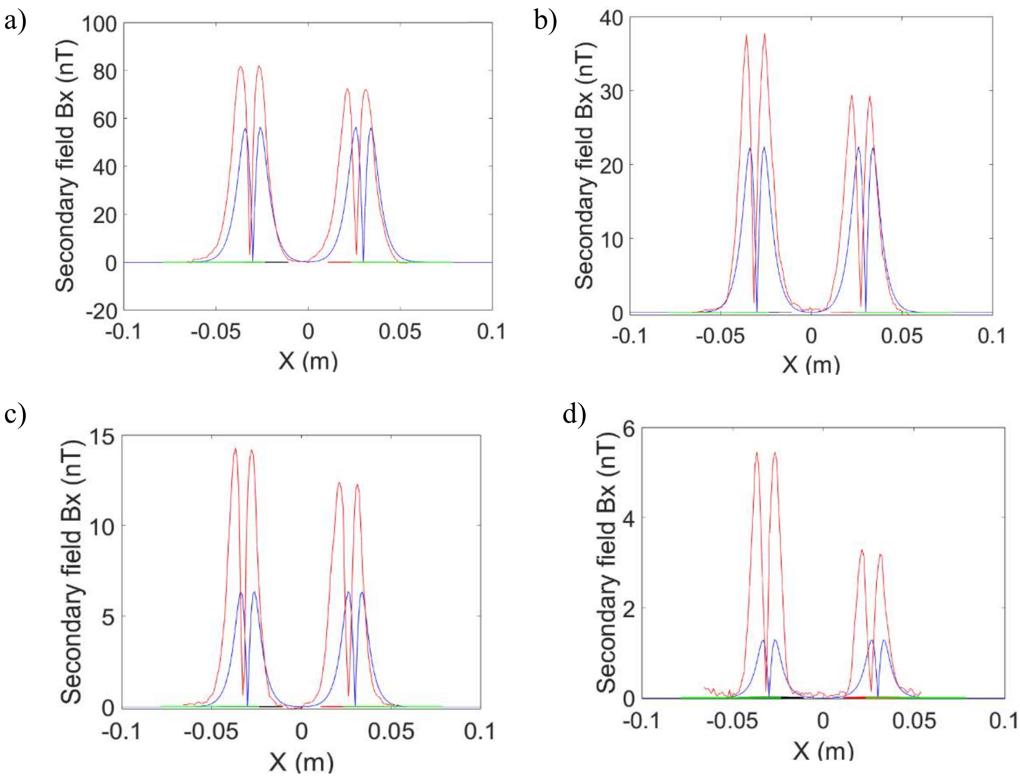

Figure 44 - Experimental data (red) and simulation (blue) of the secondary magnetic field in the region of the foreign body location, for metallic spheres placed at a distance of 6 mm, with gain 10 V/V. Sphere diameters: (a) 6 mm; (b) 5 mm; (c) 4 mm; (d) 3 mm.

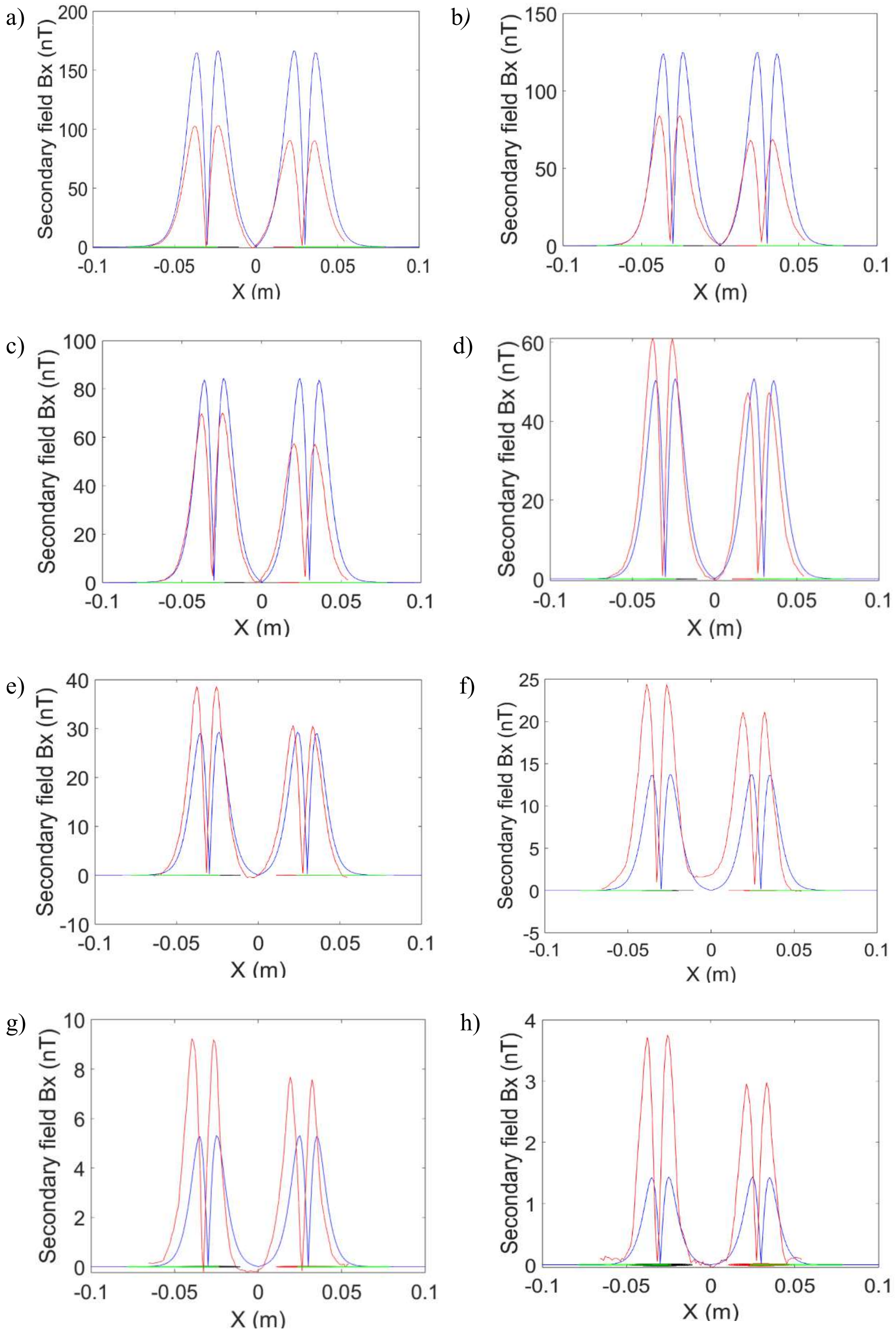

Figure 45 - Experimental data (red) and simulation (blue) of the secondary magnetic field in the region of the foreign body location, for metallic spheres placed at a distance of 9 mm, with gain 10 V/V. Sphere diameters: (a) 11 mm; (b) 10 mm; (c) 9 mm; (d) 8 mm; (e) 7 mm; (f) 6 mm; (g) 5 mm: (h)4 mm.

5.6.4.3

Gain of 20 V/V

- Distance = 6 mm: diameters from 6 mm to 3 mm (Figure 46).

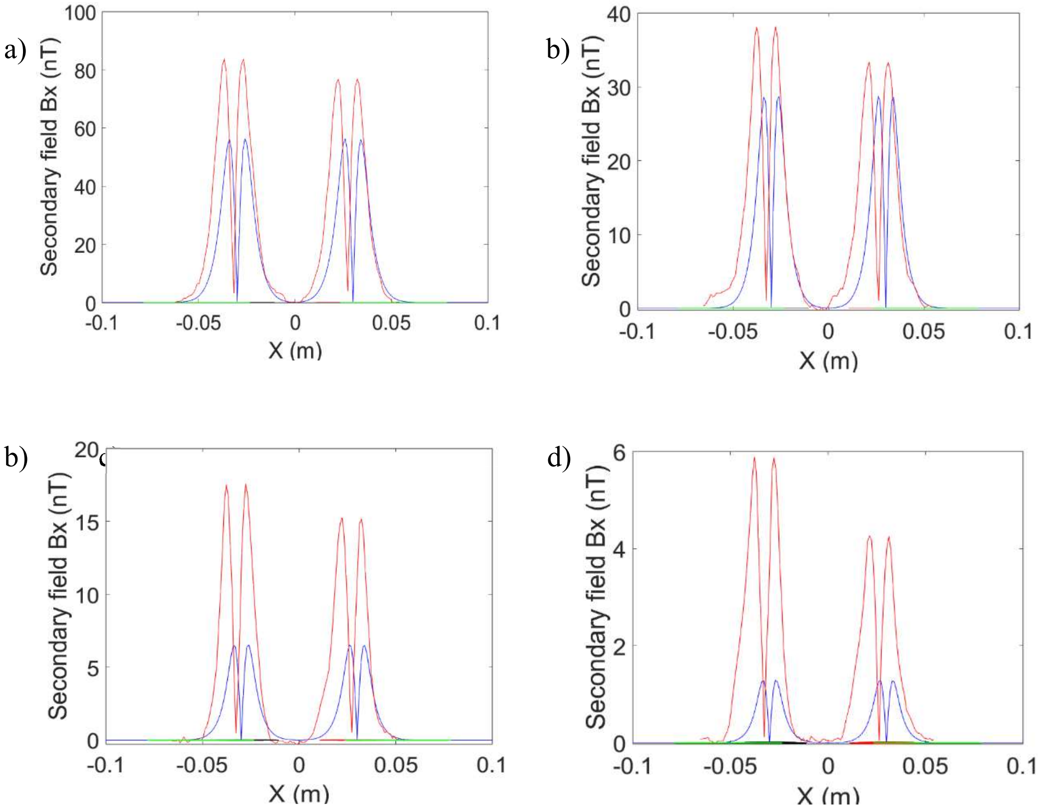

Figure 46 - *Experimental data (red) and simulation (blue) of the secondary magnetic field in the region of the foreign body location, for metallic spheres placed at a distance of 6 mm, with gain 20 V/V. Sphere diameters: (a) 6 mm; (b) 5 mm; (c) 4 mm; (d) 3 mm.*

The comparison between the experimental (red) and simulated (blue) curves shows that both present a similar overall pattern, with two main peaks corresponding to the regions of maximum coupling between the excitation coils and the induced magnetic response of the metallic sphere. Nevertheless, slight discrepancies are observed in the amplitude and width of the peaks, which are generally higher and narrower in the experimental results.

These differences may be attributed to factors not fully represented in the numerical model, such as sensor nonlinearities, coil geometry, or small misalignments during measurements. Another possible source of deviation lies in the intrinsic inhomogeneity of the commercial GMI sensors employed, which may exhibit slightly different sensitivities within the gradiometric configuration.

Additional variations may also arise from electronic noise and gain fluctuations in the amplification stage.

Overall, the simulation serves as a proof of concept, confirming that, in principle, the detection of the secondary magnetic field produced by a non-ferromagnetic metallic sphere is feasible under the proposed configuration. The experimental measurements, in turn, validate this theoretical prediction under real operating conditions, highlighting the influence of physical and electronic factors inherent to the practical setup.

5.7
Inverse Modelling Using Artificial Neural Networks

This section presents the inverse modelling of the secondary magnetic field using an artificial neural network of the MLP (Multilayer Perceptron) type, with the objective of simultaneously estimating the distance and diameter of non-ferromagnetic metallic spheres from features extracted from measured signals. The approach aims to overcome the limitations of traditional analytical methods by leveraging the neural network's ability to model nonlinear relationships between the experimental data and the physical parameters of the non-ferromagnetic metallic spheres.

5.7.1
Data and Pre-processing

The data used were extracted from a spreadsheet containing previously processed magnetic signals, generated by the passage of metallic spheres through magnetic sensors. The pre-processing stage involved extracting relevant features from these signals, focusing on the peak values of the secondary magnetic field generated by the spheres.

The input variables used in the neural network model include:

- **Heights of the four magnetic peaks:**
  - peak1, peak2, peak3, peak4 → correspond to the maximum values of the secondary magnetic field detected in the signals.

- **Corresponding positions of the peaks:**
  - pos1, pos2, pos3, pos4 → indicate the positions of the respective maximum peaks along the scanning path over the sensors.

- **Derived combinations of the previous variables:**
  - peak1_peak4 = peak1 - peak4
  - peak2_peak3 = peak2 - peak3
  - pos1_pos4 = pos1 - pos4
  - pos2_pos3 = pos2 - pos3

These combinations were included to capture differential relationships between the peaks and their positions, which proved useful for estimating the physical characteristics of the spheres (such as distance and diameter) in a more robust manner. These 12 variables were selected for their correlation with the target parameters.

5.7.2
Network Architecture

The neural network architecture implemented corresponds to a Multilayer Perceptron (MLP), with the following specifications:

- **Input layer:** 12 neurons, corresponding to the extracted features and their combinations.

- **Hidden layers:**
  - First layer: 16 neurons
  - Second layer: 8 neurons

Both layers use the ReLU (Rectified Linear Unit) activation function, which introduces non-linearity into the model, allowing the network to learn complex relationships between inputs and outputs. During training, a 30 % dropout is applied to the hidden layers, randomly deactivating 30 % of the neurons at each epoch to reduce the risk of overfitting.

- **Output layer:** 2 neurons, corresponding to the target variables: the distance and diameter of the sphere.

5.7.3
Training

The training process was conducted using the experimental dataset, as described in Section 5.7.1. The dataset consisted of 34 measurements, each representing the peak values of the secondary magnetic field generated by a non-ferromagnetic metallic sphere at a certain position relative to the sensor.

The training process was conducted by splitting the dataset into 80 % for training and 20 % for validation, with all variables previously normalised. The network was trained using the Adam optimiser, with a learning rate of 0.001, a batch size of 8, and the Mean Squared Error (MSE) loss function.

To prevent overfitting, the early stopping technique was applied, which automatically halts training when the validation loss fails to improve after 130 consecutive epochs. The maximum number of epochs was set to 900, although in most executions the network converged before reaching this limit.

Figure 47 shows the loss curve during training. It can be observed that the model achieved stable convergence, with a progressive reduction in validation loss and no signs of overfitting.

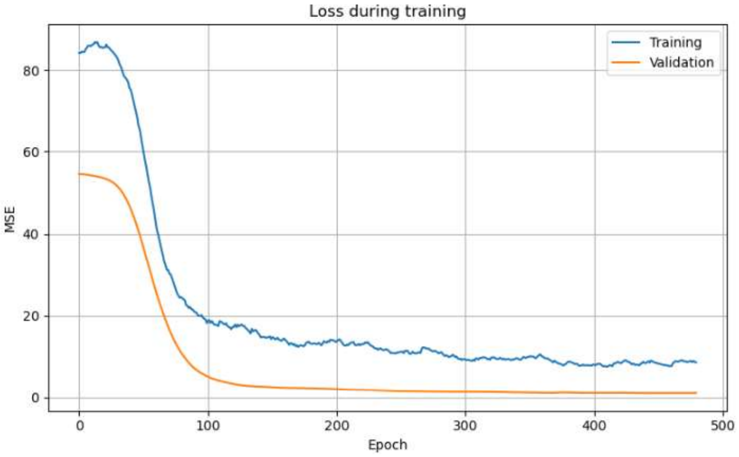

Figure 47 - Loss During Training

Although the experimental dataset consisted of only 34 samples, the neural network was implemented as a proof of concept to evaluate the feasibility of the inverse modelling approach. To mitigate overfitting, dropout regularisation and early stopping were employed, ensuring convergence despite the limited dataset size.

5.7.4
Evaluation

After training, the model was evaluated using the validation set (20 % of the data), ensuring an unbiased assessment of its generalisation capability. The following metrics were used to quantify the prediction errors:

- RMSE (Root Mean Squared Error)

$$\mathrm{RMSE} = \sqrt{\frac{1}{\mathrm{N}} \sum_{j=1}^{\mathrm{N}} \left(P_j - T_j\right)^2} \tag{59}$$

- MAPE (Mean Absolute Percentage Error)

$$\mathrm{MAPE} = \frac{1}{\mathrm{N}} \sum_{j=1}^{\mathrm{N}} \left| \frac{P_j - T_j}{T_j} \right| \tag{60}$$

where P_j is the value predicted by the network for sample j in the test set, Tj is the corresponding experimental (target) value, and N is the number of test samples.

The results obtained were:

- RMSE for Distance: 1.013 mm
- RMSE for Diameter: 1.064 mm
- MAPE for Distance: 10.83 %
- MAPE for Diameter: 16.47 %

Figures 48 and 49 show scatter plots comparing the measured and predicted values for distance and diameter, respectively. The dashed red line represents the ideal line, where predictions would exactly match the measured values. The proximity of the data points to this line demonstrates the good performance of the model.

These results correspond to the validation set (20 % of the data), which was not used during training, thus reflecting the model's generalisation capability when predicting unseen experimental samples.

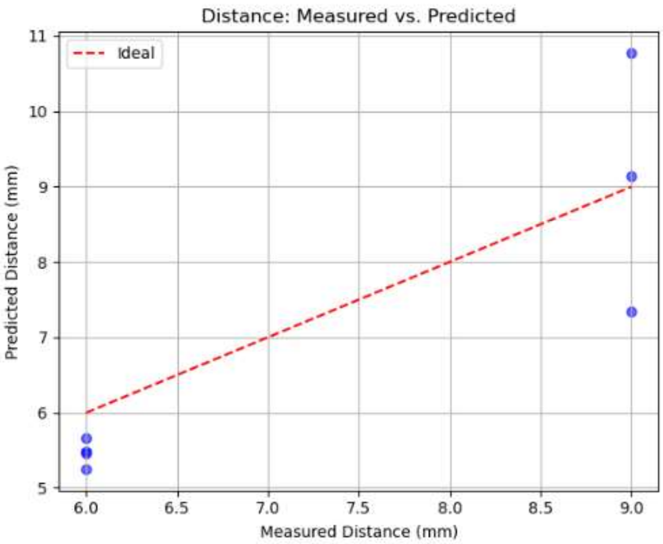

Figure 48 - Distance: Measured vs. Predicted

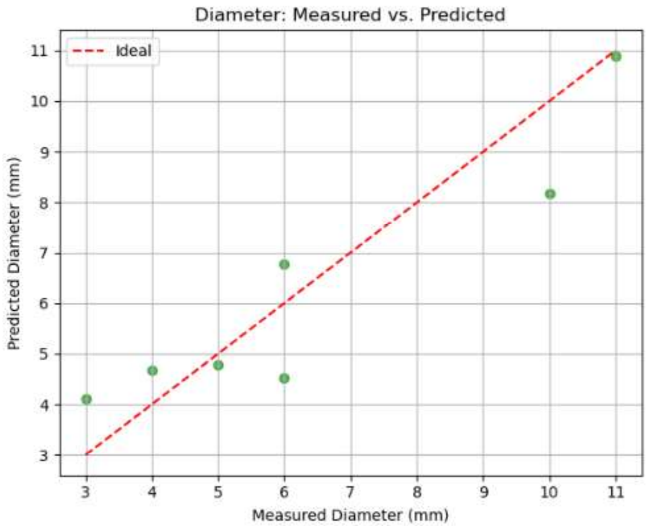

Figure 49 - Diameter: Measured vs. Predicted

Table 10 presents the measured and predicted values for the distance and diameter of the metallic spheres, considering samples with an experimental distance of 6 mm. In addition to the predictions provided by the model, the corresponding absolute errors for each parameter are shown. It can be observed that, for most samples, the absolute error in distance remains below 0.3 mm, while for diameter, the errors are generally less than 1 mm. These results indicate that the model exhibits good performance in estimating both variables, even under specific experimental conditions.

Table 10 – Comparison between measured and predicted values for distance = 6 mm.

Measured distance (mm)	Measured Diameter (mm)	Predicted distance (mm)	Predicted Diameter (mm)	Absolute error Distance (mm)	Absolute error diameter (mm)
6.0	11.0	6.50	8.92	0.51	2.08
6.0	10.0	5.98	7.61	0.02	2.39
6.0	9.0	6.93	9.42	0.93	0.42
6.0	8.0	5.46	6.38	0.53	1.62
6.0	7.0	5.29	5.76	0.70	1.24
6.0	6.0	5.95	5.52	0.05	0.48
6.0	5.0	5.54	4.78	0.46	0.22
6.0	4.0	5.29	4.71	0.71	0.71
6.0	3.0	5.45	4.11	0.55	1.11

Table 11 presents the measured and predicted values for the distance and diameter of the metallic spheres, considering samples with an experimental distance of 9 mm. Differently from what was observed in Table 10, the absolute errors here are more significant, especially in the distance prediction, which in some samples exceeds 1 mm. The error in diameter also varies more significantly, reaching up to 2.2 mm. These results indicate lower accuracy of the model for this specific condition, which may be related to greater signal attenuation at higher elevations or to the limitations of the training data for this range. Still, the model maintains a reasonable generalisation capability, with acceptable errors in several samples.

Table 11 – Comparison between measured and predicted values for distance = 9 mm.

Measured distance (mm)	Measured Diameter (mm)	Predicted distance (mm)	Predicted Diameter (mm)	Absolute error Distance (mm)	Absolute error diameter (mm)
9.0	11.0	8.97	10.38	0.03	0.62
9.0	10.0	8.39	8.2	0.61	1.8
9.0	9.0	6.56	6.00	2.44	3.0
9.0	8.0	7.10	6.54	1.9	1.46
9.0	7.0	7.37	6.13	1.63	0.87
9.0	6.0	7.34	6.77	1.66	0.77
9.0	5.0	7.74	6.35	1.26	1.35
9.0	4.0	7.42	6.21	1.58	2.21

Therefore, the results obtained demonstrate that inverse modelling with MLP neural networks is a reliable and effective approach for estimating the physical characteristics of non-ferromagnetic metallic bodies from magnetic signals, showing low average error even under different experimental conditions.

Still, the model maintains a reasonable generalisation capability, with acceptable errors in several samples. Although the dataset contained slightly more measurements for the 6 mm spheres, the use of normalised data helped minimise bias toward specific diameters.

6
Discussion

This chapter presents a critical and integrated analysis of the results obtained throughout the study, covering both simulated and experimental data. The discussion is organised into three main parts: (i) primary magnetic field, (ii) secondary magnetic field (experimental and simulated), and (iii) application of artificial neural networks in inverse modelling.

6.1
Primary Magnetic Field

The comparative analysis between the experimental and simulated results of the primary magnetic field showed excellent agreement. The simulation of the primary magnetic field presented in this work reproduced the results reported in [2] with high fidelity, showing the characteristic profile with two symmetric positive peaks and a central negative peak along the X-axis, which confirms that the theoretical model previously proposed remains valid under the current experimental configuration. Figure 33 highlights the correspondence between the magnetic flux density profiles obtained from simulation and practical tests.

The percentage error observed between the simulated (179 μT) and experimental (173 μT) maximum values was only 3.35 %, significantly lower than the acceptable limit of 5 % for experimental validations in the field of magnetic instrumentation.

Compared to the system described by [5], in which the primary field is generated by a long solenoid with an amplitude limited to 1 μT, a value close to the saturation limit of GMI sensors, the system proposed here with planar coils allowed for the generation of more intense fields, without compromising the linear operation of the sensor. This represents a significant improvement in excitation capacity, without penalising the measurement.

This result reinforces the reliability of the computational modelling and experimental methodology used to generate and measure the primary field.

6.2
Secondary Magnetic Field

It was observed that the overall shapes of the simulated and experimental curves were similar, presenting the four characteristic peaks expected from the model. However, amplitude differences were noted depending on the sphere diameter:

- For larger diameter spheres, the simulated values were higher than the experimental ones.
- For intermediate diameters, there was good agreement between simulation and experiment.
- For smaller spheres, the experimental peaks exceeded the simulated ones.

This trend was similarly observed across different gain levels (1, 10, and 20) and for both measurement distances (6 mm and 9 mm), indicating that the model responds consistently, but with deviations related to the size of the sphere.

Previous techniques, such as the SQUID-based method described in [1], also aimed to map the secondary magnetic field generated by metallic objects, achieving highly accurate results. However, such systems require cryogenic operation and are costly, which limits their widespread clinical application. The system proposed in this study, operating at room temperature and employing lower-cost GMI sensors, represents a viable alternative albeit with slightly lower sensitivity compared to SQUID-based devices.

Previous works, such as those in [3,5], employed GMI sensors in a differential configuration placed along a solenoid, but the excitation field was limited to ±1 μT due to the sensor's linear operating range. This restriction also reduced the intensity of the detected secondary field, especially in the case of small or deeply positioned spheres. In the system proposed here, the physical separation between the excitation and measurement stages allowed for an increase in the secondary field intensity without compromising sensor operation, resulting in improved detection sensitivity.

The study conducted in [2] resented the design and computational validation of an innovative measurement system aimed at locating non-ferromagnetic metallic foreign bodies in the human body. The proposed system was based on the generation of eddy currents and subsequent mapping of the secondary magnetic field using a horizontally positioned GMI sensor. Additionally, it incorporated spiral planar coils with opposing windings, specially designed to maximise sensitivity and detection accuracy. Although the approach demonstrated excellent theoretical and computational performance [2], experimental tests revealed a significant limitation: in all evaluated positions, it was not possible to null the measured magnetic field even when the sensor was strategically positioned between the coils and aligned along the X-axis as predicted by the model. Due to this practical limitation, the strategy proposed in [3,5] was adopted, which involves the use of a time-varying primary magnetic flux density generator, with the secondary field measured by a differential gradiometric system composed of two GMI sensors. In our research, planar coils were retained for generating the primary magnetic field, and a gradiometer was employed to measure the secondary magnetic field. This approach yielded improved results compared to previous tests, indicating greater accuracy and reliability in the measurements.

Furthermore, it was identified that the electrical conductivity used in the simulations significantly influences the results. Initially, a value of $\sigma = 4{,}55 \times 10^{6}$ S/m was used, corresponding to the conductivity of pure lead. However, after empirically reducing this value, a better agreement was observed between the simulated and experimental data, especially for intermediate sphere diameters. This suggests that the spheres used may contain impurities or structural imperfections that reduce their effective conductivity, which reinforces the importance of accurately characterising the materials to build more realistic computational models.

6.3 Discussion of Detection Performance

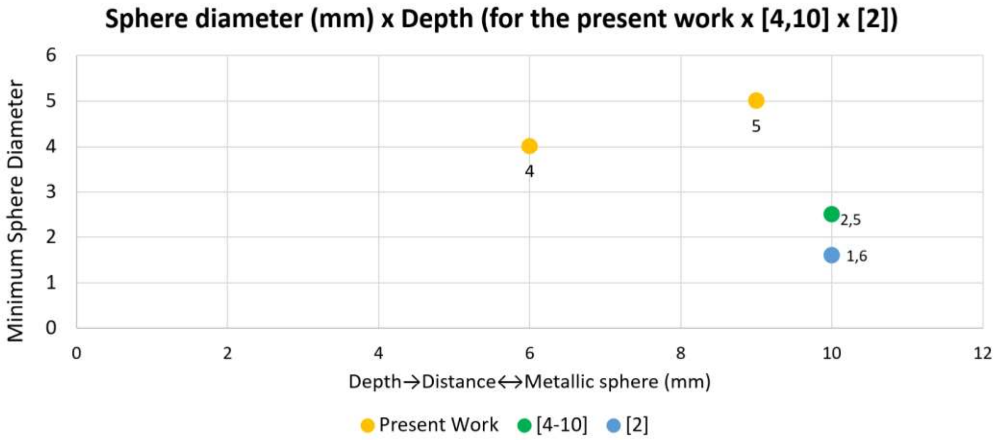

Figure 50 - Comparison of minimum detectable sphere diameter as a function of depth between the present work and previous studies

Figure 50 compares the minimum detectable sphere diameter as a function of depth between the present work and previous studies [2] and [4–10]. The results show that the system developed here was able to detect metallic spheres with diameters of 4–5 mm at depths of 6 and 9 mm, whereas previous studies achieved smaller diameters (1.6–2.5 mm) but only at shallower depths.

The differences observed in the minimum detectable sphere diameter between this work and the results reported in [2] and [4–10] may be attributed to several experimental and geometric factors.

Firstly, the planar gradiometric configuration employed in this study may not represent the optimal sensitivity condition for deeper measurements. In such an arrangement, the horizontal component of the magnetic field decreases more rapidly with depth, which can reduce the coupling between the induced secondary field and the GMI sensors. In contrast, an axial configuration could provide stronger field coupling, since the sensors would be aligned with the dominant magnetic component (Bz).

Furthermore, slight differences in the sensitivity or calibration of the two GMI sensors may have introduced asymmetries in the differential response, limiting the system’s ability to fully cancel the primary field. In addition, any small misalignment between the sensitive axes of the sensors could further weaken the differential signal.

Another relevant aspect is that the configuration in [2] employed a single GMI sensor, avoiding inter-sensor balancing and alignment issues, which may explain its higher sensitivity at shallower depths. Finally, possible metallic impurities in the experimental support could have induced parasitic eddy currents, slightly distorting the magnetic field and affecting the detection accuracy.

Despite these limitations, the system developed in this work successfully detected metallic spheres at depths of 6–9 mm, demonstrating the feasibility of the proposed approach under realistic experimental conditions.

6.4
Inverse Modelling with Neural Networks

The inverse modelling approach using MLP neural networks proved effective in simultaneously estimating the distance and diameter of the metallic spheres. To select the final model configuration, different combinations of input variables were evaluated. Initially, the network was trained using only the four maximum peaks of the secondary field along with their gain values, which resulted in relatively high error. Later, the peaks were normalised by their gain (peak / gain) and additional information about peak positions and derived combinations of peaks and positions was included. This final configuration allowed the model to better capture the signal features, significantly improving the accuracy in estimating sphere height and diameter, demonstrating the robustness of the proposed solution. Figures 53 and 54 demonstrate the network’s ability to generalise from the training data, showing good proximity between the predicted and measured values.

In Table 10, for samples with a distance of 6 mm, absolute distance errors were mostly below 0.3 mm, and diameter errors below 1 mm. In contrast, in Table 11, for samples with a distance of 9 mm, the errors were more significant, especially in distance prediction, exceeding 1 mm in some cases. This indicates that the model's accuracy decreases as the distance between the metallic object and the sensor increases a trend also observed in the magnetic field measurements.

While previous works such as [2,3,5] effectively addressed the generation of the secondary magnetic field, few authors have simultaneously applied neural networks to the inverse problem to estimate multiple physical parameters. Thus, the methodology proposed in this study stands out by integrating artificial neural network techniques with magnetic instrumentation, expanding the possibilities for inference even under conditions of signal noise and complexity.

The global evaluation metrics (RMSE and MAPE) confirm the trends observed in the results, showing that the model achieves good accuracy in estimating both distance and diameter.

Therefore, it can be concluded that the use of artificial neural networks represents a viable and accurate alternative for solving the inverse problem in magnetic detection systems, with potential for practical applications in environments with geometric and material variability.

7

Conclusions and Future Work

In this dissertation, a detection system was proposed, developed, and validated for the localisation of non-ferromagnetic metallic bodies, based on eddy current excitation and gradiometric reading using GMI sensors. The main objective was to overcome the limitations identified in previous approaches, such as the interference of the primary magnetic field with the GMI sensor, the low portability of SQUID-based systems, and the difficulty in detecting small projectiles located at greater depths.

The system developed here integrates two fundamental concepts previously investigated separately in the literature: the use of spiral planar coils with opposing windings for generating the primary magnetic field [2], and the application of a differential gradiometric configuration with two GMI sensors for reading the secondary magnetic field [3]. This combination not only allowed for increased excitation intensity without saturating the sensor but also significantly improved measurement sensitivity, as evidenced by the experimental results.

Measurements demonstrated that the system is capable of detecting metallic spheres with diameters of just a few millimetres at depths of 6 mm and 9 mm, while remaining within the exposure limits defined by the ICNIRP. The computational modelling of the primary magnetic field showed excellent agreement with experimental data, validating the theoretical approach adopted.

In the case of the secondary magnetic field, the experimental results confirmed the behaviour predicted by the simulation, with a clear presence of the four characteristic peaks defined by the model. The comparison between simulation and experiment showed good agreement for intermediate-sized spheres, and amplitude deviations in cases involving large or small spheres, which can be attributed to factors such as the material's effective conductivity and the limitations of the simplified model.

Beyond solving the direct problem, this research also addressed the inverse problem, proposing a methodology based on MLP-type artificial neural networks to simultaneously estimate the distance (depth) and diameter of metallic spheres from features extracted from the measured signals. The developed neural model demonstrated promising performance, with low mean errors, particularly at smaller depths, and good generalisation capability.

Therefore, the results obtained indicate that the developed system is a viable, safe, low-cost, and non-invasive solution for localising non-ferromagnetic metallic bodies, with potential for real clinical applications. The use of accessible technologies, operation at room temperature, and the possibility of integration with intelligent algorithms make this system a promising alternative to conventional methods based on ionising radiation.

Several directions for future research can be pursued to enhance the system even further and extend its applicability:

Although the proposed system successfully demonstrated the feasibility of detecting non-ferromagnetic metallic bodies, some asymmetries were observed in the experimental signals. A possible explanation for these differences may be related to the inhomogeneity of the sensitivity of the commercial GMI sensors employed. In particular, higher amplitudes of peaks 1 and 2 were observed relative to peaks 3 and 4 in the experiments, which may indicate unequal sensor responses in the gradiometric configuration. Future work should investigate this hypothesis by exchanging the position of the sensing elements in the setup, or by performing detailed characterisation of each sensor individually. Additionally, future work should include characterisation measurements of the tuned filters associated with the readout circuit.

Another promising line of research involves refining the computational model. Currently, the model relies on simplified analytical approximations, which, despite their good agreement with experimental results, limit its ability to represent more complex geometries. The adoption of finite element modelling would allow a more accurate simulation of both the primary and secondary magnetic fields, thereby improving the predictive capability of the system.

Yet, particular attention should be given to the material properties of the detected objects. The effective electrical conductivity of the metallic spheres plays a crucial role in generating the secondary magnetic field. Accordingly, dedicated experiments to precisely determine the electrical conductivity of the bullets employed would provide valuable input for both experimental validation and modelling improvements.

Finally, as a broader perspective for future work, it is proposed to develop a pre-industrial prototype of the presented system, with the aim of enabling its use outside the laboratory environment. This stage would allow the validation of the device's performance under real detection conditions, assessing its robustness, portability, and potential for clinical applications focused on the localisation of non-ferromagnetic metallic bodies.

REFERENCES

[1] MONTEIRO, E. C. et al. Locating steel needles in the human body using a SQUID magnetometer. **Physics in Medicine and Biology**, v. 45, n. 8, p. 2389–2402, 1 ago. 2000.

[2] SEIXAS, V. T.; BARBOSA, C. R. H.; COSTA MONTEIRO, E. Design of a system for detection of non-ferromagnetic metallic foreign bodies based in eddy currents and GMI magnetometer. **Frontiers in Physics**, v. 12, p. 1330887, 6 maio 2024.

[3] FORTALEZA, L. G. S. et al. Biomedical comparison of magnetometers for non-ferromagnetic metallic foreign body detection. **Journal of Physics: Conference Series**, v. 1044, p. 012013, jun. 2018.

[4] COSTA MONTEIRO, E.; SUMMERS, R. Metrological requirements for biomedical device assessment and their ethical implications. **Measurement: Sensors**, v. 24, p. 100574, dez. 2022.

[5] GOUVEA E SILVA FORTALEZA, L. **NON-FERROMAGNETIC METALLIC FOREIGN BODY DETECTION BY EDDY CURRENTS**. MESTRE EM METROLOGIA—Rio de Janeiro, Brazil: PONTIFÍCIA UNIVERSIDADE CATÓLICA DO RIO DE JANEIRO, 28 set. 2016.

[6] BARBOSA, C. H. et al. Improvement of a technique for localization of steel needles in humans using a SQUID magnetometer. **IEEE Transactions on Appiled Superconductivity**, v. 11, n. 1, p. 677–680, mar. 2001.

[7] ANDRÄ, W. et al. Application of Magnetic Particles in Medicine and Biology. Em: KRONMÜLLER, H.; PARKIN, S. (Eds.). **Handbook of Magnetism and Advanced Magnetic Materials**. 1. ed. [s.l.] Wiley, 2007.

[8] POMPÉIA, F. et al. Ring shaped magnetic field transducer based on the GMI effect. **Measurement Science and Technology**, v. 19, n. 2, p. 025801, 1 fev. 2008.

[9] SILVA, E. C. D. et al. Sensitivity improvement of GMI magnetic and pressure transducers for biomedical measurements. **Revista Brasileira de Engenharia Biomédica**, v. 27, n. 2, p. 79–89, 2011.

[10] FORTALEZA, L. G. S. et al. Detecting non-magnetic metallic foreign bodies by GMR sensors through the use of eddy currents. 2015.

[11] BENAVIDES CABRERA, L. S.; COSTA DA SILVA, E.; MONTEIRO, E. C. Highly Sensitive Pressure Transducer for Measuring Arterial Pulse Wave Velocity Based on Giant Magneto-Impedance Sensors. **Sensors**, v. 25, n. 10, p. 3188, 19 maio 2025.

[12] BENAVIDES, L. S. et al. High sensitivity pressure transducer based on the phase characteristics of GMI magnetic sensors. **Measurement Science and Technology**, v. 29, n. 3, p. 035106, 1 mar. 2018.

[13] BENAVIDES, L. S.; COSTA DA SILVA, E.; COSTA MONTEIRO, E. Pressure transducer based on the phase characteristics of GMI effect for measuring the arterial pulse wave. **Journal of Physics: Conference Series**, v. 1065, p. 072039, ago. 2018.

[14] DIENSTKNECHT, T. et al. Indications for bullet removal: overview of the literature, and clinical practice guidelines for European trauma surgeons. **European Journal of Trauma and Emergency Surgery**, v. 38, n. 2, p. 89–93, abr. 2012.

[15] HALL BARBOSA, C. Localization of firearm projectiles in the human body using a superconducting quantum interference device magnetometer: A theoretical study. **Review of Scientific Instruments**, v. 75, n. 6, p. 2098–2106, 1 jun. 2004.

[16] RIPKA, P.; MIRZAEI, M.; MLEJNEK, P. Effect of external DC field on current transformers with amorphous and nanocrystalline cores. **Journal of Magnetism and Magnetic Materials**, v. 563, p. 170019, dez. 2022.

[17] **BIPM**. Disponível em: <https://www.bipm.org/en/>. Acesso em: 1 ago. 2025.

[18] **Le SI**. Disponível em: <https://www.bipm.org/en/measurement-units>. Acesso em: 1 ago. 2025.

[19] **International Organization of Legal Metrology — English**. Disponível em: <https://www.oiml.org/en>. Acesso em: 1 ago. 2025.

[20] **IEC homepage**. Disponível em: <https://www.iec.ch/homepage>. Acesso em: 1 ago. 2025.

[21] **ICNIRP | LF (1 Hz-100 kHz)**. Disponível em: <https://www.icnirp.org/en/frequencies/low-frequency/index.html>. Acesso em: 31 jul. 2025.

[22] **ISO - International Organization for Standardization**. Disponível em: <https://www.iso.org/home.html>. Acesso em: 1 ago. 2025.

[23] **World Health Organization (WHO)**. Disponível em: <https://www.who.int>. Acesso em: 1 ago. 2025.

[24] **Instituto Nacional de Metrologia Qualidade e Tecnologia**. Disponível em: <https://www.gov.br/inmetro/pt-br/copy_of_capa-inmetro>. Acesso em: 1 ago. 2025.

[25] EM 03/04/2024 16H29, P. EM 21/08/2020 11H24 A. **Eletricidade e Magnetismo**. Disponível em: <https://www.gov.br/inmetro/pt-br/assuntos/metrologia-cientifica/laboratorios/eletricidade-e-magnetismo>. Acesso em: 1 ago. 2025.

[26] **AnvisaLegis**. Disponível em: <https://anvisalegis.datalegis.net/action/ActionDatalegis.php?acao=apresentacao&cod_menu=9434&cod_modulo=310>. Acesso em: 1 ago. 2025.

[27] **Associação Brasileira de Normas Técnicas (ABNT)**. Disponível em: <https://abnt.org.br/>. Acesso em: 1 ago. 2025.

[28] **JCGM200-2012**. Disponível em: <https://www.bipm.org/en/doi/10.59161/jcgm200-2012>. Acesso em: 1 ago. 2025.

[29] ACCOMANDO, F.; FLORIO, G. Applicability of Small and Low-Cost Magnetic Sensors to Geophysical Exploration. **Sensors**, v. 24, n. 21, p. 7047, jan. 2024.

[30] MAHDI, A. E.; PANINA, L.; MAPPS, D. Some new horizons in magnetic sensing: high-Tc SQUIDs, GMR and GMI materials. **Sensors and Actuators A: Physical**, v. 105, n. 3, p. 271–285, ago. 2003.

[31] DE OLIVEIRA, B. R. C. et al. Automatic system for locating magnetic foreign bodies using GMI magnetometer. **Journal of Physics: Conference Series**, v. 1826, n. 1, p. 012085, 1 mar. 2021.

[32] MACHADO, F. L. A.; REZENDE, S. M. A theoretical model for the giant magnetoimpedance in ribbons of amorphous soft-ferromagnetic alloys. **Journal of Applied Physics**, v. 79, n. 8, p. 6558–6560, 15 abr. 1996.

[33] PANINA, L. V. Asymmetrical giant magneto-impedance (AGMI) in amorphous wires. **Journal of Magnetism and Magnetic Materials**, International Workshop on Magnetic Wires. v. 249, n. 1, p. 278–287, 1 ago. 2002.

[34] PHAN, M.-H. et al. Origin of asymmetrical magnetoimpedance in a Co-based amorphous microwire due to dc bias current. **Applied Physics Letters**, v. 83, n. 14, p. 2871–2873, 6 out. 2003.

[35] MAKHNOVSKIY, D. P.; PANINA, L. V.; MAPPS, D. J. Asymmetrical magnetoimpedance in as-cast CoFeSiB amorphous wires due to ac bias. **Applied Physics Letters**, v. 77, n. 1, p. 121–123, 3 jul. 2000.

[36] SILVA, E. C. et al. High sensitivity giant magnetoimpedance (GMI) magnetic transducer: magnitude versus phase sensing. **Measurement Science and Technology**, v. 22, n. 3, p. 035204, fev. 2011.

[37] PHAN, M.-H.; PENG, H.-X. Giant magnetoimpedance materials: Fundamentals and applications. **Progress in Materials Science**, v. 53, n. 2, p. 323–420, 1 fev. 2008.

[38] SILVA, E. C. et al. Magnetic field transducers based on the phase characteristics of GMI sensors and aimed at biomedical applications. Em: LIM, C. T.; GOH, J. C. H. (Eds.). **13th International Conference on Biomedical Engineering**. IFMBE Proceedings. Berlin, Heidelberg: Springer Berlin Heidelberg, 2009. v. 23p. 652–656.

[39] CESAR DE OLIVEIRA PITTA BOTELHO, A. **MODELO INTELIGENTE PARA OTIMIZAÇÃO DA SENSIBILIDADE DE AMOSTRAS GMI**. MESTRE EM ENGENHARIA ELÉTRICA—Rio de Janeiro, Brazil: PONTIFÍCIA UNIVERSIDADE CATÓLICA DO RIO DE JANEIRO, 15 abr. 2014.

[40] **Type DJ | Product Information | MI Sensors | Smart Company | Aichi Steel Corporation**. Disponível em: <https://www.aichi-steel.co.jp/ENGLISH/smart/mi/products/type-dj.html>. Acesso em: 31 jul. 2025.

[41] ANDRÄ, W.; NOWAK, H. (EDS.). **Magnetism in Medicine: A Handbook**. 1. ed. [s.l.] Wiley, 2006.

[42] SMYTHE, W. R. **Static and dynamic electricity**. 3rd. ed. USA: Hemisphere Publ. Corp., 1989.

[43] SILVESTER, P. P.; OMERAGIC, D. Sensitivity maps for metal detector design. **IEEE Transactions on Geoscience and Remote Sensing**, v. 34, n. 3, p. 788–792, maio 1996.

[44] CATTANI, M.; VANNUCCI, A. Correntes de Foucault: Aspectos básicos. **Revista Brasileira de Ensino de Física**, v. 36, n. 2, jun. 2014.

[45] YAN, S.; CHEN, X. Detection of Non-Ferromagnetic Metal Balls Based on the Analytical Solution of Motion-Induced Eddy-Current Field. **IEEE Transactions on Instrumentation and Measurement**, v. 74, p. 1–10, 2025.

[46] NUNES, J. V. P. Utilização da bobina de Helmholtz para medição do campo magnético da Terra. [s.d.].

[47] GRIFFITHS, D. J. **Introduction to electrodynamics**. 3. ed., reprinted with corrections ed. Upper Saddle River, NJ: Prentice Hall, 1999.

[48] OLABE, X. B. REDES NEURONALES ARTIFICIALES Y SUS APLICACIONES. [s.d.].

[49] MONTESINOS LÓPEZ, O. A.; MONTESINOS LÓPEZ, A.; CROSSA, J. Fundamentals of Artificial Neural Networks and Deep Learning. Em: MONTESINOS LÓPEZ, O. A.; MONTESINOS LÓPEZ, A.; CROSSA, J. (Eds.). **Multivariate Statistical Machine Learning Methods for Genomic Prediction**. Cham: Springer International Publishing, 2022. p. 379–425.

[50] HAYKIN S. Neural Networks: A Comprehensive Foundation, Prentice Hall PTR, Upper Saddle River, New Jersey, USA, 1998.

[51] PAUL MEDINA HUACASI, J. **MODELAGEM DE CORPOS ESTRANHOS MAGNÉTICOS E SOLUÇÃO DO PROBLEMA INVERSO POR REDES NEURAIS**. MESTRE EM METROLOGIA—Rio de Janeiro, Brazil: PONTIFÍCIA UNIVERSIDADE CATÓLICA DO RIO DE JANEIRO, 2 out. 2018.

[52] VOROBIOFF, J.; CERROTTA, S.; MOREL, E. N.; et al. ***Inteligencia Artificial y Redes Neuronales: Fundamentos, ejercicios y aplicaciones con Python y Matlab***. 1. ed. Ciudad Autónoma de Buenos Aires: edUTecNe – Universidad Tecnológica Nacional, 2022. ISBN 978-987-4998-82-8..

APPENDIX A: PAPER SUBMITTED TO THE 2025 BRAZILIAN CONGRESS OF METROLOGY

Development of a measurement system based on a GMI magnetometer and eddy current induction for locating non-ferromagnetic metallic foreign bodies in the human body

B L Martinez Chavez, E Costa Monteiro and C R Hall Barbosa

Postgraduate Programme in Metrology, Pontifical Catholic University of Rio de Janeiro, Rio de Janeiro, Brazil.

brandomartinez@puc-rio.br

Abstract. The detection of non-ferromagnetic metallic foreign bodies within the human body presents a clinical challenge, mainly due to the limitations of conventional imaging techniques such as X-rays and tomography, which expose patients to ionizing radiation and do not always provide precise localisation. This work presents the development of a portable, low-cost system operating at room temperature, based on Giant Magnetoimpedance (GMI) sensors and planar spiral coils. The approach employs eddy currents and differential gradiometric measurements to non-invasively detect non-ferromagnetic metallic bodies, enhancing accuracy and sensitivity compared to existing methods. Experimental results, supported by computational simulations, indicate that the primary magnetic field reaches up to 179 µT at a depth of 6.3 mm, which is consistent with simulated values. Reliable detection of the secondary field enables high-precision localization of the objects. The proposed portable and low-cost system demonstrates feasibility for biomedical applications, contributing to faster, safer, and more effective surgical procedures.

Keywords: Giant Magnetoimpedance (GMI); eddy currents; planar spiral coils; non-ferromagnetic metallic bodies; biomedical application.

1. Introduction

Incidents involving metallic foreign bodies in the human body, often resulting from accidents or firearm projectiles, usually require surgical intervention due to adverse effects [1-,3]. Conventional imaging techniques, such as radiography and tomography, are commonly used but provide low accuracy and involve ionising radiation, which carries health risks [1,2,4-6]. Moreover, they do not provide precise location or depth information, making removal more difficult and prolonging surgeries [1,2,6,7]. These limitations underscore the need for safer, more effective, and noninvasive alternatives [1,2,6].

The magnetometer with the highest sensitivity, the Superconducting Quantum Interference Device (SQUID), presents extremely low noise and has been successfully used in seven clinical cases to locate foreign bodies [1,7,8]. However, its high cost and cryogenic requirements limit its clinical use and violate Biometrology principles [1,2,6].

It is important to acknowledge that, although SQUID systems have been widely studied, quantitative comparisons with other emerging low-cost magnetic detectors, such as GMR sensors and sensors that utilize the Hall effect, are limited. Nevertheless, the development of portable, low-cost alternatives, such as the GMI-based system presented in this work, remains highly relevant, offering clinically feasible solutions without the high cost and operational constraints of superconducting devices. The Biometrology Laboratory (LabBioMet) at PUC-Rio has focused its research on noninvasive clinical diagnostics, developing low-cost, portable systems that operate at room temperature for biomedical applications, including the detection of metallic foreign bodies in humans, based on Giant Magnetoimpedance (GMI) and Giant Magnetoresistance (GMR) sensors [2,3,9-14].

Metallic foreign bodies, however, are not always ferromagnetic, what represents an additional challenge. These objects, such as firearm projectiles, which are frequently encountered in medical practice [15], are typically made of lead (Pb) or elements with diamagnetic properties [3,16]. They lack a remanent magnetic field and therefore cannot be directly measured with magnetic sensors [2,3,13,16]. In this case, locating these objects via magnetic mapping requirer the induction of eddy currents using alternating magnetic fields [2,3,11,13,16,17], which can be detected by a magnetometer with the adequate sensitivity and resolution [2,16]. A preliminary system using a single solenoid for eddy current generation and two high-sensitivity GMI sensors in a gradiometric configuration was developed at LabBioMet for locating non-ferromagnetic metallic foreign bodies' position in humans [2,11]. However, this configuration has shown limitations resulting from the excitation and measurement stages coupling, producing a significant excitation magnetic field in the sensors' region, compromising their linear operation and, consequently, their detection capability [2,11]. As a result, further improvements were necessary to overcome these limitations and fully meet biomedical application requirements [2,6].

Later on, the study conducted by [3,13] proposed and computationally validated [13] an innovative measurement system configuration for locating non-ferromagnetic metallic foreign bodies in the human body. Similar to the approach implemented in [2,11,13], the system in [3] is also based on the generation of eddy currents and the subsequent mapping of the secondary magnetic field. However, this study investigated how the orientation of a single GMI sensor relative to the excitation stage impacts the performance of the magnetic measuring instrument. A setup was designed using a pair of planar spiral coils or long solenoids, which were carefully optimized to enhance sensitivity and precision in detecting and localising non-ferromagnetic metallic objects. The new configuration decouples the excitation and GMI measuring stages, generating a spatial distribution of the field characterized by adequate magnetic flux density levels in the region of the foreign body and nearly imperceptible levels at the sensor site.

The present study experimentally implements the computational proposal described in [3], based on the better results yielded by the double spiral planar coils for the excitation stage. It also considers [2,11] regarding the potential contributions of implementing a gradiometric configuration of the sensing elements for measuring the secondary magnetic flux density by setting up the reading system composed of two sensors. Besides the promise of better performance, the proposed system offers simplicity and low cost, making it well-suited for portable clinical devices. It is designed to safely and non-invasively locating metallic fragments while complying with the exposure limits established by the International Commission on Non-Ionising Radiation Protection (ICNIRP) [18].

2. Materials and Methods

The system developed to locate non-ferromagnetic foreign bodies, such as firearm projectiles, consists of two stages: excitation and measurement. The excitation of the foreign body is carried out by two spiral planar coils wound in opposite directions, creating an almost circular magnetic flux that passes horizontally through the coils and the target

[19]. In the measurement stage, the sensor records the secondary magnetic field generated by these currents.

2.1. GMI Sensor

The commercial GMI magnetometer MI-CB-1DJ-M-B, from Aichi Micro Technology, operating at a frequency of 1 MHz with a sensitivity of 5 V/µT and with a estimated narrow-band resolution of 15 pT, was selected in this work due to its high sensitivity, low cost, and compact dimensions (13.5 × 1.2 mm), making it ideal for portable systems aimed at detecting diamagnetic metallic bodies in biomedical applications [2,6,20].

2.2. Excitation System

The excitation system uses spiral planar coils, as illustrated in Figure 1. These coils were carefully designed to optimize the generation of magnetic fields and have windings in opposite directions, with a distance of 20 mm between them. Each coil has an internal radius of 5 mm and an external radius of 20 mm, with a track width of $w = 0.75$ mm and a spacing between tracks of $s = 0.83$ mm. In addition, each coil contains $N = 10$ turns, considering a maximum amplitude for the excitation current of 1 A.

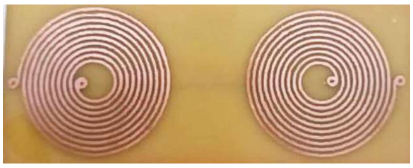

Figure 1. Spiral planar coils of the excitation system.

Both spiral planar coils are powered by sinusoidal currents with a frequency of 8 kHz, maintaining the same intensity and opposite directions. This configuration generates a horizontal magnetic field, providing high intensity in the region of the foreign body, while maintaining a very low intensity of the magnetic field in the area where the GMI sensors are placed.

2.3. Eddy Currents

Eddy currents are current loops induced in conductors when they are exposed to time-varying magnetic fields, and are widely used as a non-destructive testing technique to detect cracks and faults in metals. This effect is also employed in metal detectors, being the operating principle behind devices designed for locating non-ferromagnetic metallic foreign bodies [2,3,13,16]. In this work, the excitation system generates a primary magnetic field that induces eddy currents in the foreign body. These eddy currents generate a secondary magnetic field. The characteristics of this secondary field depend on the properties of the foreign body, such as its size, shape, and relative position to the primary magnetic field [3,11,13]. The calculation of the secondary magnetic field was based on the classical formulation for eddy currents in metallic spheres subjected to time-varying magnetic fields as is thoroughly described in [3].

2.4. Detection System

In this system, two GMI sensors are used, with each sensor centered in one of the coils and measuring the magnetic field component parallel to the coil plane. This arrangement allows each sensor to be mostly insensitive to the primary magnetic field and simultaneously be sensitive to the secondary magnetic field, thus allowing a large increase in the primary magnetic field and improving the accuracy and sensitivity of the measurements. Figure 2a illustrates the experimental setup, showing the spiral coils and the positioning of the GMI sensors relative to them.

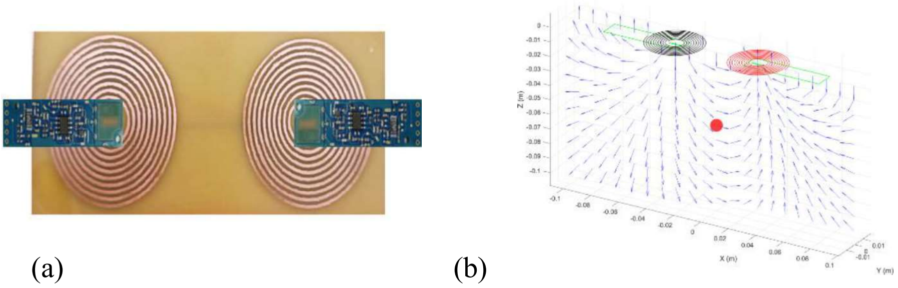

(a) (b)

Figure 2. Positioning of the GMI sensors relative to the coils. (a) Experimental setup showing the GMI sensors arranged parallel to the coils. (b) a three-dimensional mesh to compute the resulting field around the sphere and its variation across the sensors.

2.5. Signal Conditioning and Processing Circuit for Gradiometric Measurement

Based on the architecture proposed by [2,11], which explored similar systems for detecting non-ferromagnetic metallic foreign bodies using eddy currents and GMI magnetometers, the GMI-based detection system comprises essential primary elements, such as band-pass filters and instrumentation amplifiers, which are fundamental for gradiometric reading and signal amplification.

Figure 3 outlines the main functional blocks of the system. The excitation of the planar coils controls the frequency (f₀) and amplitude (I₀) of the coil current, being responsible for generating the primary magnetic field. The outputs of each GMI sensor are connected to fourth-order band-pass filters centered at 8 kHz. The filtered signals are then fed to an instrumentation amplifier, which is used to perform the gradiometric reading while introducing gain.

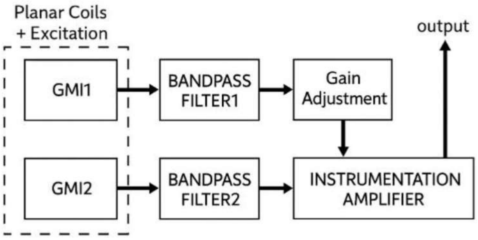

Figure 3. Block diagram of the implemented circuit for gradiometric magnetic reading.

3. Results and discussion

3.1. Primary Magnetic Field

The simulation of the primary magnetic field aimed to characterise the spatial distribution generated by the spiral coils used in the experiment. A computational model based on the Biot–Savart Law was implemented in MATLAB, considering the actual geometry of the system. The results revealed an alternating pattern along the X-axis, with two symmetrical positive peaks and a more pronounced negative peak in the central region (Figure 4), resulting from the superposition of the fields generated by two coils powered with an 8 kHz alternating current of 1 A. The magnetic flux density reaches values greater than 179 µT (in magnitude) at a depth of 6.3 mm, indicating a strong concentration of the field in the region of interest for foreign body detection. The experimental results confirmed the behaviour predicted by the simulation, showing an alternation of magnetic flux density along the X-axis, reproducing the same simulated pattern and a maximum error of approximately 6 µT (3.35 %), well below the commonly accepted 5 % threshold, confirming both the robustness of the theoretical model and the reliability of the experimental procedures. These results provide a solid foundation for the subsequent analysis of the secondary magnetic field.

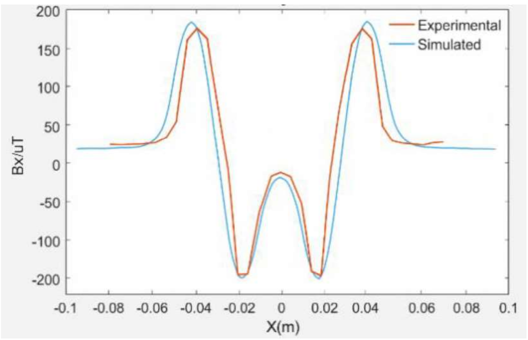

Figure 4 – Comparison between simulated and experimental results of the primary magnetic flux density generated by the spiral planar coils distributed along the X-axis.

3.2. Simulation of the Secondary Magnetic Field

The secondary magnetic field generated by a non-ferromagnetic metallic body was simulated in MATLAB using the same geometric model of coils and sensors previously described (Figure 2b). A three-dimensional mesh was used to compute the resulting field around the sphere and its variation over the sensors. Figure 5 shows the simulated spatial distribution of the secondary magnetic field B_x, resulting from the interaction between the primary field and the lead sphere.

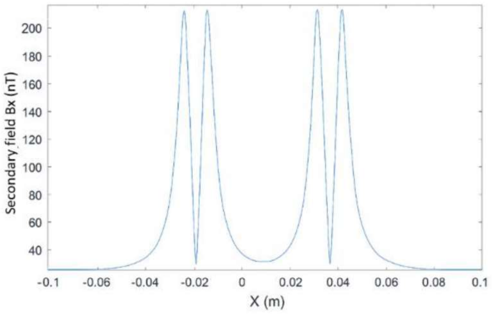

Figure 5 –Simulated response of the secondary magnetic field B_x along the X-axis for a lead sphere positioned at the centre of the measurement system.

Four prominent peaks are observed in the regions where the sphere aligns with the edges of the coils, indicating maximum secondary field intensity. Between these peaks, the field decreases significantly and approaches zero, the behaviour expected when the sphere is located at the centre, where magnetic contributions cancel out. These results provide a theoretical prediction of the system's response under ideal conditions, to be later compared with experimental data.

3.3. Experimental Results of the Secondary Magnetic Field

Measurements were conducted using lead (Pb) spheres with diameters ranging from 3 to 11 mm, at distances of 6 mm and 9 mm. The gains used in the experiments were set to 1, 10, and 20 V/V. In the following section, the results are presented according to the gain applied to the readout circuit, showing the four characteristic peaks of the secondary magnetic field as a function of sphere diameter for each fixed distance, which corresponds to the distance between the lead sphere and the detecting sensors.

3.3.1. Results with gain of 1 V/V. Table 1 presents the peak values of the measured secondary magnetic field for different diameters of lead spheres with a constant distance of 6 mm and a gain of 1 V/V. A characteristic pattern of four peaks is observed, which is associated with the position of the sphere relative to the sensitive region of the GMI sensors.

Table 1. Peak amplitudes of the secondary magnetic field for a gain of 1 and 6 mm distance, considering a set of lead spheres with diameters from 4 mm to 11 mm.

Diameter (mm)	Distance (mm)	Gain (V/V)	Peak1 (nT)	Peak2 (nT)	Peak3 (nT)	Peak4 (nT)
11.0	6.0	1	368.46	368.57	301.79	302.87
10.0	6.0	1	340.85	341.50	277.30	277.53
9.0	6.0	1	279.79	278.15	226.44	226.67
8.0	6.0	1	183.74	186.87	150.73	153.27
7.0	6.0	1	129.17	128.69	109.09	108.50
6.0	6.0	1	72.55	73.37	53.57	53.71
5.0	6.0	1	35.61	35.58	28.23	27.78
4.0	6.0	1	8.97	8.88	6.36	6.31

Figure 6 presents the eight signals depicted in Table 1, showing that peak intensity increases proportionally with sphere diameter due to stronger interaction with the excitation field.

Table 2 presents the data obtained for the same set of spheres, but with a distance of 9 mm, also under a gain of 1 V/V. The peak values decrease significantly compared to the 6 mm distance, highlighting the dependence of amplitude on the distance between the sphere and the sensors.

Figure 7 shows the behaviour of the secondary magnetic field with a gain of 1 and a distance of 9 mm. Compared to Figure 6, a general decrease in the peak amplitudes can be observed, as expected, due to the increased distance between the object and the sensors.

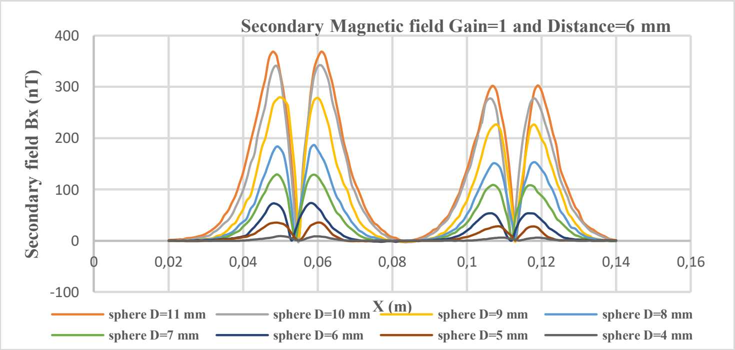

Figure 6 - B_x for spheres with diameters from 4 mm to 11 mm, with a gain of 1 V/V and 6 mm distance.

Table 2 – Peak amplitudes of the secondary magnetic field for a gain of 1 V/V and 9 mm distance, considering same set of lead spheres, but with diameters from 5 mm to 11 mm.

Diameter (mm)	Distance (mm)	Gain (V/V	Peak 1 (nT)	Peak 2 (nT)	Peak 3 (nT)	Peak 4 (nT)
11.0	9.0	1	89.44	90.23	81.18	80.72
10.0	9.0	1	71.53	72.27	58.18	58.29
9.0	9.0	1	64.21	64.83	50.54	49.89
8.0	9.0	1	55.24	55.92	42.23	41.92
7.0	9.0	1	29.64	29.87	21.38	21.41
6.0	9.0	1	19.40	19.18	15.30	15.13
5.0	9.0	1	8.68	8.71	6.28	6.17

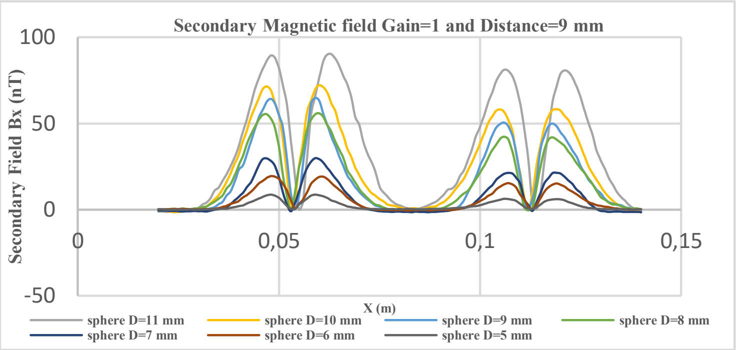

Figure 7-B_x curves for spheres with diameters from 5 mm to 11 mm, with a gain of 1 and 9 mm distance.

3.3.2. Results with gain of 10 V/V. Tables 3 and 4 present the measured peaks for a gain of 10 V/V, with distances of 6 mm and 9 mm, respectively. The increased gain enables the detection of weaker signals from lower-diameter spheres, specifically 3 mm for the 6 mm distance and 4 mm for the 9 mm distance, while preserving the symmetric pattern of the detected peaks.

Table 3 – Peak amplitudes of the secondary magnetic field for a gain of 10 V/V and 6 mm distance, with sphere diameters ranging from 3 mm to 6 mm.

Diameter (mm)	Distance (mm)	Gain (V/V)	Peak 1 (nT)	Peak 2 (nT)	Peak 3 (nT)	Peak 4 (nT)
6.0	6.0	10	81.82	81.86	72.39	72.20
5.0	6.0	10	37.59	37.69	29.42	29.32
4.0	6.0	10	14.28	14.18	12.41	12.32
3.0	6.0	10	5.45	5.45	3.30	3.20

Figure 8 illustrates the results obtained with a gain of 10 V/V for distances of 6 mm and 9 mm, respectively, in Figures 8a and 8b. The increasing trend with the sphere diameter remains evident, although with less pronounced variations at greater distances (Figure 8b).

Table 4 – Peak amplitudes of the secondary magnetic field for a gain of 10 V/V and 9 mm distance, with sphere diameters ranging from 4 mm to 11 mm.

Diameter (mm)	Distance (mm)	Gain (V/V)	Peak 1 (nT)	Peak 2 (nT)	Peak 3 (nT)	Peak4 (nT)
11.0	9.0	10	102.67	103.04	90.24	90.10
10.0	9.0	10	83.91	83.91	67.98	68.76
9.0	9.0	10	69.82	70.11	57.43	57.18
8.0	9.0	10	61.03	60.94	47.27	47.30
7.0	9.0	10	38.70	38.67	30.65	30.51
6.0	9.0	10	24.42	24.38	21.05	21.12
5.0	9.0	10	9.22	9.18	7.68	7.58
4.0	9.0	10	3.72	3.76	2.96	2.98

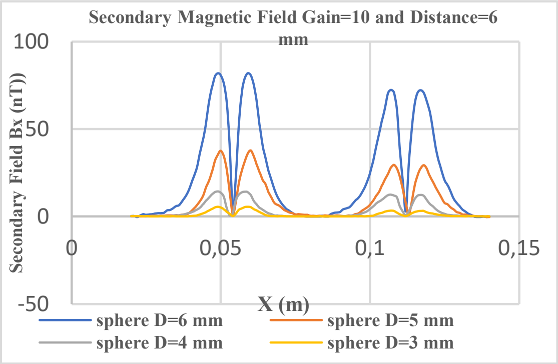

(a)

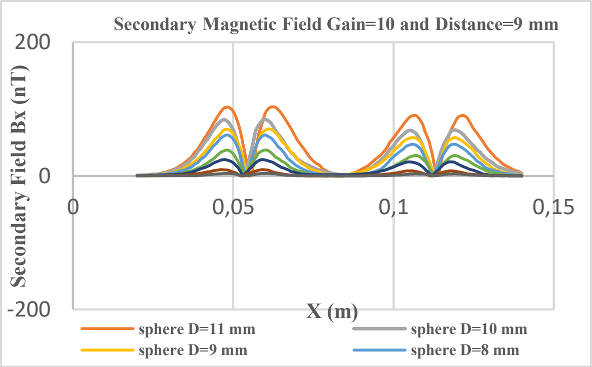

(b)

Figure 8- B_x curves for spheres with a gain of 10, in **(**a) for spheres with diameters from 3 mm to 6 mm and a distance of 6 mm; in (b) for spheres with diameters from 5 mm to 11 mm and a distance of 9 mm.

3.3.3. Results with gain of 20 V/V. Table 5 presents the data obtained with a gain of 20 V/V and a distance of 6 mm, used especially for spheres with smaller diameters, ranging from 3 mm to 6 mm. The distance amplification allowed for clear detection of signals even for 3 mm spheres.

Table 5 – Peak amplitudes of the secondary magnetic field for a gain of 20 and a 6 mm distance.

Diameter (mm)	Distance (mm)	Gain (V/V)	Peak 1 (nT)	Peak 2 (nT)	Peak 3 (nT)	Peak 4 (nT)
6.0	6.0	20	83.61	83.70	76.79	76.82
5.0	6.0	20	38.12	38.16	33.33	33.33
4.0	6.0	20	17.53	17.56	15.27	15.18
3.0	6.0	20	5.88	5.88	4.27	4.25

Figure 9 shows the experimental data for a gain of 20 and a distance of 6 mm, mainly applied to small spheres, from 3 mm to 6 mm in diameter. Despite the low absolute intensity of the peaks, the amplification makes it possible to observe the typical shape of four symmetric peaks clearly.

Finally, Table 6 summarises the smallest detectable sphere diameter for each distance and gain analysed. At 6 mm distance, spheres as small as 3 mm were detected with gains of 10 and 20 V/V, and 4 mm with a gain of 1 V/V. At 9 mm distance, the limit was the diameter of 5 mm with a gain of 1 V/V and 4 mm diameter with a gain of 10 V/V. These results confirm the significant influence of gain on system sensitivity and serve as a reference for the simulation comparison in the next section. According to these results. a gain of 10 V/V is the most efficient one for both studied distances.

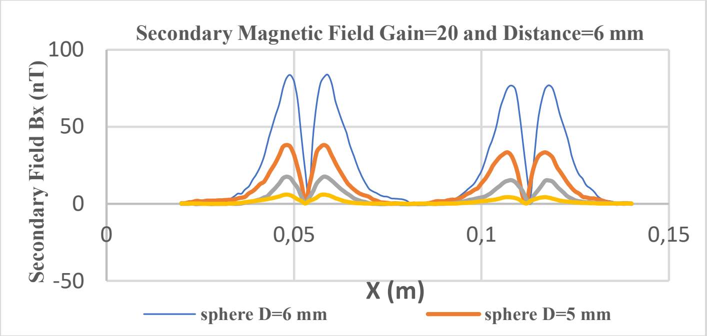

Figure 9- B_x curves for spheres with diameters from 3 mm to 6 mm, with a gain of 20 and 6 mm distance.

Table 6 – Smallest detectable diameter of metallic spheres according to sensor distance and amplification gain.

Distance (mm)	Diameter (mm) for Gain = 1 V/V	Diameter (mm) for Gain = 10 V/V	Diameter (mm) for Gain = 20 V/V
6.0	4.0	3.0	3.0
9.0	5.0	4.0	-

4. Discussion

4.1. *Primary Magnetic Field*

The comparison between experimental and simulated results of the primary magnetic field showed excellent agreement (Figure 4), with a maximum amplitude error of only 3.35 %.

In contrast to systems using long solenoids [2], limited to ~1 μT, our planar coil design generated stronger fields without saturating the GMI sensor, enhancing excitation without compromising linearity. This validates both the computational model and the experimental methodology.

4.2. *Secondary Magnetic Field*

Simulated and experimental secondary field curves showed similar shapes, featuring the expected four-peak pattern (Figures 5 to 9). Amplitude differences were observed: simulated values were higher for larger spheres, closely matched for intermediate sizes, and lower than experimental results for smaller spheres. This trend was consistent across gain levels (1, 10, and 20) and measurement distances (6 mm and 9 mm), indicating the model's robustness but also the influence of sphere size.

Compared to SQUID-based systems [1], our GMI-based solution offers a cost-effective, room-temperature alternative, with slightly lower sensitivity but improved clinical feasibility [2,5,6]. Prior GMI systems [2,3,11] suffered from low excitation due to sensor constraints, limiting detection of weak secondary fields. In our design, the physical separation between excitation and measurement stages improved sensitivity without exceeding sensor limits [3,13].

5. Conclusions and Future Work

In this work, a system for detecting non-ferromagnetic metallic bodies based on eddy currents induced by an excitation system using spiral planar coils and a gradiometric readout using GMI sensors was developed. The objective was to overcome limitations of previous approaches, such as GMI sensor saturation caused by the primary field configuration relative to the position of these sensing elements and the low portability and high cost of SQUID-based systems.

The developed system combines two previously studied concepts: planar spiral coils with opposite windings for generating the primary field [3,13], and differential readout with GMI sensors [11]. This configuration enabled higher excitation without saturation and improved detection sensitivity, as demonstrated experimentally. Experimental results showed that tiny metallic spheres were detected at depths of 6 mm and 9 mm, within the exposure limits established by ICNIRP for the primary field generated. The modelling of the primary field showed strong agreement with the experimental data, thereby validating the theoretical model. An amplification of 10 V/V is an optimized choice for any distance between the sensor and the foreign body employed in investigation.

For the secondary field, the four peaks predicted by the simulation were observed experimentally. The amplitude discrepancies, particularly for large or small spheres, can be attributed to the effective conductivity of the material and the limitations of the simplified model.

Therefore, the results obtained indicate that the developed system is a viable, safe, low-cost, and non-invasive solution for localizing non-ferromagnetic metallic bodies, with potential for real clinical applications. The use of accessible technologies, operation at room temperature, and the possibility of integration with intelligent algorithms make this system a promising alternative to conventional methods based on ionising radiation.

Several directions for future research are proposed to enhance the system and broaden its applicability. Although the current computational model, based on analytical approximations, showed good agreement with experimental results, using finite element methods would allow for a more accurate representation of the system's geometry and the resulting magnetic fields. Additionally, since the secondary magnetic field depends heavily on the sphere's electrical conductivity, future work should include specific experiments to characterise this property in the investigated projectiles accurately.

Finally, it is important to acknowledge certain limitations of the present study. The detection depth demonstrated (6–9 mm) is clinically limited, as many projectiles may be located deeper in tissue. Therefore, the proposed system is particularly suitable for scenarios involving superficial metallic fragments, such as subcutaneous regions, where conventional methods are less effective or carry higher risks. Moreover, the secondary magnetic field model adopted in this work was based on spherical metallic objects and analytical approximations, which simplify the geometry and allow for controlled validation but do not fully represent the irregular shapes and fragmentation commonly found in real projectiles. These aspects constrain the direct extrapolation of results to more complex clinical scenarios. Nevertheless, the adopted approach was appropriate for demonstrating the proof of concept and ensuring measurement reliability. Future studies will address these limitations through experiments with irregular projectiles and numerical modeling based on finite element methods to extend the applicability of the system.

Acknowledgments

The authors thank, for the financial support provided, the Brazilian funding agencies CNPq, CAPES, FINEP, and FAPERJ. This study was financed in part by the Coordenação de Aperfeiçoamento de Pessoal de Nível Superior-Brasil (CAPES)-Finance Code 001.

References

[1] Costa Monteiro E, Barbosa C, Lima E, Costa Ribeiro P, Boechat P Locating steel needles in the human body using a SQUID magnetometer. Phys Med Bio (2000) 45(8): 2389–402. doi:10.1088/0031-9155/45/8/323

[2] Fortaleza LGS, Costa Monteiro E, Barbosa CRH, Silva EC, Gusmão LAP Biomedical comparison of magneto-meters for non-ferromagnetic metallic foreign body detection. JPhys Conf. Ser (2018) 1044:012013. doi:10.1088/1742-6596/1044/1/012013

[3] Seixas V, Barbosa C R H, Costa Monteiro E, "Design of a system for detection of non-ferromagnetic metallic foreign bodies based in eddy currents and GMI magnetometer," *Frontiers in Physics*, vol. 12, p. 1330887, 2024. DOI: 10.3389/fphy.2024.1330887.

[4] Maralakunte M, Debi U, Singh L, Pruthi H, Bhatia V, Devi G, et al. Foreign body imaging-experience with 6 cases of retained foreign bodies in the emergency radiology unit. Arch Clin Med Case Rep (2020) 4(5):952–68. doi:10.26502/acmcr.96550285

[5] Costa Monteiro E, Leon L. Metrological reliability of medical devices. J Phys Conf Ser (2015) 588:012032. doi:10.1088/1742-6596/588/1/012032

[6] Costa Monteiro E, Summers R Metrological requirements for biomedical device assessment and their ethical implications. Meas Sensors (2022) 24:100574. doi:10.1016/j.measen.2022.100574

[7] Barbosa C R H, Costa Monteiro E, Lima E A, Santos S, Cavalcanti E, Costa Ribeiro P Improvement of a technique for localization of steel needles in humans using a SQUID magnetometer. IEEE Trans App Sup (2001) 11(1):677–80. doi:10.1109/77.919435

[8] Andrä W, Nowak H, Magnetism H In medicine: a handbook. 2. Weinheim: WILEY-VCH Verlag GmbH and Co. KGaA (2007).

[9] Pompéia F, Gusmão LAP, Barbosa CRH, Costa Monteiro E, Gonçalves L, Machado F Ring shaped magnetic field transducer based on the GMI effect. Meas Sci Technol (2008) 19:025801. doi:10.1088/0957-0233/19/2/025801

[10] Silva E C, Gusmão L A P, Barbosa C R H, Costa Monteiro E, Machado F High sensitivity giant magneto-impedance (GMI) magnetic transducer: magnitude versus phase sensing. Meas Sci Technol (2011) 29:035106. doi:10.1088/1361 6501/aaa27f

[11] Fortaleza L G S, Barbosa C R H, Costa Monteiro E, Silva E C, Gusmão L Detecting non magnetic metallic foreign bodies by GMR sensors through the use of eddy currents. XI Int Congress Electr Metrology (Semetro) (2015) 1–4.

[12] Benavides LS, Silva EC, Costa Monteiro E Pressure transducer based on the phase characteristics of GMI effect for measuring the arterial pulse wave. J Phys Conf. Ser (2018) 1065:072039. doi:10.1088/1742-6596/1065/7/072039

[13] Seixas V, Hall Barbosa C R, Costa Monteiro E. New measuring system for locating firearm projectiles in the human body based on eddy currents and GMI sensors. Journal of Physics: Conference Series 2606 (2023) 012002 IOP Publishing doi:10.1088/1742-6596/2606/1/012002

[14] Benavides Cabrera, L. S.; Costa da Silva, E.; Costa Monteiro, E. Highly Sensitive Pressure Transducer for Measuring Arterial Pulse Wave Velocity Based on Giant MagnetoImpedance Sensors. Sensors 2025, 25, 3188. https://doi.org/10.3390/ s25103188

[15] Dienstknecht T, Horst K, Sellei R M, Berner A, Nerlich M, Hardcastle T C "Indications for bullet removal: overview of the literature, and clinical practice guidelines for European trauma surgeons". Eur J Trauma Emerg Surg (2012) 38(38): 89–93. doi:10.1007/s00068-011-0170-x

[16] Barbosa C R H. Localization of firearm projectiles in the human body using a superconducting quantum interference device magnetometer: a theoretical study. Rev Scientific Instr (2004) 75(6):2098–106. doi:10.1063/1.1753679

[17] Ripka P, Mirzaei M,Blažek JMagnetic position sensors.Meas Sci TechnolV(2022) 33:022002. doi:10.1088/1361-6501/ac32eb

[18] International Commission on Non-Ionizing Radiation Protection. Guidelines for limiting exposure to time-varying electric and magnetic fields (1 Hz to 100 kHz). Health Phys (2010) 99(6):818–36. doi:10.1097/HP.0b013e3181f06c86

[19] Palatnik de Sousa I, Barbosa CRH, Costa Monteiro E. Safe exposure distances for transcranial magnetic stimulation based on computer simulations. PeerJ (2018) 6:e5034. doi:10.7717/peerj.5034

[20] Oliveira B R C, Louzada DR, Costa Monteiro E, Barbosa C.R.H., "Automatic system for locating magnetic foreign bodies using GMI magnetometer," *Journal of Physics: Conference Series*, vol. 1826, p. 012085, 2021.

[21] Machado F L A, Rezende S M, "A theoretical model for the giant magnetoimpedance in ribbons of amorphous soft-ferromagnetic alloys," *Journal of Applied Physics*, vol. 79, no. 8, p. 6558, 1996. DOI: 10.1063/1.361945.

[22] Machado F L A, Silva Blda, Rezende S M, Martins CS. Giant ac magnetoresistance in the soft ferromagnet Co70.4Fe 4.6Si15B10. J Appl Phys (2018) 75(10):6563–5. doi:10.1063/1.356919